

The Heusler alloy Co_2MnSi in thin films

Dissertation zur Erlangung des Doktorgrades
der Fakultät für Physik der
Universität Bielefeld

vorgelegt von

Sven Kämmerer

29. Oktober 2004

Erklärung

Hiermit erkläre ich Eides statt, daß ich die vorliegende Arbeit selbstständig verfaßt und keine anderen als die angegebenen Hilfsmittel verwendet habe.

Bielefeld, 29. Oktober 2004

(Sven Kämmerer)

Gutachter:

Priv. Doz. Dr. Andreas Hütten
Prof. Dr. Markus Sauer

Datum des Einreichens der Arbeit: 29. Oktober 2004

Gedruckt auf alterungsbeständigem Papier °° ISO 9706

Contents

| | |
|---|-----------|
| Preface | 1 |
| 1 Fundamentals | 5 |
| 1.1 Heusler alloys | 5 |
| 1.1.1 Unit cell | 5 |
| 1.1.2 Ferromagnetism | 6 |
| 1.1.3 Half metallicity | 10 |
| 1.2 Ordering on atomic scale | 12 |
| 1.2.1 Ordering parameters | 12 |
| 1.2.2 Determination of the disorder parameter | 14 |
| 1.2.3 Evolution of structure factor with ordering | 18 |
| 2 Preparation I - Co₂MnSi thin films | 21 |
| 2.1 The sputtering system | 21 |
| 2.2 Annealing process | 23 |
| 2.3 The choice of substrate | 24 |
| 3 Characterization | 27 |
| 3.1 Magnetic measurements | 27 |
| 3.1.1 Magneto-optical Kerr effect (MOKE) | 27 |
| 3.1.2 Alternating Gradient Magnetometer (AGM) | 28 |
| 3.2 Transport measurements | 29 |
| 3.2.1 Measurements at room temperature | 29 |
| 3.2.2 Temperature dependence | 30 |
| 3.3 Atomic arrangement on nanoscale | 30 |
| 3.3.1 X-ray diffraction | 30 |
| 3.3.2 Auger spectroscopy | 32 |
| 3.3.3 XAS/XMCD | 33 |
| 3.4 Determination of spin polarization | 33 |
| 3.4.1 Magnetic tunnel junctions | 34 |
| 3.4.2 Alternative techniques | 35 |

| | | |
|----------|---|------------|
| 4 | Thin films of Co₂MnSi | 39 |
| 4.1 | Polycrystalline films | 39 |
| 4.1.1 | Electrical behavior | 39 |
| 4.1.2 | Magnetic evolution | 41 |
| 4.1.3 | Analysis of microstructure | 43 |
| 4.2 | Textured films | 45 |
| 4.2.1 | Electrical behavior | 45 |
| 4.2.2 | Magnetic evolution | 46 |
| 4.2.3 | Analysis of microstructure | 47 |
| 4.3 | Conclusion - ordering and intrinsic parameters | 48 |
| 4.4 | Growth of Co ₂ MnSi films | 50 |
| 4.4.1 | Surface morphology and roughness | 52 |
| 4.4.2 | Magnetism | 53 |
| 4.4.3 | Local ordering | 53 |
| 5 | Preparation II - magnetic tunnel junctions (MTJs) | 57 |
| 5.1 | Magnetic tailoring | 57 |
| 5.2 | The barrier | 60 |
| 5.3 | The stack - patterning | 60 |
| 5.4 | The final process layout | 61 |
| 6 | Spin polarization in thin Co₂MnSi films | 63 |
| 6.1 | TMR effect amplitude and spin polarization realized | 63 |
| 6.1.1 | Quality of the interface I - electrical behavior | 64 |
| 6.1.2 | Quality of the interface II - atomic distribution | 73 |
| 6.1.3 | Co-termination at the interface | 77 |
| 6.2 | Spin polarization and local ordering | 80 |
| 7 | IETS - Inelastic electron tunneling spectroscopy | 85 |
| 7.1 | Experimental aspects | 85 |
| 7.2 | Results | 86 |
| | Conclusion and outlook | 89 |
| | A X-ray diffraction patterns | 93 |
| | Publications and talks | 95 |
| | Bibliography | 104 |
| | Acknowledgment | 105 |

Preface

A first glance at the title of this thesis "The Heusler alloy Co_2MnSi in thin films" may arise a minimum of three questions. The first term is *Heusler* alloy. What are Heusler alloys and what makes them interesting for research and applications. Secondly, the special choice of Co_2MnSi has to be discussed and finally, the restriction to thin films should be illuminated.

Before introducing physical aspects of this thesis, the historical background of the term Heusler alloy has to be clarified. It was named after Friedrich Heusler (1866-1947), who discovered Cu_2MnAl to be ferromagnetic in 1903 [1], although the alloy only consists of non-magnetic elements. Today the name Heusler alloys is attributed to two classes of materials: The half Heusler alloys with general formula XYZ and the full Heusler alloys with X_2YZ . The X and Y are elements of the transition metal group, whereas the Z component comes from the group III-V elements. Both classes exhibit well defined microstructures. The full Heusler alloys are characterized by the L2_1 structure and the half ones by the C1_b . These two types of unit cells are described well by the picture of four interpenetrating fcc lattices, each occupied by one of the four constituents in the case of full Heusler alloys and three occupied and one free sublattice for the half ones. How the ferromagnetism in many Heusler alloys appears is still not fully understood, but it is attributed to the complex unit cell of this type of materials.

Some of the Heusler alloys show *half metallic* character as was pointed out in 1983 by de Groot *et al.* [2]. This makes them very interesting candidates for spin electronic applications, even a long time after their discovery in 1903. In spin electronic or spintronic devices additional to the carrier charge the spin of the electrons is used to store information. The fundamental physical effects in spintronics are the Giant Magnetoresistance (GMR) and the Tunnel Magnetoresistance (TMR). These two related phenomena bear two different physical effects. However, both are only apparent in thin film systems ($\sim\text{nm}$). The GMR effect is based on the spin dependent scattering on magnetic/non-magnetic interfaces, where the TMR effect is founded on the quantum mechanical tunneling effect with spin-split transition probabilities. However, in magnetoresistance behavior these two effects show similar characteristics, which can best be illustrated by the simplest system of two ferromagnetic layers separated by a conducting (GMR) or insulating (TMR) spacer layer. If it is possible to reach the antiparallel and parallel states of the in-plane magnetization of the two ferromagnets by variation of an external magnetic field, these

two states differ in its electrical resistance. The magnetoresistance effect amplitude is then defined by resistive difference $\Delta R = R_{AP} - R_P$ of the two states normalized to the resistance of the parallel R_p (low resistance) state:

$$TMR = \frac{\Delta R}{R_P} \quad (1)$$

These two states, defined by their different resistivities, can serve as logical 1 and 0 within the magnetic random access memory (MRAM) concept. Alternatively, if not the sole two states are taken into account, but the detailed change of resistance in an external field is considered, the concept of a magnetic field sensor or hard drive read head is applicable. Within this concept not a high effect amplitude is important in the first way, but a most rapid change is desired. This sensitivity can be increased by nearly rectangular switching of the magnetic layers and by high effect amplitudes. In this background this thesis is dedicated to improve the effect amplitude by a suited choice of the magnetic materials. How this choice has to be taken will become clear by the fact that a high effect amplitude is based on high spin polarization of the electrons at the Fermi level in the ferromagnets. This correlation was revealed by Julliere in 1975. This makes the search for highly spin polarized materials obvious. If the spin polarization of the conduction electrons is 100 %, one speaks of half metallic character. Additional to this half metallic character Heusler alloys also provide fundamental aspects concerning ferromagnetism in complex systems due to their complex microstructure and the consequently complex behavior of the ferromagnetism. Accordingly, Heusler alloys are of great interest in fundamental investigations concerning the understanding of ferromagnetism.

Firstly, theoretical investigations by Ishida *et al.* in 1998 [3] dragged attention to Co_2MnSi . Band structure calculations revealed a half metallic character for Co_2MnSi , in addition to its relatively large Curie temperature of 985K [4]. These two aspects make Co_2MnSi a very promising candidate for applications in spintronics. Especially the high Curie temperature opens the way from fundamental research to applications due to the fact that the temperature dependence of the spin polarization scales with the Curie temperature. A low Curie temperature would rest only a poor fraction of the full spin polarization at room temperature. However, a room temperature working is a must for electronic applications. Experimentally, Co_2MnSi was completely characterized by Webster [4] with respect to its magnetic and microstructural behavior, but only in bulk specimens. For technical purposes spintronic devices made of thin films (\sim nm) are required. These thin film aspects were independently discussed by Geiersbach *et al.* [5, 6] and Raphael *et al.* [7]. They fabricated thin Co_2MnSi films for the first time and thus laid the foundation of the present work. Experimental parameters of their results were taken as an input for the initial experimental investigations.

Although theoretical and experimental investigations of Co_2MnSi were performed, no thin film spin polarization measurements were done before this work was started. This is one major task of the present thesis. One way to determine the spin polarization of

thin films is to establish the TMR effect and apply Julliere's formula, which connects the TMR effect amplitude to the spin polarizations P_1 and P_2 of the two ferromagnets [8]:

$$TMR = \frac{2P_1P_2}{1 - P_1P_2} \quad (2)$$

Such a determination is performed in a so-called magnetic tunnel junction (MTJ) emphasizing the layered structure of the system.

Alternatively, ways to determine the spin polarization in thin films as photo emission and vacuum tunneling are not suited due to the fact that they do not respect the complex layered structure of a MTJ. Especially the important interfaces to the insulator are different in such measurements. Only the determination by MTJs can consider the complex aspects of a following application in spintronic devices.

Although a MTJ consists of three simple layers, its ideal realization takes great efforts. The preparation of the insulating barrier, AlO_x in the present case, as well as the separated magnetic switching of the ferromagnets to achieve quite distinguished parallel and antiparallel states are known to be important aspects. However, if this can experimentally be realized, the formation of a Heusler alloys film is a challenging task. Especially local disorder processes are known to emphasize the half metallic character sensitively. Theoretical investigations by Ishida [3] show that local disorder effects would destroy the half metallic character. In real samples, the occurrence of disorder was shown in bulk (Webster [4] and Brown *et al.* [9]) and thin films (Raphael *et al.* [7]). For highly spin polarized thin films one has to avoid such a disorder process. Therefore, the different types of disorder have to be identified and understood.

To address all these aspects, the present work is divided as follows. Firstly, a brief review of the fundamentals of ferromagnetism with focus on the case of the Heusler alloys will be given. Then, it will become clear that disorder will sensitively disturb ferromagnetic exchange interaction. By this the need for a quantitative description of disorder processes becomes apparent and an adequate formalism will be presented in the second part of chapter 1. The following chapter 2 deals with initial experiments concerning the growth of Co_2MnSi films. The choice of substrate as well as the deposition parameters are of importance, where the experiments by Geiersbach *et al.* [5, 6] and Raphael *et al.* [7] serve as initial points. Afterwards in chapter 3 the experimental methods and their special features with respect to this work will be described. The magnetic, electrical and microstructural properties of single Co_2MnSi films are discussed in chapter 4. Here, a lot of known as well as new aspects are investigated with respect to Co_2MnSi . This knowledge of preparation conditions and physical properties of Co_2MnSi in thin films enables one to develop a strategy for integrating thin Co_2MnSi films in MTJs. This leads to the possibility to determine the spin polarization. Occurring problems of the integration process and their solutions are given in chapter 5, where the complete process resulting in a working MTJ is presented. The discussion of spin polarization determination including a detailed analysis of the $\text{Co}_2\text{MnSi}/\text{AlO}_x$ interface and the restricting factors for applications are presented in the following chapter 6. Finally, to get more insight into the

exact tunneling process, inelastic electron tunneling spectroscopy (IETS) is established in a qualitative manner.

Chapter 1

Fundamentals

Heusler alloys exhibit the promising possibility enhancing current magnetoresistive devices. Its theoretically predicted 100 % spin polarization is very interesting in terms of applications, but also from fundamental physical point of view. Consequently, the beginning of this thesis is dedicated to reveal the fundamentals of Heusler alloys. Its characteristic microstructure plays a dominant role for the magnetic properties and the underlying spin polarization at the Fermi level.

1.1 Heusler alloys

The history of the Heusler alloys began in 1903. Friedrich Heusler discovered Cu_2MnAl to be ferromagnetic, although its elements are all non-ferromagnetic [1]. When the microstructure was completely understood in 1929, the search for other Heusler alloys with similar unit cells was initiated. The theoretical prediction of 100 % spin polarization of some of the Heusler alloys in 1983 [2] and especially that for Co_2MnSi in 1998 [3] makes them interesting for spinelectronic applications as an alternative for conventional 3d ferromagnets such as Fe, Co or Ni and their alloys, exhibiting only 51 % spin polarization at low temperatures [10].

1.1.1 Unit cell

Co_2MnSi crystallizes in the $L2_1$ structure, as is the case for all full Heusler alloys. This unit cell can be visualized in a picture of four interpenetrating fcc lattices, each occupied by one of the participating elements as indicated in Fig. 1.1. The two Co sublattices are positioned at $(0,0,0)$ and $(\frac{1}{2},\frac{1}{2},\frac{1}{2})$, where the Mn sublattice is at $(\frac{1}{4},\frac{1}{4},\frac{1}{4})$ and the Si sublattice at $(\frac{3}{4},\frac{3}{4},\frac{3}{4})$ in the unit cell.

Thus, silicon and manganese atoms are surrounded by eight cobalt atoms. Each cobalt atom has four silicon and four manganese atoms as next neighbors. The visualized crystal

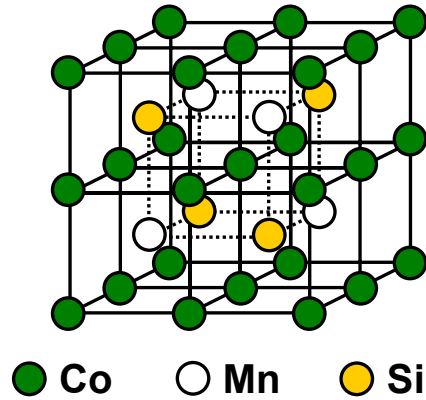


Figure 1.1: Assembly of atoms in Co_2MnSi unit cell displaying the $L2_1$ structure: four interpenetrating fcc lattices, each occupied by one of the elements (Co, Co, Mn, and Si)

structure in Fig. 1.1 displays four times the volume corresponding to the formula unit (f.u.) Co_2MnSi . The lattice constant available from x-ray diffraction characterization is determined to be $a=0.5670\text{ nm}$ [11]. In contrast, half Heusler alloys exhibit only three interpenetrating fcc lattices. One of the two cobalt sublattices is empty. These empty sites make the half Heusler alloys more fragile to swaps with this fcc sublattice [12, 13] to form a state of higher degree of disorder. However, the consequences of this disorder on the spin polarization at the Fermi level are not that drastic, since the half Heusler alloys exhibit a larger gap with respect to the full ones [14].

1.1.2 Ferromagnetism

The appearance of ferromagnetism in the original Heusler alloy is not that obvious as it is for Co_2MnSi . In Cu_2MnAl the ferromagnetism is carried by manganese atoms, although manganese as pure element exhibits an antiferromagnetic behavior at low temperature and a paramagnetic one at room temperature [15]. This ferromagnetic coupling between manganese atoms is still present in Co_2MnSi . In addition, the magnetic moments of Co are also ferromagnetically coupled to the Mn moments.

In order to be able to get insight into the complex coupling, the fundamental mechanisms of ferromagnetic coupling are presented before the special situation in Co_2MnSi will be described.

Quantum mechanical exchange interaction

The quantum mechanical exchange interaction is responsible for the occurrence of ferromagnetism. The magnetic moment of a single atom is caused by the exchange interaction of the electrons within the shells of this atom. In the transition metals the 3d shell is responsible for the atomic magnetic moment. Hund's rule directs the way to calculate the atomic spin moment [16]. Until the half of the shell is filled, all electrons will align their spin in parallel. This makes manganese with five electrons in the 3d shell to be the element with the highest magnetic moment of $2.5 \mu_B$ within the series of the transition elements. Further filling of the 3d shell will add electrons in antiparallel, so that the resulting magnetic moment will be reduced with increasing occupation of the shell. However, as in pure metallic manganese, the atomic magnetic moments does not have to lead to ferromagnetism. The ferromagnetic coupling of the single atomic moments require an additional interatomic interaction. In literature the phenomenon of ferromagnetism is described by various theoretical approaches depending on the elevated magnetic system. To understand the ferromagnetism of the Heusler alloys, four fundamental exchange interactions have to be considered:

- *Band magnetism*

If the magnetic moment is carried by the itinerant conduction electrons, the exact band structure is essential for the occurrence of ferromagnetism. To reveal ferromagnetism, the spin up and spin down band have to be exchange splitted. This will only occur under special conditions. The responsible band structure effect can be demonstrated in the following way:

Starting from two equally occupied sub-bands, the exchange splitted state can be reached as follows: The transfer of a spin down electron into the spin up sub-band requires an increase of its potential energy. To be present this process, the kinetic energy of this electron within the spin down sub-band has to exceed this gain of potential energy. This so-called Stoner criteria fits the 3d transition metals very well [17, 16].

- *Direct exchange*

If the magnetic moment and the electrical current are carried by different types of electrons, one speaks of localized magnetic moment systems. In principle, three types of ferromagnetic coupling can occur. The direct exchange interaction, as direct consequence of the Pauli principle, takes into account the fermionic character of the electrons. The required antisymmetric wave functions reveal different energies for the antiparallel and parallel state in case of a two electron system. This quantum mechanical interaction depends strongly on the overlap of the participating wave functions. For small interatomic distances, antiferromagnetic coupling occurs. At larger distances the coupling alters to ferromagnetic. For large distances the coupling vanishes and paramagnetism is present. This behavior is illustrated in Fig. 1.2 a).

The graph displays the exchange integral, that is negative for antiferromagnetic and positive for ferromagnetic coupling, in dependence of the interatomic distance r_{ab} . If the interatomic distance is too large, as present in most ferromagnetic materials, the direct exchange interaction is too small to mediate the ferromagnetism.

- *RKKY exchange*

The RKKY exchange (after Rudermann, Kittel, Kasuya and Yosida) provides a polarization of the conduction electrons due to the localized magnetic moments. Due to the validity of the Pauli principle, an enrichment zone of spin up electrons has to follow a zone of enrichment of spin down electrons. By this mechanism, an oscillatory behavior of the exchange integral occurs (see Fig. 1.2 b)) with alternating ferro- and antiferromagnetic configuration in dependence of interatomic spacing x up to large distances [18, 16]. This same mechanism is responsible for the antiferromagnetic coupling in multilayer GMR structures of alternating magnetic (Co, Fe) and non-magnetic (Cu, Cr, Ru) [19] thin films discovered by Grünberg in 1986 [20].

- *Super exchange*

In the absence of conduction electrons, RKKY coupling can not be present. Nevertheless, antiferromagnetic coupling can also be observed in MnO and MnF₂ [21, 15]. This finding is attributed to the occurrence of the so-called super exchange. The coupling is mediated by the presence of diamagnetic atoms. The diamagnetic atom provides one electron to the magnetic atom obeying Hund's rules. Hence the diamagnetic ion becomes paramagnetic and couples via direct exchange to the next magnetic atom. This more complex mechanism can initiate ferro- and antiferromagnetic coupling character [22].

How these coupling mechanisms have to be employed for the understanding of the full Heusler alloys will be the subject of the following paragraph.

Ferromagnetic full Heusler alloys

The origin of ferromagnetic behavior in Heusler alloys is complicated and far away from being yet completely understood. Consequently, this paragraph will present a compilation of exchange mechanisms momentarily discussed.

Firstly, a direct exchange coupling is not realistic due to the large interatomic distance of both the manganese and cobalt atoms in Heusler alloys [18]. A description by a mechanism of pure itinerant electrons, as was successfully applied to the 3d transition metals, is also unrealistic due to the localization of the magnetic moments to the Mn atomic sites [25]. However, the presence of two of the transition metals would favor at least a partly band

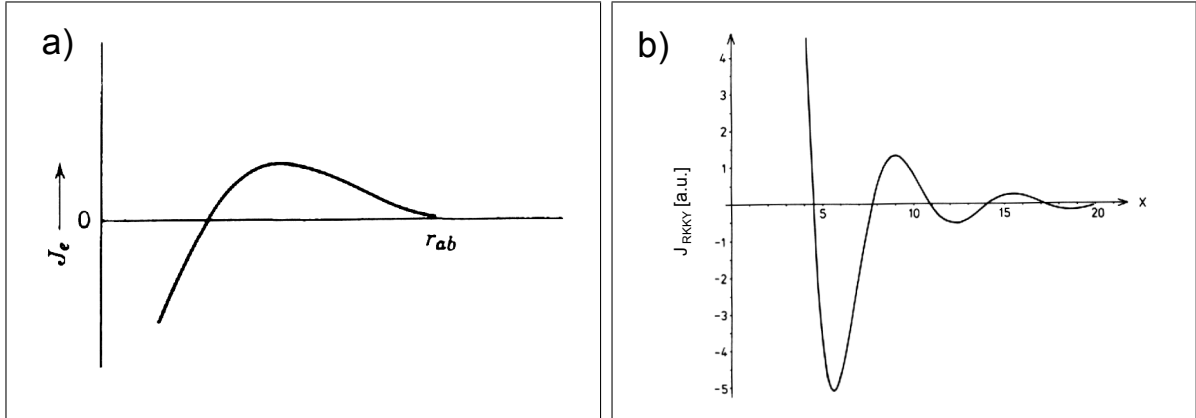


Figure 1.2: a) Evolution of direct exchange integral J_e with interatomic distance r_{ab} (after [23]): at short interatomic distances the direct exchange interaction exhibits antiferromagnetic character; at larger distances the coupling changes to ferromagnetic, before it alters to paramagnetic behavior at even larger distances; b) evolution of RKKY type interaction (after [24]): the RKKY exchange interaction J_{RKKY} varies between ferromagnetic and antiferromagnetic character in dependence of interatomic distance x

like contribution to the ferromagnetic coupling.

Starting from the more simple Heusler alloy Cu_2MnAl , it is possible to extract some features of the essential Mn-Mn interatomic coupling¹. As indicated before, direct exchange is impossible due to the large distance (about 4.2 \AA) [27]. Zener proposed a model including a direct and an indirect exchange mechanism [28]. The direct contribution always provides antiferromagnetic coupling, whereas the indirect interaction via the 4s conduction electrons couples ferromagnetically. Zener's simple model finds its quantum mechanical foundation in the oscillatory RKKY interaction proposed nowadays as the coupling mechanism between separate manganese atoms [29, 14]. In contrast, Kübler makes a mechanism of super exchange type responsible for the Mn coupling [25]. Coupling via the diamagnetic group III-V element can be an alternative or an addition to the RKKY mechanism. In Cu_2MnAl a coupling via the Cu atoms can be neglected. If these Cu atoms are replaced by Co atoms, as in Co_2MnSi , the magnetic configuration becomes more complicated. Kübler again proposes an indirect coupling of the manganese atoms via the cobalt atoms [25]. Alternatively, exchange interaction by means of the common d bands of manganese and cobalt hybridization is utilized in band structure calculations [29].

An exact description of the ferromagnetic coupling in Heusler alloys is currently not real. In recent theoretical investigations three different exchange mechanisms were taken into account [29, 25] to achieve agreement with experimental data.

However, a good understanding of the resulting saturation magnetization in dependence

¹In Heusler alloys containing Mn atoms, the magnetic moment is mainly restricted to the Mn atoms [26]. In the case of Co_2MnSi , the Co atoms additionally contribute to the total magnetic moment.

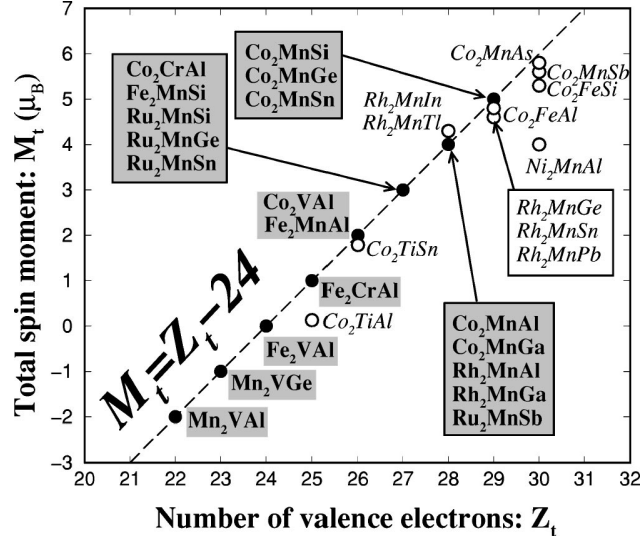


Figure 1.3: Slater Pauling behavior of full ferromagnetic Heusler alloys (after [14]): the number of the present conduction electrons of the group III-V elements determines the resulting total magnetic moment per f.u.

of the constituents is achieved. This results from the well-known Slater-Pauling behavior presented in figure 1.3 for the Heusler alloys and was deduced in [14]. The not completely filled shells of the group III-V elements in the s-p bands determine the resulting magnetic moment. Due to the hybridization with the two other constituents the empty states will be filled by d electrons of manganese and cobalt (for Co_2MnX) and, as a consequence, the spin asymmetry increases or decreases within these atoms. This behavior allows to form Heusler alloys of *any* saturation magnetization by the proper choice of the constituents.

1.1.3 Half metallicity

The term *half metallic* characterizes a spin-split band structure that exhibits different electrical behavior for each spin orientation. In one spin direction (spin up) the conduction electrons exhibit metallic character, where in the opposite spin direction (spin down) semiconducting or insulating behavior is present. This means that the Fermi energy is situated within a gap in the spin down band structure and hence a spin polarization of 100 % at the Fermi level exists². First evidence for the presence of 100 % spin polarization was given by theoretical investigations on half Heusler alloys [2]. De Groot *et al.* predicted NiMnSb to be half metallic. Initiated by these theoretical findings, numerous experimental studies so as to verify the spin polarization followed. These experiments concentrated on the preparation NiMnSb of thin films [30, 31, 32, 33] and to prove their half metallic character, but failed to do so [34, 35, 36]. As a reason for this failure, two aspects are

²Within the framework of this thesis the term *spin polarization* is always meant to be at the Fermi level

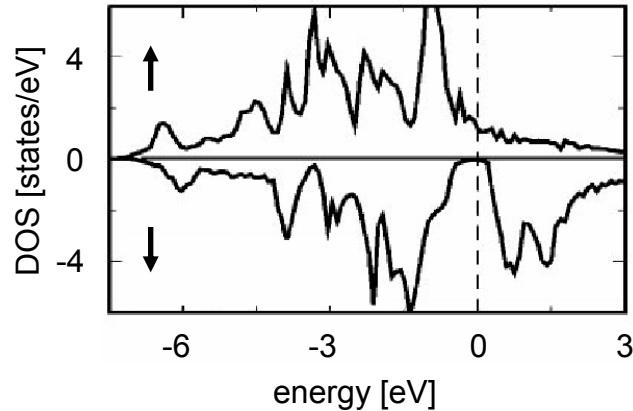


Figure 1.4: Spin-resolved DOS for Co_2MnSi (from [14]) shows the spin-split band structure character with insulating behavior of the spin down electrons

discussed in literature. Firstly, due to the empty fourth fcc lattice antisite disorder effects are more favored [12, 13]. In the picture of the four fcc lattices, the two Ni-sublattices (one is empty) are indistinguishable. The full Heusler L2_1 structure is the more stable phase. And secondly, since in these experiments the spin polarization was determined by surface sensitive techniques (compare also paragraph 3.4), the theoretical predicted missing of half metallicity at the surface [37, 38] can be responsible. Hence full Heusler alloys would be better candidates due to lower tendency to antisite disorder and still half metallic character at the surface/interface for elevated full Heusler alloys [3, 38].

In bulk a lot of the full Heusler alloys show half metallic character [14]. However, first evidence of half metallicity of Co_2MnSi was given in 1998 by Ishida *et al.* [3]. They calculated the energy gap within the spin down band structure to be about 0.4 eV. This would be sufficiently large to provide 100 % spin polarization at room temperature ($k_B T \sim 25$ meV). This is the crucial advantage with respect to half metallic oxides as CrO_2 , $\text{Sr}_2\text{FeMoO}_6$ or $\text{La}_{0.7}\text{Sr}_{0.3}\text{MnO}_3$ showing high spin polarization at low temperatures, but exhibit Curie temperatures under 500 K [39]. Hence no remarkable spin polarization would be present at room temperature. An alternative would be magnetite (Fe_3O_4 : $T_c=858$ K [15]). However, it is hard to prepare due to preparational constrains [39]. Consequently, the full Heusler alloys are the most promising candidates for realizing 100 % spin polarization at room temperature.

The origin of spin polarization is strongly related to the existence of the ferromagnetism. Recently it is not clear if a single physical mechanism can be made responsible for the existence of the gap in the minority band structure. Theoretical investigations concentrate on the band structure calculations within the formalism of the local spin density approximation (LSDA) [29, 38, 14, 3]. Such calculations reveal the spin-resolved density of states for Co_2MnSi presented in Fig. 1.4. The gap for the minority charge

carriers is clearly observable at the Fermi level, establishing the half metallic character. The Co-Mn hybridization is the main key to 100 % spin polarization, whereas, in contrast, the Co-Co hybridization is responsible for the smaller energy gap of the full Heusler alloys with respect to the half ones [14]. However, if the Co-Mn hybridization is present, the Heusler alloys do not have to be 100 % spin polarized. If it is a real half metal or *only* highly spin polarized, depends on the group III-V elements. Its p electrons hybridize with the d electrons of the other constituents to form the bands next to the Fermi level. This formation is influenced by the existent group III-V element in two ways [29] and thus the half metallic character is affected. By determining the lattice constant³, the group III-V element influences the degree of hybridization in the first way. And secondly, it directly determines the density of states by the number of its valence electrons.

In conclusion, this very complex behavior responsible for the half metallic density of states of Heusler alloys makes them very sensitive to small disorder effects [41]. Consequently, the control and suppression of disorder have to be achieved. Additional to these effects concerning the bulk properties, the situation in thin films and at surfaces or interfaces is very different. Too thin or Co-terminated films are theoretically predicted not to be half metallic [3, 41], where Si and Mn terminated surfaces would inhibit half metallicity [42].

1.2 Ordering on atomic scale

As mentioned before, local ordering is essential for the presence of half-metallic character in Heusler alloys. Consequently, local disorder has to be considered. Two approaches to measure the disorder were exploited. One is to monitor electrical resistance and magnetic moment, so as to identify the degree of disorder. The other is a more direct one using x-ray diffraction, where the influence of disorder can be observed by measuring the diffracted beam intensities. However, one disadvantage of all theoretically ordering models available is the limitation to binary alloys. To analyze the microstructural ordering of a ternary alloy such as Co_2MnSi , Webster proposed an extension of the formalism [18].

1.2.1 Ordering parameters

To describe ordering in a formal way, one has to introduce an ordering parameter, which provides a measure for a quantitative analysis. In principle, two kinds of order parameters can be distinguished: short range and long range order. In binary alloys the short range order parameter gives the probability to find a pair (A,B) on two neighboring lattice sites [43]. If the two sites are occupied by a pair (A,B) or (B,A), full order is reached. Hence the short range ordering parameter would not detect an (A,B) switch. In opposite, it reveals deviations of the local environment of an atomic site from the optimum configuration [44].

³Also the choice of the first element (in the present case Co) strongly influences the existent lattice parameter [40].

The long range order parameter displays variation on a large length scale. It is a measure which ratio of type A atoms occupy B sites and vice versa. Within this thesis the emphasis is on the long range order parameter due to degradation of spin polarization resulting from antisite formation [4, 12].

Long range order parameter of binary alloys

The long range order parameter quantifies the degree of interexchange, the B-site occupation of an A-atom and vice versa. In Heusler alloys the local ordering is essential for the half metallic character [3, 41]. Thus, the presence of atoms of type A- on B-sites would sensitively influence the band structure [41]. The long range order parameter S takes into account the fraction n_A of A-atoms located on A-sites [43]:

$$S = 2\frac{n_a}{N} - 1 \quad (1.1)$$

where N is the total number of A lattice sites in the crystal. Equation (1.1) describes the degree of order in binary alloys consisting of A- and B-atoms. If the A-sites are randomly occupied by A- or B- atoms, S becomes zero. In case of perfect ordered unit cell S becomes one.

Extending the ordering formalism to ternary systems leads to a set of order parameters α_x [18].

Extension to ternary alloys

The definition of a single order parameter S , as in binary alloy system, is not possible in ternary systems. The determination by experimental data is difficult and ambiguous. However, to extract information about local disorder from the relative peak intensities in x-ray diffraction experiments, a formalism proposed in [18] is applied here. Not one single order parameter S can be employed, but instead seven parameters α_x . Then the disorder parameter α_{X-Y} reveals the fraction of Y-atoms on X-sites. Thus, in contrast to the order parameter S , the disorder parameter α_x is 0 for perfect order and 0.5 for completely random interexchange. In table 1.1 the effective scattering factors of the seven principal disorder types are listed for each sublattice (A, B, C, D). For Co_2MnSi X, Y and Z have to be replaced by Co, Mn and Si, respectively. Row 1 displays perfect order. In the second and third one antisite disorder of manganese atoms with one Co-sublattice (A) and both Co-sublattices (A, C) is summarized. At this stage of discussion the distinction between interexchange with one or both Co-sublattices seems to be senseless. However, the scattering structure factor, which mainly contributes to the diffracted beam intensity in x-ray experiments, is sensitive to these two interexchange types. The next two rows account for Co-Si disorder. The following row describes Mn-Si interexchange, before the last indicates random disorder, which means interexchange between all four sublattices.

How the order-disorder relation is experimentally determined, is described in the subsequent paragraph.

1.2.2 Determination of the disorder parameter

In order to determine the type and the degree of disorder, two experiments are suitable. Diffraction of neutrons or x-rays can be used to detect the scattering amplitudes quantitatively. Due to its higher accuracy in determining the intensities and strong dependence of intensity from angle position, neutron diffraction would be the favored method [18]. In addition, it provides the magnetic information of the atom as a result of the interaction of the neutron spin with the nucleus spin [18]. Hence the element-specific atomic magnetic moment in Co_2MnSi can be derived [9]. However, a neutron beam source is not that common, even today. Consequently, in this work x-ray diffraction is applied to determine the type of disorder.

Before the disorder mechanism will be discussed, the experimental technique is outlined.

Peak position and intensity

If an electromagnetic wave hits the surface of matter, a lot of physical interactions are possible. Some of these are fluorescent x-rays, transmission of incident beam, electron emission or scattered x-rays [45]. Even for x-ray scattering, two processes can be distinguished. By Compton scattering the phase information of the reflected beam is lost and, consequently, cannot interfere with other reflected x-rays. In contrast, the coherent scattering by tightly binding electrons provides a phase shift of $\frac{\pi}{2}$ for all reflected rays, which preserves a constant relative phase relation [46]. This coherent x-ray scattering is the one of interest in x-ray diffraction experiments.

The incoming photons hit the first crystal plane of the sample and are reflected or transmitted. The transmitted ones experience the same procedure at the following crystal planes. The resulting reflections interfere at a position of the detector. For the interference present at an angle θ , constructive superposition is achieved at [46, 47]:

$$2d_{(hkl)} \sin \theta = \lambda, \quad (1.2)$$

where λ is the wavelength of the beam and $d_{(hkl)}$ is the lattice plane distance of a chosen lattice direction $[hkl]$. The Bragg equation lets one calculate the complete set of peaks apparent in the XRD pattern of a known microstructure. Or knowing λ and all θ , the lattice parameter of an unknown material can be deduced.

From the Bragg equation (1.2) point of view all (hkl) combinations are possible. However, not every class of planes reveals a finite intensity, since the internal structure of the unit cell determines the annihilation of peaks by destructive interference.

The intensity of the reflected beam is a superposition of several effects. The derivation of the exact form of the peak intensities can be found in fundamental x-ray diffraction

| Type of disorder | f_A | f_B | f_C | f_D |
|------------------|--|--|--|--|
| L2 ₁ | f_X | f_Y | f_X | f_Z |
| X-Y | $(1 - \alpha)f_X + \alpha f_Y$ | $(1 - \alpha)f_Y + \alpha f_X$ | f_X | f_Z |
| X-Y-X | $(1 - \frac{\alpha}{2})f_X + \frac{\alpha}{2}f_Y$ | $(1 - \alpha)f_Y + \alpha f_X$ | $(1 - \frac{\alpha}{2})f_X + \frac{\alpha}{2}f_Y$ | f_Z |
| X-Z | $(1 - \alpha)f_X + \alpha f_Z$ | f_Y | f_X | $(1 - \alpha)f_Z + \alpha f_X$ |
| X-Z-X | $(1 - \frac{\alpha}{2})f_X + \frac{\alpha}{2}f_Z$ | f_Y | $(1 - \frac{\alpha}{2})f_X + \frac{\alpha}{2}f_Z$ | $(1 - \alpha)f_Z + \alpha f_X$ |
| Y-Z | f_X | $(1 - \alpha)f_Y + \alpha f_Z$ | f_X | $(1 - \alpha)f_Z + \alpha f_Y$ |
| X-Y-X-Z | $(1 - \frac{2}{3}\alpha)f_X + \frac{\alpha}{3}(f_Y + f_Z)$ | $(1 - \alpha)f_Y + \frac{\alpha}{3}(2f_X + f_Z)$ | $(1 - \frac{2}{3}\alpha)f_X + \frac{\alpha}{3}(f_Y + f_Z)$ | $(1 - \alpha)f_Z + \frac{\alpha}{3}(2f_X + f_Y)$ |

Table 1.1: Effective scattering factors $f_{A,B,C,D}$ for the different types of antisite disorder after [18]; the letters A, B, C and D denote the four fcc sublattices.

textbooks such as of Cullity [46] and Warren [47]. The key contribution to the intensity to be known for investigating microstructural local disorder effects is the structure factor F [48]:

$$I \propto F^2 \quad (1.3)$$

This proportionality of the peak intensity to the square of the structure factor reveals the strong influence of local ordering. Even small deviations from perfect ordering would be detectable by the diffracted beam intensity.

The structure factor

The structure factor takes into account the internal structure of the unit cell. In a simple cubic cell only upper and lower plane of the cube contribute to the reflected intensity. But, for example in a fcc cell, the face-centered atoms introduce an extra plane at half distance of the two initial ones. This extra plane makes some peaks to vanish by destructive interference.

To calculate the peaks allowed in a x-ray diffraction pattern, one has to consider the exact distribution of atoms within the unit cell leading to the general form of the structure factor [48]:

$$F(hkl) = \sum_{k=1}^N f_k \exp(2\pi i n(hu_k + kv_k + lw_k)), \quad (1.4)$$

where (h, k, l) denotes the class of planes reflecting. u_k , v_k and w_k are the individual positions of each atom in the unit cell and the sum is taken over the total number of atoms N of the unit cell. If the unit cell is built up of different kinds of atoms, the individual atomic scattering factors f_k come into account. In case of disorder, the atomic scattering factor at position (u_k, v_k, w_k) has to be replaced by the effective scattering factor $f_{A,B,C,D}$ (see table 1.1) of the elevated sublattice. Its element-specific character is the key to investigate local disorder processes by x-ray diffraction.

The atomic scattering factor

As can be deduced from equation (1.4), the difference in the atomic scattering factors of the different elements in the unit cell gives rise to the difference in the structure factor, when local disorder is occurring. That is because the structure factor includes the atomic positions within the unit cell, whereas the atomic scattering factors take into account the possibility of different atoms on the unit cell sites.

The incident x-ray beam mainly interacts with the electron cloud of each atom. Consequently, the atomic scattering factor is influenced by the arrangement of the scattering

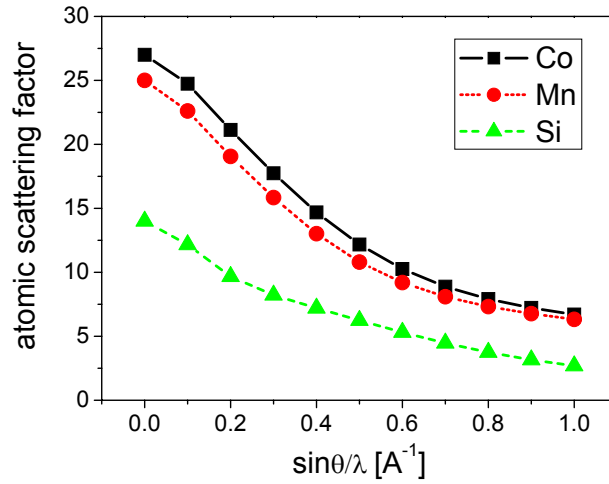


Figure 1.5: Atomic scattering factors of the constituents of the investigated Heusler alloy Co_2MnSi ; the valid range of the used x-ray diffraction system is remarked by $0.057 \text{ \AA}^{-1} \leq \frac{\sin\theta}{\lambda} \leq 0.627 \text{ \AA}^{-1}$ from [46]

electrons of each atom. Thus, the local distribution of electron density $n(\vec{r})$ determines the atomic scattering factor f_k [48]:

$$f_k = f_0 \int dV n(\vec{r}) \exp i(\Delta\vec{k} \times \vec{r}), \quad (1.5)$$

where the integration has to be performed over the complete volume and f_0 is the scattering factor by a single electron. The exponential factor respects the retardation by reflections of the different electrons analogue to the structure factor.

In the typical Bragg configuration (incident angle = reflecting angle), the atomic scattering factor is dependent on the wavelength λ and the Bragg angle θ , both included in the factor $\frac{\sin\theta}{\lambda}$. The detailed characteristic is displayed in plot 1.5 for the elements Co, Mn and Si. In case of large wavelengths or small Bragg angles, the atomic scattering factor equals the number of electrons present in the atom. Within this work, the wavelength is that of $\lambda = 0.154056 \text{ nm}$ (Cu-anode) and the angle varies from $\theta = 10\text{-}150^\circ$ resulting in the range of $0.057 \text{ \AA}^{-1} \leq \frac{\sin\theta}{\lambda} \leq 0.627 \text{ \AA}^{-1}$.

For completeness, the author wants to refer to anomalous dispersion corrections. These occur if the incident x-rays can raise an electron into higher energy levels and the following recombination emits an x-ray quantum of the same wavelength but without phase information.

1.2.3 Evolution of structure factor with ordering

After this general introduction of the two terms structure factor and atomic scattering factor, a detailed calculation for Co_2MnSi will enable to measure the order-disorder relation for this material with x-ray diffraction.

Calculation for Co_2MnSi

As has already been mentioned, the Co_2MnSi Heusler alloy exhibits a microstructure of four interpenetrating fcc-lattices. For fcc-lattices, in general, three types of apparent reflecting planes can be identified. Firstly, only (hkl) planes with all even ((220) and (200)) or all odd (111) miller indices result in a non-vanishing intensity. Additionally, the planes with even indices are distinguished into the even (220) and odd (200) ratios of $(h+k+l)/2$. The calculation of the square of the corresponding structure factor F^2 reveals:

$$F^2(220) = 16(f_B + f_D + f_A + f_C)^2 \quad (1.6)$$

$$F^2(111) = 16[(f_B - f_D)^2 + (f_A - f_C)^2] \quad (1.7)$$

$$F^2(200) = 16(f_B + f_D - f_A - f_C)^2 \quad (1.8)$$

where $f_{A,B,C,D}$ is defined with respect to the presence of the four fcc-sublattices and equals the effective scattering factors in table 1.1. In case of perfect ordered unit cell, the factors $f_{A,B,C,D}$ have to be replaced by $f_{\text{Co},\text{Mn},\text{Co},\text{Si}}$, respectively.

The structure factor $F^2(220)$ is characterized by the sum of all atomic scattering factors. Thus, it is clear that even in the presence of disorder, the resulting peak intensity will stay unchanged. This identifies these planes to be *fundamental* ones, being always apparent with the same intensity and hence can serve as normalization factor so as to cancel out influences of the experimental setup.

In contrast, the intensities of the two other classes behave very sensitively to disorder processes, indicating already minor changes of order in the unit cell and hence are named *superlattice* reflections. The evolution of the peak intensity as a function of the degree of disorder is displayed in figure 1.6 for both superlattice peaks (111) and (200). For clarity in the discussion of the experimental results: normalized or relative peak intensity means measured peak intensity divided by the measured intensity of the (220) peak.

The calculation was done with respect to effective scattering factors (Tab. 1.1) and use of equations (1.6)-(1.8). The atomic scattering factors $f_{X,Y,Z}$ are put in the effective atomic scattering factors for each sublattice $f_{A,B,C,D}$, where α_x employs the disorder dependence. If these effective scattering factors are inserted in equations (1.6)-(1.8), a disorder dependent structure factor is the result.

The evolution clearly indicates the strong correlation of peak intensity with increasing normalized disorder parameter α_x . For example, a Co-Mn antisite disorder of 10% would decrease the normalized peak intensity by 20% in both classes ((111) and (200)). Also remarkable is that a Mn-Si disorder will increase the (200) intensity. Hence high (200)

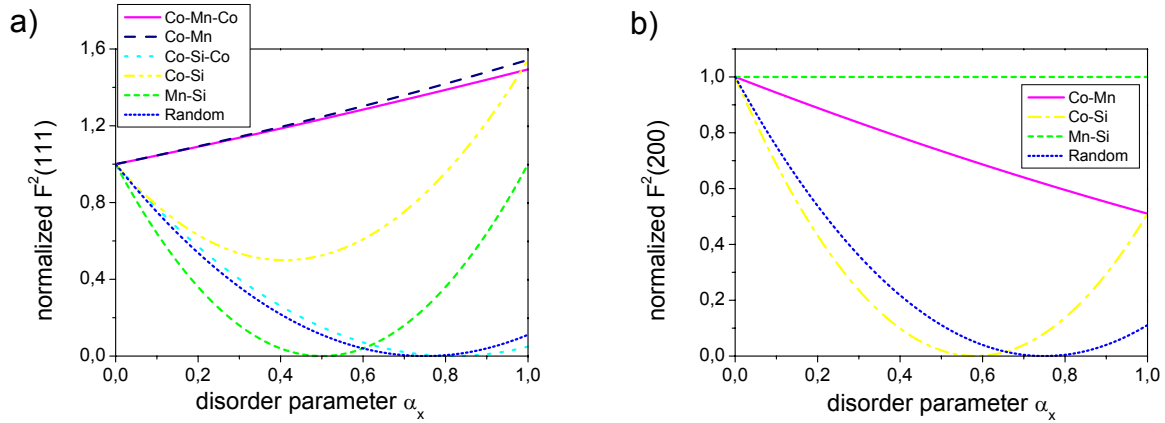


Figure 1.6: Influence of local disorder on the scattering structure factors: a) (111) and b) (200) in Co_2MnSi ; the calculations are done with respect to atomic scattering factors of Co, Mn and Si and to effective structure factors

peak intensities do not have to represent a high degree of order.

In conclusion, the proposed technique enables one to determine the type of disorder by combination of the evolution of the two superlattice lattice peaks (111) and (200). A quantitative investigation would need a reference sample with perfect crystalline structure to determine the exact deviation of peak intensity and to extract the absolute degree of disorder. However, such a perfect crystalline sample was available. Thus, for qualitative characterization, an additional parameter, indicating the direction of local disorder, is needed. In case of Co_2MnSi the saturation magnetization may serve as such a parameter in the way that only a perfect ordered unit cell will provide maximum magnetic moment [41]. Then the evolution of peak intensities with saturation magnetization can deduce the type of disorder.

In the end, three remarks concerning the formalism have to be given. Firstly, this formalism does not include deviation of measured peak intensities from calculated ones by texture formation. Consequently, the reduced (400) intensity of a (110) textured sample makes the identification of local disorder impossible. Therefore, this formalism needs to prepare perfect polycrystalline samples in the way that all crystal orientations are equally distributed. Secondly, degrees of disorder higher than $\alpha_x = 0.5-0.8$ are not possible, if the general x-ray pattern is that of Co_2MnSi . High degrees would result in a different fundamental unit cell and the characteristic XRD pattern of the $L2_1$ structure is lost [18]. Thirdly, the peak intensity described here is defined to be the total integrated intensity of the peak. In the experimental investigation the discussion will be reduced to the maximum peak intensity. This approach is only valid due to the fact that the peak widths for the peaks (111), (200) and (220) of investigated samples were nearly identical for all samples. Thus, the maximum peak intensity is equal to integrated intensity despite a constant factor. This factor vanishes for the investigated relative peak intensities.

Chapter 2

Preparation I - Co_2MnSi thin films

Before the spin polarization of Co_2MnSi Heusler alloy in thin films can be determined, full understanding of the growth of thin films (~ 100 nm) is required in order to experimentally realize appropriate samples. This chapter will introduce the experimental techniques for deposition, sputtering and annealing, and additionally inform about substrate material, substrate orientation, the necessity of a seed layer and the temperature-time window for annealing.

Various techniques for thin film deposition can be used depending on the material and aiming for special application [49, 50]. One of these techniques is magnetron sputtering used in DC or RF mode [51, 52]. It is characterized by high deposition rates and homogeneity over large lateral dimensions [52]. Thus, the paragraph 2.1 will describe experimental parameters and characteristics for the Leybold sputter systems, which have been employed for thin Co_2MnSi film preparation.

In literature it is reported that Co_2MnSi thin films were prepared on heated substrates to achieve polycrystalline [7] or (110) textured [5] growth. This annealing has let to install a contactless heating system in one of the two sputter systems within the framework of this thesis. Details are given in paragraph 2.2 together with experimental data on the quality of the prepared films.

Recently, silicon oxide (SiO_2) [7] and sapphire (Al_2O_3) with vanadium seed layer [5] have been used to realize the L_{21} Heusler phase. To get a complete understanding of the influence of the substrate material including the seed layer and orientation, various materials are tested. The results of these investigations will be presented in paragraph 2.3.

2.1 The sputtering system

Thin film processing makes high demands on the experimental setup of the sputtering facilities. Especially the demand for ultra fine vacuum, full control of deposition yields and film roughness are important. For mastering these requirements, film deposition is accomplished in two very similar DC/RF magnetron sputtering system, both manu-

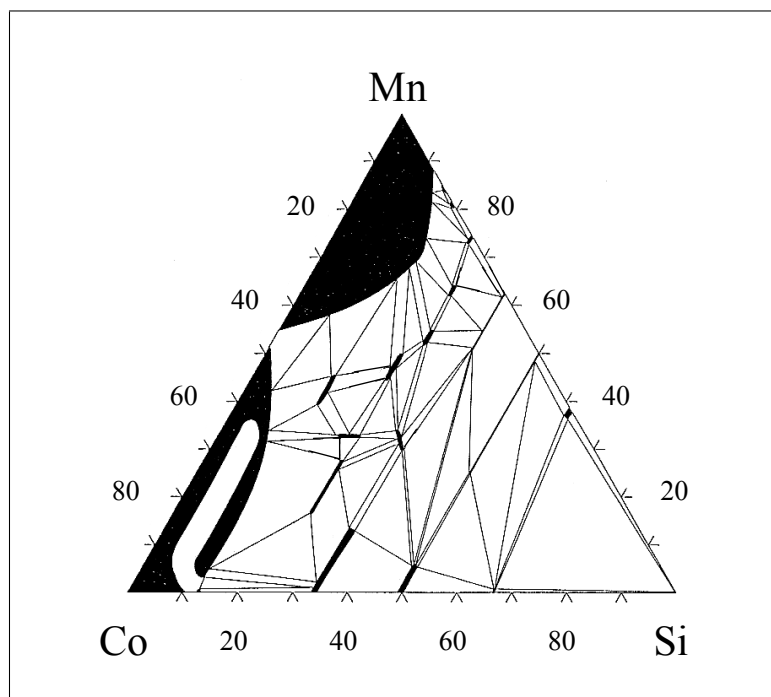


Figure 2.1: Phase-diagram of the system Co-Mn-Si at 800°C after [53]

factured by Leybold Systems Dresden. The principle assembly is given in the following and is identical for both systems. To distinguish the two systems, they will be named system I and system II. System I exhibits 6 sputter sources and the possibility for in-situ plasma oxidation. System II possesses 4 sputter sources and the possibility for heating the substrate during the sputter deposition process. This makes system II the preferred one for the initial investigations concerning the principle growth conditions.

To ensure best film preparation conditions, the deposition chambers of both systems are evacuated by a three-step pump system. By this assembly a basis pressure of 2×10^{-7} mbar (system I) and 5×10^{-7} (system II) is reached. To achieve moderate deposition yields and sufficiently smooth films, sputtering power and sputtering argon pressure are the variables to be controlled. By managing the sputtering pressure to 1×10^{-3} mbar and the sputtering power to about 100 W, typical sputtering yields of 0.3 nm/sec are reached. The typical rms-roughness is determined to be in the range of $0.2\text{-}0.4 \text{ nm}$ ¹.

For establishing a ternary alloy of defined stoichiometric ratio, in principle, three techniques are suitable, enabling good stoichiometric quality. These are very critical to prepare the L_{21} phase with Co 50 at%/Mn 25 at%/Si 25 at%, which has a very narrow existence range according to the cross section at $T = 800^\circ\text{C}$ of the ternary phase diagram 2.1. The silicon ratio has to be adjusted very accurately. Atomic deviations in the range

¹The rms-roughness is defined by the root mean square of the difference between the height of each point in the area and the mean height summed over the total area. The rms-roughness determination is always performed by atomic force microscopy (AFM) over an area size of $500 \times 500 \text{ nm}^2$.

of 1% make the $L2_1$ Heusler phase vanish. In contrast, for the cobalt and manganese concentration higher deviations are allowed. The cobalt ratio can range from 48% to 60%, the manganese from 15-27%.

To deposit alloys of defined stoichiometric ratios, the possible techniques are co-evaporation, multilayer deposition and sputtering from a stoichiometric target. The co-evaporation and multilayer deposition would sputter from single-element targets. During co-evaporation, atoms of all materials are simultaneously reaching the substrate surface to form the desired alloy. Therefore, the sputter sources have to be situated very close to each other. The existing sputter systems are not constructed for this purpose. In contrast, they ensure undiluted deposition of the single target material without any input of impurity atoms of neighboring sputter sources. This makes the technique of co-evaporation impossible in the present sputter systems.

Alternatively, multilayer deposition employs altering layers of the desired elements. Afterwards the resulting layered structure demands for an annealing procedure to ensure an intermixing of the single layers and to form the stoichiometric alloy. However, assisted by the layered superstructure, partial formation of non-stoichiometric stable alloys can occur and would prevent homogeneous and stoichiometric samples [54].

To ensure homogeneous stoichiometric films in the present sputter system setup, the third technique of sputtering from a stoichiometric target is the best choice. The stoichiometry, which is defined by the target, will occur on the substrate surface and the homogeneity is present a priori. However, two restricting factors are existent for this technique. Firstly, adjusting the stoichiometric ratio is impossible after the target has been produced. Hence, defined investigations of the influence of stoichiometric variations are out of scope of this technique. Secondly, production of the stoichiometric target is a critical process depending on the selected components. High melting elements and materials are very hard to process. Therefore, powder samples of the components are mechanically mixed and subsequently hot-pressed [55]. The hot-pressed targets exhibit a grain-type microstructure in the sub-100 μm -range [56] and are brittle. This last aspect demands for a mechanical stabilization by bonding onto a 1-2 mm thick copper plate [56] to prevent breaking of the target.

2.2 Annealing process

To provide the possibility to sputter on heated substrates, an infrared emitter heating system was installed in sputter system II. By emission of radiation with a maximum intensity at a wavelength of 1.25 μm [57], contactless heating of the sample is possible. Together with a transfer chamber this technique enables one to transfer various samples into the main sputter chamber without breaking vacuum and to process a lot of samples in short time. The three incorporated infrared emitters produce a maximum power of 800 W resulting in a maximum substrate temperature of 700 °C . To record and control the substrate temperature, a copper plate contacted with a thermocouple was positioned between substrate and emitters. A typical annealing process needs about 30 min to reach

| m [μ_B per f.u.] | reference |
|-----------------------|-------------|
| 4.940 (bulk) | theor. [14] |
| 4.96 (bulk) | exp. [9] |
| 4.9 ± 0.25 | exp. [7] |

Table 2.1: List of theoretical and experimental values of magnetic moment per formula unit; at a lattice constant of 0.564 nm a magnetic moment per formula unit of $4.94 \mu_B$ corresponds to a saturation magnetization of 1023 kA/m

temperatures of 600 °C. Since the temperature control cannot be in direct contact with the substrate so as not to influence the thin film growth, the measured temperature is only a lower limit ².

The cooling process is without any active cooling. In summary, the combination sputter chamber and heating system enables one to deposit thin films with smooth surfaces onto heated substrates. Alternatively, a room temperature sputter process followed by an in-situ post annealing procedure is also possible with that system.

Due to the limited accuracy of the exact temperature determination during in-situ annealing, an additional oven is in use. This oven provides temperatures up to 550 °C and is described in detail by [58].

2.3 The choice of substrate

From literature it is well known that polycrystalline [7] and (110) textured [5] can be prepared. The polycrystalline samples were deposited on SiO₂ substrates, whereas the (110) textured samples were deposited on sapphire substrate with vanadium seed layer. However, both experiments are characterized by a substrate temperature T_{sub} during deposition in the range of 400-500 °C. To reproduce this finding, silicon oxide and sapphire with vanadium seed layer as well as magnesium oxide (MgO), strontium titanate (SrTiO₃) and silicon substrates are heated up to 450 °C during Co₂MnSi deposition. For silicon, the two crystallographic orientations (100) and (111) are considered. To judge the microstructural quality of these samples, x-ray diffraction (XRD) is employed and the measured relative peak intensities are compared to a calculated reference data set [11]. The resulting intensities are displayed in Fig. 2.2 for all substrate materials. The most intense peaks ($I(\text{hkl})/I(220) > 1$) are completely existent. This reveals a polycrystalline growth with characteristic XRD pattern in Fig. 2.3 a) on heated substrate independent of substrate material. These results confirm the investigations on polycrystalline samples [7], but disprove the ones on (110) textured samples [5].

If the high substrate temperature deposition always reveals polycrystalline growth in the

²Reference measurements reveal deviations in the range of 50-100 °C. This should be hold in mind, when discussing the optimal temperature range.

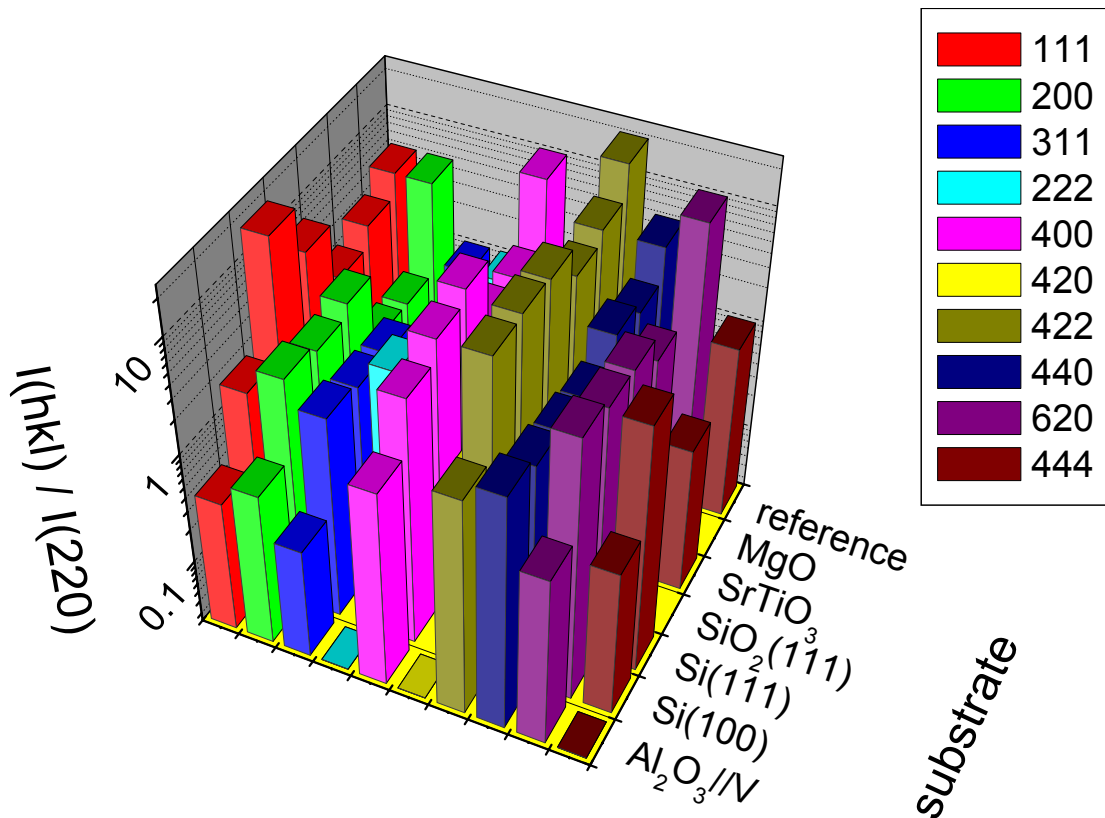


Figure 2.2: Overview of studied substrates for polycrystalline growth deposited at 450 °C and in comparison with calculated reference data [11] (normalized intensities of peak (hkl))

present case, room temperature preparation may support different growth modes. This assumption has been tested for all previously mentioned substrates. The typical XRD pattern in Fig. 2.3 b) for silicon oxide (111) reveals only one very wide peak in width of 5° at position of the (220) peak. The presence of this most intense peak with this tall width points to very small grains ~2-3 nm or amorphous growth.

Now the idea arise, if vanadium as seed layer can enhance (110) texture at high substrate temperatures, then a vanadium buffer can do the same at room temperature. To prove this, for the first, the growth of the vanadium buffer has been tested on various substrates. All substrates ensure a (110) texture in the vanadium film with highest degree of texture on the (111) silicon with 5 nm oxide on top. For a subsequent deposition of Co₂MnSi, a 42 nm thick vanadium seed layer has been prepared. And in fact, the room temperature deposition of Co₂MnSi on a 42 nm seed layer reveals (110) textured growth as can be seen in Fig. 2.3 b). Additional to the (110) and (220) peaks of the vanadium the (220) and (440) peaks of Co₂MnSi are present. This clearly points to the formation of (110)

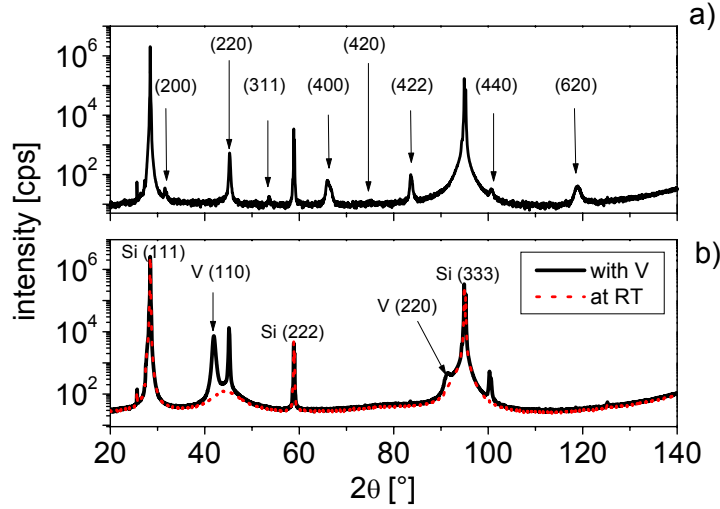


Figure 2.3: a) Typical XRD pattern of polycrystalline sample prepared on heated substrate ($T_{\text{sub}} = 450^\circ\text{C}$ on SiO_2 (111)); b) influence of vanadium seed layer on the growth of Co_2MnSi at room temperature: without vanadium seed layer only amorphous growth, but with V buffer (110) texture is present

textured growth. This fine enhancement of growth of Co_2MnSi at room temperature can be addressed to the small lattice misfit between the two (110) orientations in vanadium and Co_2MnSi . The misfit is estimated to be 4% [59].

However, the room temperature deposition reveals in both cases a poor result in the magnetometric characterization. Only $0.25 \mu_B$ per formula unit is determined in contrast to the experimental and theoretical values in Tab. 2.1. This finding can be due to a two phase film. A small volume $\sim 5\%$ is (110) textured, where the rest volume is in the amorphous phase [60]. A post annealing procedure is thought to order the complete sample into the (110) textured phase. To test a post annealing procedure on (110) textured films as well as to completely characterize the polycrystalline samples, both growth modes are studied in chapter 4. As substrate materials natively oxidized (5 nm) (111) silicon and thermally oxidized (100 nm) (100) silicon substrates are employed in the following.

Chapter 3

Characterization

Before going into detail on the different characterization techniques, some remarks are necessary. This chapter is not to describe the methods and technical parameters in detail. The paragraphs are addressed to briefly explain the physical background of the techniques and aim for pros and cons for the application of each method used.

3.1 Magnetic measurements

Since the Heusler alloys are half-metals and therefore ferromagnets, magnetic characterization is essential. In the present thesis two techniques have been used. For qualitative and very quick measurements MOKE has been employed. Its main disadvantage is the lack of the absolute magnetic moment. Thus, the Alternating Gradient Magnetometer (AGM) technique has also been employed to determine the saturation magnetization.

3.1.1 Magneto-optical Kerr effect (MOKE)

The Magneto-Optical Kerr Effect (MOKE) is based on the interaction of polarized light with magnetic matter. An incident linearly polarized beam is reflected by the magnetic samples and experiences the transformation to elliptical polarized light. The detection of the Kerr rotation enables to measure a signal that is proportional to the magnetic moment of the ferromagnetic sample [58]. Since this signal depends on the magnetic material, the exact determination of absolute magnetic moment is hard to achieve. The hysteresis loop of the sample can be taken in a normalized manner, where the information concerning the coercivity can correctly be extracted. A nice description of the MOKE effect and its application to thin magnetic films is given by [61].

Due to its surface sensitivity, the MOKE experiment is restricted to a magnetic volume of a few nanometers in depth (~ 10 nm [62]). On the other hand this allows to perform surface sensitive magnetic characterization, but it reveals the disadvantage of being

limited in volume. The integration of the magnetic layers into a complex layer stack therefore makes their magnetic behavior not available at the surface. Consequently, the upper layers have to be removed by ion etching to get the magnetic information. Hence, magnetic tunnel junctions are alternatively characterized by AGM.

Due to this disadvantage, MOKE is not mainly used, but the more favorable AGM technique, which provides the absolute magnetic moment and is volume sensitive.

3.1.2 Alternating Gradient Magnetometer (AGM)

If a magnetic sample is placed into an inhomogeneous magnetic field, the sample experiences a force towards the highest field gradient. This force is proportional to the magnetic moment of the sample. So as to determine the magnetic moment of the sample, the acting force has to be measured. Hence, the principle of the alternating gradient magnetometer (AGM) is to position a magnetic sample into an alternating magnetic field. The responding force on the sample is detected by piezo-electrical crystals and transformed into a voltage employing the Lock-In technique [62]. The complementary technique to AGM is the Vibrating Sample Magnetometer (VSM), where the field is not varied, but the sample is vibrating [52]. This *gradient field* varies in orders smaller than the coercive fields of the investigated sample and is applied by small coils placed in the greater field coils providing the magnetic bias field.

The main advantages with respect to MOKE are the volume and the absolute magnetic moment sensitivity. This allows to investigate complex stack geometries without any further preparational efforts and enables to study the magnetic moment or saturation magnetization in a quantitative manner.

However, the most significant disadvantage is the poor signal-to-noise ratio for samples with small coercive fields resulting in small gradient fields, which causes the magnetic force to be smaller. To smoothen the magnetic curves, an increase in the integration time or the increase of the magnetic volume is necessary. Consequently, the *standard* sample size is 100 nm thick ¹. The lateral dimensions are restricted to areas smaller than $4 \times 4 \text{ mm}^2$ so as to fit into the sample holder of the AGM.

All magnetic measurements are performed parallel to the film plane because of the thin film geometry, which forces the magnetic moment to be in plane ².

¹Here comes apparent the great advantage of MOKE. Independently of magnetic behavior, the MOKE experiment always provides experimental results of unchanged, good quality in a very short time.

²The in-plane magnetic behavior of the Co_2MnSi thin films shows a soft magnetic switching with a remanent magnetization very close to the saturation magnetization (4.1.2 and 4.2.2) and in correspondence with theoretical [14, 29] and experimental investigations [9, 5, 63, 7, 4].

3.2 Transport measurements

The transport of electrical charge carriers provides a lot of information. Firstly, the electrical resistivity of a single Co_2MnSi film is an indicator for solid state excitations and disorder effects due to phonons and impurities [43].

More so, the tunneling process in magnetic tunnel junctions can be characterized by its electrical behavior. A tunneling process provides parabolic conductance-voltage (G - V) characteristics [64]. By the special form, information about the quality of the barrier and the involved interfaces can be deduced [65]. Inelastic electron tunneling (IET) processes can be identified by the 1st derivation of G - V -curves ($\frac{d^2I}{dV^2}$ - V) [66].

To the last, the determination of tunnel magnetoresistance (TMR) is performed by resistance measurements in dependence of applied magnetic field.

To distinguish these electrical characteristics from solid state excitations (e.g. phonons and magnons), present at room temperature [67, 66, 58], the samples are cooled down to 10 K in an Oxford Instruments cryostat.

3.2.1 Measurements at room temperature

To determine the electrical resistivity, a 4 point DC probe technique is performed [68]. The exact absolute resistivity is very hard to determine due to two preparational reasons. Firstly, the distance between the voltage contacts is kept fixed at 4 mm, where the width is 15 mm. This geometry will not result in an exact determination of resistivity due to the short measurement length with respect to the small width [68]. The determination becomes more inaccurate by the use of vanadium as seed layer in the textured films. This makes the current distribution in Co_2MnSi more incalculable and, therefore, only relative conclusions on evolution of resistivity can be made.

To force the electrical current to flow through the insulating barrier, the electrical current geometry has to be perpendicular to the film plane. Therefore, the electrical characterization concerning the magnetic tunnel junctions (G - V and TMR) was performed in a 2 point probe assembly. This is made possible due to the large resistance of the tunnel barrier (5-500 k Ω) with respect to the small resistance of the leads ($< 1 \Omega$). The magnetoresistance (TMR) is provided by measuring the resistance of the samples, when varying the external magnetic field over the range of -350-350 mT. During a TMR measurement the bias voltage amounts to 10 mV.

The characterization by current-voltage (I - V) and conductance-voltage (G - V) curves can establish a lot of information about the exact atomic arrangement within the barrier and at its interfaces [65, 69]. Typical I - V -characteristics were performed up to voltages of 500 mV. By measuring the I - V -curves in the parallel and antiparallel state, the bias voltage dependence of the TMR amplitude is generated, which also provides information about the barrier quality in a more qualitative manner.

To record the inelastic electron tunnel spectra (IETS), the measurement unit was modified by Lock-In technique to enhance the signal-to-noise ratio. More details concerning IETS

are presented separately in chapter 7.

3.2.2 Temperature dependence

At room temperature ($k_B T \sim 25$ meV), solid state excitations are activated. In magnetic tunnel junctions mainly phonon and magnon excitations contribute to the temperature dependence of the magnetoresistance due to interactions with the tunneling electrons. Consequently, by *freezing out* these excitations the intrinsic TMR effect can be extracted [10], which reveals the *real* spin polarization of the magnetic electrodes and uncovers imperfections within the barrier [70, 71]. Additionally, magnon excitations within the magnetic electrodes vanish and give account to the full spin polarization, if it is assumed that the spin polarization is connected to the $T^{\frac{3}{2}}$ -law [72, 73].

To provide this bit of information within the framework of this thesis, a cryostat by Oxford is used. It enables one to cover the temperature range from room temperature down to 10 K. The installed air coil reaches 180 mT, which can not saturate the exchange biased upper electrode in MTJs at low temperature. However, this is not critical due to the low coercive fields of Co_2MnSi at low temperatures.

3.3 Atomic arrangement on nanoscale

The study of the atomic ordering in magnetic tunnel junctions containing Co_2MnSi as one electrode is based on two considerations. One aspect is the local ordering within the Co_2MnSi films. Only a perfect ordered unit cell in the Co_2MnSi alloy can provide the full 100% spin polarization [41]. One effective technique to determine the order-disorder relation is to analyze the intensities of x-ray diffraction patterns. Besides the ordering of the Heusler phase, x-ray diffraction additionally provides information about lattice constant, grain size and orientation of grains, which also reflects the local ordering.

In addition, the quality of the AlO_x barrier is equally essential. Only a perfect barrier will result in high TMR amplitudes even at room temperatures [69, 65]. As proposed in the previous paragraph, the electrical characterization as well provides information about these aspects, but more indirectly. Auger electron spectroscopy (AES) [65] and x-ray magnetic circular dichroism (XMCD) [74] achieve stoichiometric and magnetic information of a few monolayers (3-5 [75]) and can uncover the microstructure at the barrier interface [76, 77].

3.3.1 X-ray diffraction

X-ray diffraction characterization is performed by an X'pert PRO MPD diffractometer by Philips. A copper anode running at 2 kW is used with a wavelength of $\lambda = 0.154056$ nm for

Cu K_{α_1} . For calculation, the average of K_{α_1} and K_{α_2} is taken as $\lambda = \lambda_{av} = 0.154184$ nm. The sputter yield determination has been performed on approximately 30-50 nm thin films in the 2θ range 0-10°, since in this thickness range the determination works very well with highest accuracy. X-ray irradiation of films in this small angle range employs the reflection on the interfaces between individual layers. Therefore, such an experimental setup is named x-ray reflectometry. The corresponding estimation of the film thickness by the x-ray pattern is complicated and can clearly be followed in [45]. The so-called *Gonioscans* in the range $2\theta = 10 - 150^\circ$ are based on the Bragg equation (1.2). The typical step width and integration time per step were 0.04° and 20 sec.

The Bragg equation enables to determine the lattice constant by knowledge of the peak position θ , beam wavelength λ and the Miller indices, which are extracted by comparison to a reference database [11]. Then the distance of the diffracting planes is connected to the lattice constant a by the following formula [15]:

$$a = d_{hkl} \sqrt{h^2 + k^2 + l^2} \quad (3.1)$$

Additional to the peak position, the peak shape reveals information about grain size and grain orientation both in direction perpendicular to the film plane.

Peak width - grain size

Theoretically the peak produced by a single crystalline sample is a delta function. The Bragg equation (1.2) is only fulfilled for one exact peak position 2θ . Real measurements reveal a from zero different value for the full width at half maximum (FWHM). This is due to two reasons:

I. Firstly, an instrumental broadening in wavelength is present due to several instrumental and geometrical aspects [45]. This results even for single crystalline silicon substrates in FWHM of 0.01° ³. When calculating the grain size, this has to be taken in account by subtracting the *instrumental* peak broadening from the measured peaks.

II. Further broadening appears by the real grain morphology. Small deviations from the exact peak position already result in a vanishing of the intensity. This is due to destructive interference of reflections from corresponding planes and in the presence of real and finite grains no corresponding planes can be found. This means that finite crystal sizes provide finite FWHM values [46]. The grain size of the crystallites in normal direction is connected to the FWHM of the peak by Scherrer's formula [78]:

$$\delta = \frac{K\lambda}{\text{FWHM} \cos \theta}, \quad (3.2)$$

δ gives the grain size, where λ and θ are the selected wavelength and the Bragg angle. The factor K is the shape factor and is set to 0.9 for cubic crystal structures [46]⁴.

³This line broadening of peaks of single crystalline silicon substrate is present in all XRD measurements.

⁴The $L2_1$ structure of Co_2MnSi is of cubic character.

Absolute measurements of the grain size is very difficult, since it requires the knowledge of the additional broadening due to stress in thin films [45]. However, it is safe to conclude on the relative evolution of the grain size, if the deposition conditions are varied.

Peak height - degree of texture

Besides position and FWHM, the peak intensity is also of importance. For polycrystalline powder samples the relative peak intensities can be exactly calculated. However, especially in thin films, a pure polycrystalline configuration is hard to realize. Due to substrate or seed layer induced stress, the films commonly show textured growth [46, 45]. For preparation of a powder sample, the volume of a film is normally too small. Consequently, deviations from calculated peak intensities are a problem. Additional to the formation of textured growth, local disorder processes can alter the intensity, as discussed in paragraph 1.2.3. Therefore, the measured peak intensities can only be taken as a rough estimate of the degree of texture [46].

A more detailed analysis of texture is available using the technique of *pole figures* [46, 79]. It provides quantitative information on the present texture of the sample. However, within this thesis pole figures are not investigated because of two reasons. Firstly, the Philips diffractometer is not equipped with a Euler cradle. Secondly, by sputtering and heat treatment, one expects randomized orientation with respect to the in-plane orientations of the grains. However, the sample can be tilted around the axial orientation of the normal film direction. Therefore, so-called rocking curves can be taken to analyze the degree of texture. The width and the intensity of the peaks at fixed Bragg condition will serve as parameters for the discussion of texture.

For a complete introduction of texture analysis and pole figures it is referred to the textbooks by Bunge [80, 81, 82].

Finally, one remark, all samples investigated are polycrystalline and more or less textured. In the following, the term *polycrystalline* means no amorphous nor single crystalline growth and that the grains are nearly perfect randomly oriented. *Textured* samples are meant to be also polycrystalline, but with (110) texture. Consequently, the decrease of the FWHM of (220) peak in rocking curves together with an increased intensity in 2θ -scans can serve as qualitative measure of the degree of texture.

3.3.2 Auger spectroscopy

To identify and quantify compositional changes in the surface region, Auger electron spectroscopy (AES) provides a suitable technique. The excitation of the Auger electrons reveals information from the depth of a few Angstrom (50 \AA [65]). In combination with ion beam etching, quantitative depth profiling is possible. Nevertheless, different etching yields for different elements complicate the detection of the Auger electrons. An element with lower etching yield stays longer on the sample surface than one with a higher yield. Consequently,

a dynamic equilibrium state is reached that is different from the real atomic composition in the sample. Hence, the quantitative analysis of the sample's stoichiometry in a depth profile has cautiously to be considered.

Additionally, a principle error of Auger spectroscopy has to be taken into account. The attenuation length of Auger electrons is element-specific [65]. Thus, the signal of two different elements, present in a thin film of equal atomic concentration, causes different concentrations. For example, a silicon film under an aluminum cap layer results in a higher signal than a comparable cobalt layer due to their different effective attenuation lengths ($\lambda_{Si2}^{eff} 2.41 \text{ nm} > \lambda_{Co1}^{eff} = 1.28 \text{ nm}$) [83].

Consequently, quantification of compositional changes requires to work with references of known stoichiometry.

3.3.3 XAS/XMCD

Element-specific magnetic information of the barrier to Heusler interface can be obtained using X-ray Absorption spectroscopy (XAS) and X-ray Magnetic Circular Dichroism (XMCD). The interaction of circular polarized x-rays with magnetic atoms originates the dichroism signal [74]. Not the direct dichroism signal, available in transmission, is detected, but that of secondary processes induced by the interaction in reflection are investigated. To ensure parallel alignment of the local magnetic moments, the measurements are taken in the saturated state of the film. They cause the XAS signal, which displays information about the electronic structure of the magnetic atoms or ions [83]. The signal difference of two measurements with parallel and antiparallel magnetic fields provides the XMCD signal, which is proportional to the magnetic moment at elevated energies corresponding to the absorption edges of the elements. The calculation of the resulting absolute magnetic moment then is a challenging task. Under certain assumptions and theoretical models the element-specific magnetic moment can be estimated [83]. Therefore, quantitative results have cautiously to be considered.

3.4 Determination of spin polarization

The determination of spin polarization is a challenging task. Especially in thin films the difference between spin up and down charge carriers is hard to determine. This paragraph will give an overview of commonly applied techniques in modern experimental physics. Although all these techniques provide information about the spin polarization, comparisons of the extracted values have cautiously to be evaluated [75]. Five experimental methods are proposed and illustrated. The determination by magnetic tunnel junctions used within this thesis will be the starting point. Afterwards a short review will be given on other alternative techniques. These are spin resolved photoemission, point contact tunneling into a ferromagnet, point-contact Andreev reflection (PCAR) and tunneling into a superconducting film after Tedrow and Meservey [84].

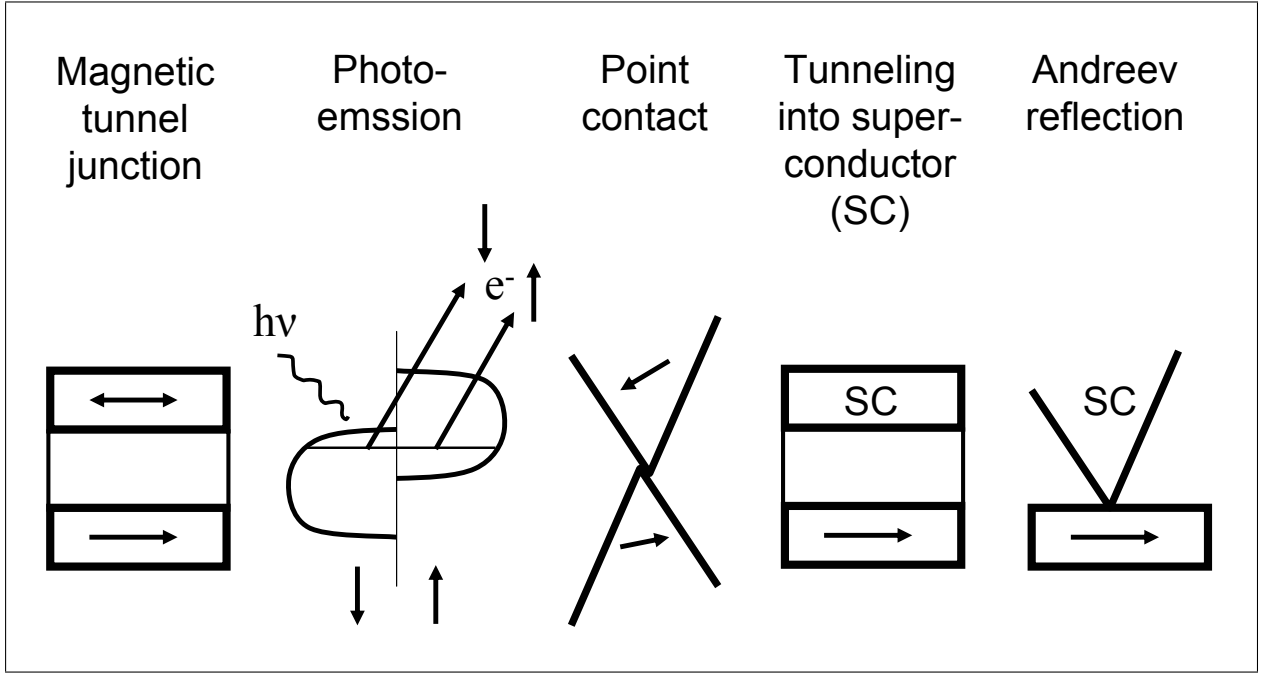


Figure 3.1: The most favored experimental techniques for determination of spin polarization; the arrows denote the orientation of magnetization (films) and the electron spin (band structure)

3.4.1 Magnetic tunnel junctions

In the thesis spin polarization determined by magnetic tunnel junctions (MTJs) is the preferred technique. It enables the tunneling of electrons through insulating barriers from one ferromagnetic film into another and serves as a spin polarization detection method. The resulting magnetoresistance is a measure of the spin polarizations of the ferromagnetic electrodes. The connection between magnetoresistance and underlying spin polarization was derived by Julliere [8] and resulted in a simple formula for the Tunnel Magnetoresistance (TMR):

$$TMR = \frac{2P_1P_2}{1 - P_1P_2}, \quad (3.3)$$

where P_1 and P_2 denote the spin polarization of the two electrodes at the Fermi level, respectively. Although this formula looks very simple, it displays the main feature, the dependence of the TMR amplitude on the spin polarization of the magnetic electrodes, of a real MTJ.

3.4.2 Alternative techniques

Alternatively to the determination by magnetic tunnel junction, few techniques are applied in present experimental investigations [39]. These four extra methods will be introduced briefly and discussed in respect to their pros and cons in background of MTJs. The reader should always hold in mind, that high spin polarized materials are, despite the fundamental aspect, very interesting for applications in magnetoresistive sensors and devices.

However, before these aspects will be discussed, some general features of spin polarization and its determination have to be considered. When determining the spin polarization, the special aspects of the applied technique have to be taken into account. In magnetic tunnel junctions as well as in tunneling into a superconducting film (also through an insulating barrier) the tunneling electrons are distributed near a few μeV at the Fermi level [75] and emit out of the first monolayers [76, 77, 75].

As indicated in [75], the interface or surface of the magnetic sample plays a dominant role for the transmission probability due to the sensitiveness of tunneling processes to the first monolayers. Therefore, tunneling through an insulating barrier (e.g. MTJ, tunneling into superconducting (SC) film) and tunneling or emission through a vacuum barrier (e.g. point-contact Andreev reflection, point-contact tunneling into a ferromagnet and photo emission) are hard to compare [75, 76], since their interface/surface structure is quite different. Common to all these techniques is, that the tunneling electrons originate from around the Fermi level [75]. In photo emission experiments, the complete band structure can be probed up to the Fermi level by variation of the wavelength of the photons [85, 86]. Hence, in principle, all these techniques can determine the spin polarization near the Fermi level. However, spin polarizations, derived from different techniques, have to be compared cautiously [87, 75].

Spin-resolved photo emission

The excitation by electromagnetic waves is one other way to determine the spin polarization. The analysis of emitted polarized electrons directly reveals the present spin asymmetry of the first few monolayers of the material studied [86, 88]. This technique enables to determine the spin-resolved band structure as well as the Fermi surface [85, 86]. For the interested reader it is referred to the book of Kevan [89].

Point-contact tunneling

Alternatively to tunneling through an insulating barrier in magnetic tunnel junctions, point contact tunneling through a vacuum barrier is a technique to provide information about the spin polarization of magnetic materials. The tunneling current between a ferromagnetic tip and film or between two ferromagnetic tips shows a dependence from relative orientation as in MTJs [90]. Antiparallel alignment of the two magnetizations

reveals a low current, where the parallel state shows a high tunnel current. Analogously to the MTJ technique, the spin polarization is determined by the use of Julliere's formula (3.3) for magnetoresistance amplitude [87]. The typical nanocontact area is ~ 1 nm [85]. The challenging task is to control the relative orientation in the tips [39], where a possible assembly is given in [90]. Advantageous is the possibility for temperature dependent spin polarization characterization [87].

Point-contact Andreev reflection (PCAR)

When tunneling into a superconducting tip, the possibility of temperature dependent studies vanishes. However, no special magnetic alignment is necessary. The point-contact Andreev reflection uses the fact that, if an electron is tunneling into the superconducting state, it needs a partner to form the Cooper pair [91]. This is only possible, if a hole with opposite spin is reflected at the interface. Consequently, if the two spin channels are occupied equally (non-magnetic), a high tunnel current is present in the energy range of the superconducting gap. Each tunneling electron can find a partner in the counterelectrode to form a Cooper pair. If no electron is available to form a Cooper pair, the tunnel current is vanishing. This is the case, if the ferromagnetic material exhibits a spin polarization of 100 %. No partner of opposite spin orientation can be found. To extract the spin polarization, the measured conductance-voltage characteristic has to be fitted by a procedure described in [91]. By this technique the transition metals [92] were characterized as well as the half Heusler alloy NiMnSb (58 % [91]), the present full Heusler Co₂MnSi (50-60 % [63]) and CrO₂ (90 % [91]).

Tunneling into a superconducting film

The method of Tedrow and Meservey uses the thin film technology as in magnetic tunnel junctions. The tunneling takes place between the investigated ferromagnetic film and a superconducting one. As superconducting electrode aluminum is preferred due to its high critical fields in thin films and its low atomic ordering number to avoid significant spin scattering via spin-orbit interaction [84]. Hence AlO_x is the inevitable choice of material for the insulating barrier. The formation of AlO_x is well understood and the Al/AlO_x interface would be of very high quality. The drawback of aluminum is the low superconducting critical temperature even in thin films ($T_c=2.5$ K [84]), which requires higher experimental efforts.

The quasi particles in the superconductor are Zeeman spin-split by an applied magnetic field [84] (smaller than the critical one), but high enough to saturate the ferromagnetic film. Due to the spin sensitive density of states in the ferromagnet the probability for tunneling is different. Consequently, the resulting I - V -characteristic reveal four separated tunneling peaks displaying the convolution of the density of states in the superconductor and in the

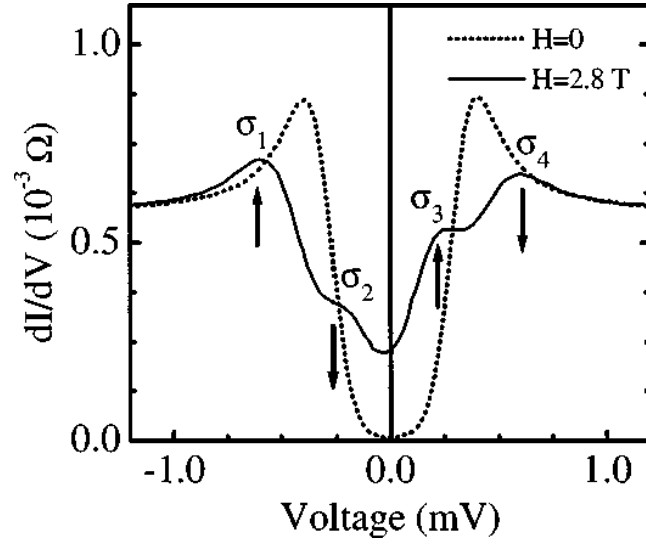


Figure 3.2: Typical measurement of spin polarization determination at NiMnSb/Al₂O₃/Al tunnel junction by the technique of Tedrow and Meservey from [36]; the conductance peaks σ_i are due to the Zeeman splitting of quasi-particles

ferromagnet. The spin polarization P can be estimated to be [84]:

$$P \sim \frac{(\sigma_4 - \sigma_2) - (\sigma_1 - \sigma_3)}{(\sigma_4 - \sigma_2) + (\sigma_1 - \sigma_3)} \quad (3.4)$$

where σ_i denote the conductances in sequence of increasing voltage (see Fig. 3.2). For the accurate determination of P spin-orbit scattering has to be accounted [75, 84]

Chapter 4

Thin films of Co_2MnSi

The deposition and integration of Co_2MnSi thin films in existing magnetic tunnel junctions is a challenging task. But before describing the realization of a MTJ containing Co_2MnSi , the behavior of single Co_2MnSi thin films will be discussed dealing with magnetic, electrical and microstructural properties under various growth conditions.

4.1 Polycrystalline films

Polycrystalline samples can be prepared by two techniques: dc magnetron sputtering of Co_2MnSi on various heated substrates or room temperature deposition on SiO_2 and subsequent post annealing.

Both techniques will be studied on 100 nm thick Co_2MnSi films to be able to apply XRD characterization. For the first technique, the substrate temperature is varied from room temperature up to 600 °C. As has been demonstrated in the initial investigations in paragraph 2, at a substrate temperature of 450 °C, polycrystalline growth is reached independently of substrate material. Therefore, $\text{SiO}_2(5 \text{ nm})//\text{V}(42 \text{ nm})$ has been chosen as substrate to simultaneously study the influence of the vanadium seed layer at substrate temperatures different from room temperature.

For the post annealing procedure $\text{SiO}_2(100 \text{ nm})$ has been taken to achieve polycrystalline growth at elevated annealing temperatures. These have been chosen to be in the range of 400-550 °C and have been applied in the external vacuum furnace. At lower temperatures the growth is still amorphous and the resulting magnetization tends to zero.

4.1.1 Electrical behavior

The electrical resistance is affected by local disorder. Hence, the resistivity is a good parameter for indirectly characterizing the order-disorder relations. Matthiessen's rule

defines the resistivity of any metal or alloy as [43]:

$$\rho(T) = \rho_0 + \rho_{p,m}(T) \quad , \quad (4.1)$$

where the resistivity is composed of the temperature dependent part $\rho(T)$ characterized by electron-phonon and electron-magnon scattering and the temperature independent part ρ_0 , which describes the electron scattering on crystal lattice imperfections. For further discussion the magnon induced part of $\rho(T)$ of single Co₂MnSi films can be neglected due to their high Curie temperature of 985 K [9]. The temperature independent part ρ_0 can be extracted by cooling down the sample to 10 K. Measuring the resistivity at 10 K provides only the influence of crystal defects, while magnon and phonon excitations are frozen out. Consequently, the effect of local disorder in Heusler alloys can be evaluated.

However, a general discussion of electrical resistivity includes an order dependent temperature part $\rho_p(S, T)$. By use of an order parameter S , as defined before in paragraph 1.2, Mathiessen's rule can be rewritten under assumption of band structure effects to [93]:

$$\rho(S, T) = \rho_0(S) + \rho_p(S, T) = \rho_0(S = 0) \left(\frac{1 - S^2}{1 - AS^2} \right) + \frac{TB}{n_0(1 - AS^2)} \quad , \quad (4.2)$$

where n_0 is the material dependent density of electrons in the disordered state and A and B are material constants. A depends upon the relative position to the Fermi surface and the Brillouin zone boundaries, where B mainly determines the temperature dependence. This equation (4.2) reveals the main influences of disorder on the electrical resistivity. A highly ordered alloy characterized by $S \sim 1$ exhibits a minimum impurity part $\rho_0 \propto 1 - S^2$ [93] and a maximum ratio between high and low temperature resistivity $(1 + C \frac{T}{1 - S^2})$, where C summarizes the material dependent coefficients. Thus, the room temperature resistivity can serve as a first rough measure of disorder. A sample in the highly ordered state exhibits a lower resistivity than the one in the disordered state.

Regarding the room temperature resistivities of SiO₂(5 nm)//V(42 nm)/Co₂MnSi(100 nm) in dependence of substrate temperature in Fig. 4.1 a), the resistivities range between 200 $\mu\Omega\text{cm}$ and 220 $\mu\Omega\text{cm}$ up to substrate temperatures of 200 °C. Thereafter, they decrease down to a minimum of 110 $\mu\Omega\text{cm}$ at $T_{\text{sub}} = 450$ °C, before they slightly increase to 120 $\mu\Omega\text{cm}$ at $T_{\text{sub}} = 600$ °C. This minimum resistivity of 110 $\mu\Omega\text{cm}$ is in agreement with values for samples on a V buffer in literature [5].

To separate the influence of the vanadium during low temperature measurement and because of the unimportance of the substrate material at a substrate temperature of unit[450]°C, the 100 nm Co₂MnSi film has been directly prepared onto SiO₂(5 nm). Then for this sample the temperature dependence of resistivity has been taken given in Fig. 4.1 b). Apart from a slightly increased resistivity at room temperature of 170 $\mu\Omega\text{cm}$, a ratio between room and low temperature resistivity of 1.3 is achieved. This value is in agreement with temperature dependent resistivity investigations on thin Co₂MnSi films by other groups [7, 5]. However, a polycrystalline bulk sample exhibits a ratio of 6.5 [7] indicating a lower degree of order in the prepared samples.

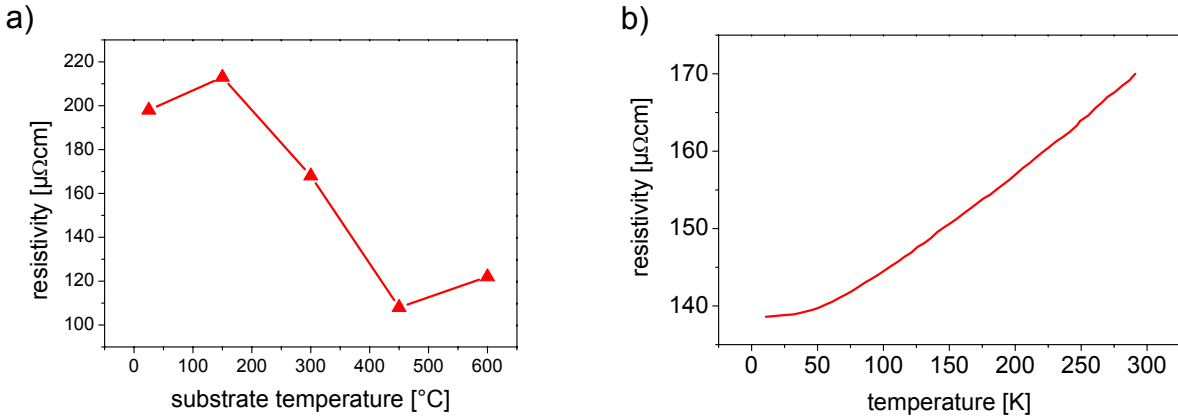


Figure 4.1: a) Resistivity at room temperature vs. substrate temperature for polycrystalline samples deposited on $\text{SiO}_2(5\text{ nm})//\text{V}(42\text{ nm})$; b) temperature dependence of resistivity of polycrystalline sample prepared at $T_{\text{sub}} = 450\text{ }^{\circ}\text{C}$ on $\text{SiO}_2(5\text{ nm})$

4.1.2 Magnetic evolution

A more directly accessible parameter for observing local ordering is the magnetic behavior. By measuring a complete hysteresis loop, one has the opportunity to extract information about local ordering from saturation magnetization.

The most intuitive magnetic parameter connected to local disorder is the saturation magnetization. The interatomic distance and the detailed atomic environment determine the type of magnetic coupling. This behavior can be illustrated very demonstratively on manganese atoms in different atomic environments and different interatomic distances. In pure metallic arrangement, manganese is antiferromagnetic at low temperatures with a next neighbor distance of about 8.9 \AA [15], but antiferromagnetic at low temperatures ($T_N = 100\text{ K}$ [15]). If the distance is artificially decreased as in the Co_2MnSi Heusler alloy or in Cu_2MnAl (4.0 \AA), the manganese atoms couples ferromagnetically. By decreasing the distance (MnO : 3.1 \AA or MnF_2 : 3.8 \AA) the magnetic interaction changes to antiferromagnetic one at low temperature. However, in the latter cases the magnetic interaction is mediated the F or O ions [24], called super exchange, as has been described in paragraph 1.1.2.

Although the magnetic coupling mechanism is different in each of the three mentioned cases, it is obvious that small deviations from optimal configuration will sensitively disturb the magnetic ordering. Small variations of the interatomic distance may weaken the exchange interaction and by that the magnetic saturation magnetization.

The evolution of the saturation magnetization as a function of the annealing temperature is given in Fig. 4.2 a). It is seen that higher annealing temperatures can stimulate atomic ordering and, hence, result in an increase of the saturation magnetization. At moderately low substrate temperatures ($T_{\text{sub}} = \text{RT} - 200\text{ }^{\circ}\text{C}$) nearly no magnetization can be detected. But when reaching temperatures of $300\text{ }^{\circ}\text{C}$ to $600\text{ }^{\circ}\text{C}$, the theoretically predicted value

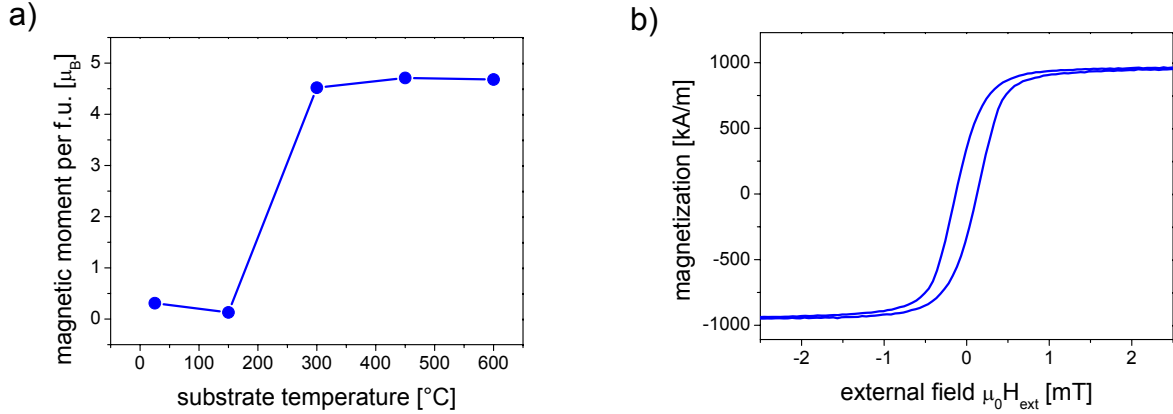


Figure 4.2: a) Magnetic moment per formula unit (f.u.) vs. substrate temperature for the heated substrate samples; b) hysteresis loop for $\text{SiO}_2(5 \text{ nm})//\text{V}(42 \text{ nm})//\text{Co}_2\text{MnSi}(100 \text{ nm})$ prepared at $T_{\text{sub}}=450 \text{ }^{\circ}\text{C}$

of the saturation magnetization is reached, as indicated in Tab. 2.1. The maximum of saturation magnetization is revealed for the sample prepared at $450 \text{ }^{\circ}\text{C}$ in agreement with lowest resistivity for this sample. In comparison the coercive field also shows a substrate temperature dependent behavior. A small coercivity of 0.2 mT belongs to the optimal magnetization value. A typical hysteresis loop is presented in Fig. 4.2 b).

Alternatively, Co_2MnSi films were firstly deposited onto SiO_2 substrate at room temperature and then subsequently annealed for 70 minutes at elevated temperatures in the external vacuum furnace. Fig. 4.3 a) summarizes the saturation magnetization vs. temperature behavior. The temperature range can be divided into three zones. The first zone up to $450 \text{ }^{\circ}\text{C}$ is characterized by not sufficient annealing temperatures, resulting in an incomplete ordering and a corresponding increase of saturation magnetization with increasing temperature. The range from $450 \text{ }^{\circ}\text{C}$ to $525 \text{ }^{\circ}\text{C}$ identifies the range where large saturation magnetization can be achieved with a maximum at $500 \text{ }^{\circ}\text{C}$. The decrease of saturation magnetization above $500 \text{ }^{\circ}\text{C}$ can be attributed to the diffusion of Co into the silicon substrate through the $\text{SiO}_2(100 \text{ nm})$. This interdiffusion has been found by XRR measurements revealing the destruction of the typical layer structure. In addition, the appearance of additional peaks corresponding to CoSi has been proven by x-ray diffraction.

Correspondingly, samples with lowest coercivities of values from 1 to 2 mT are found in the optimal temperature range, as can be seen in Fig. 4.3 b). These coercivities are in agreement with polycrystalline samples in literature [7]. In comparison, the polycrystalline samples prepared on heated substrate reveal lower coercivities $\sim 0.2 \text{ mT}$. This can be induced by the magnetic field of sputter source present during the complete deposition and cooling process.

Investigating the hysteresis loop in detail, a nearly rectangular switching behavior is

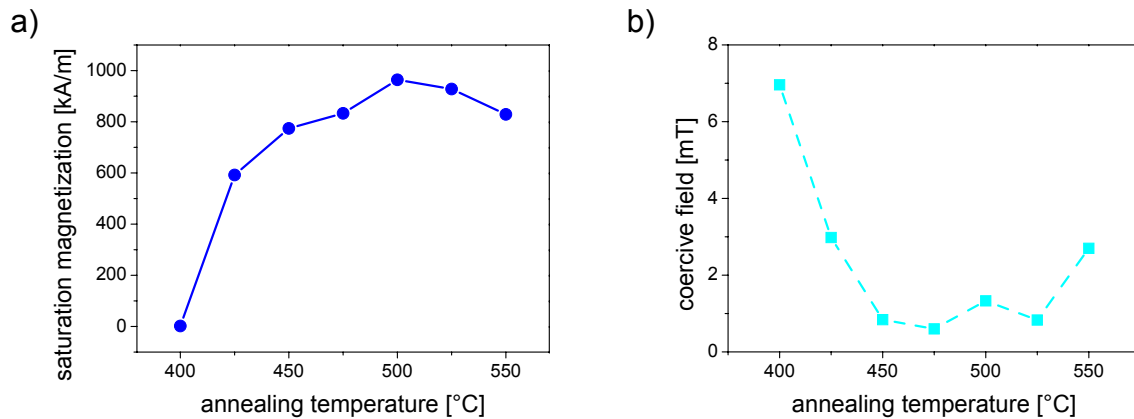


Figure 4.3: a) Magnetic behavior of polycrystalline samples $\text{SiO}_2(100\text{ nm})//\text{Co}_2\text{MnSi}(100\text{ nm})$ prepared by post annealing procedure in the external vacuum furnace: a) saturation magnetization and b) coercive field in dependence from annealing temperature

observed for the post annealed samples. The exact knowledge of the hysteresis enables one to determine the anisotropy constant of Co_2MnSi by an enhanced Stoner-Wohlfarth model [94]. By energy minimization a cubic anisotropy constant of 1.50 kJ/m^3 results. Also taken into account is a uniform distributed grain orientation in the in-plane direction, which has been confirmed by an isotropic magnetic behavior in MOKE.

In summary, it has been shown that a temperature can be found for both preparation techniques. The optimal temperature has been determined to be 450°C for the heated substrate samples and 500°C for the post annealed ones. For the heated substrate samples the maximum saturation magnetization coincides with the lowest resistivity.

In conclusion, it has been shown that lowest electrical resistivities coincides with maximum saturation magnetizations and low coercivities [7].

4.1.3 Analysis of microstructure

At the present stage, Co_2MnSi Heusler alloys thin films have been characterized in terms of substrate and annealing temperature with the focus on the magnetic and electrical behavior. Now the underlying microstructural evolution will be discussed in detail starting again with the series of heated substrates and subsequently the samples treated via the post annealing procedure.

Samples prepared at room temperature only show a very wide (220) peak at about $2\theta \sim 45^\circ$, as indicated by the red dotted curve in Fig. 2.3 b). The FWHM of this peak corresponds to 5° and is related to a grain size in normal direction of about 2-3 nm. The appearance of this most intense fundamental (220) peak together with this small grain

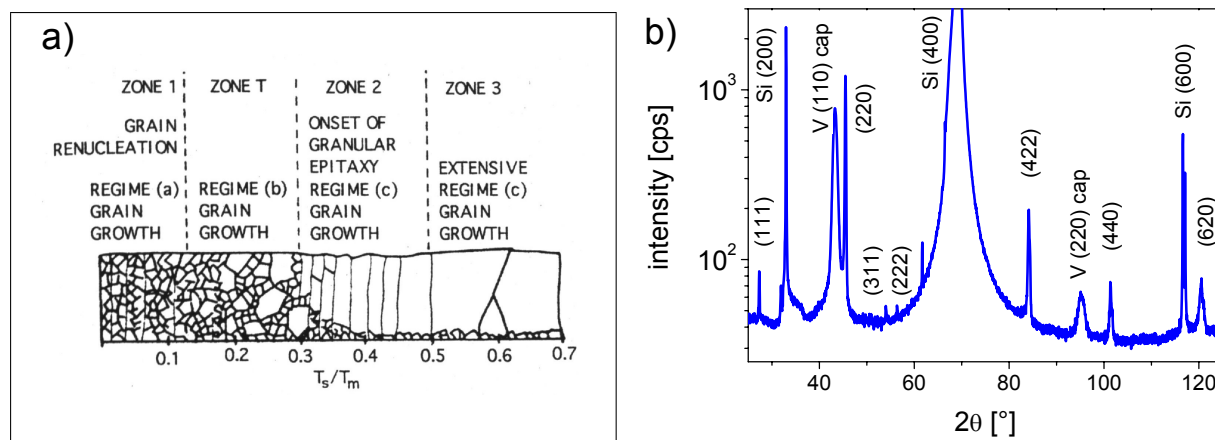


Figure 4.4: a) Growth scheme after [95] introducing four zones for substrate temperature dependent growth (the abscissae is denoted by the ratio of substrate temperature T_s (T_{sub}) and melting point T_m); b) XRD pattern of polycrystalline sample prepared by post annealing at 500 °C for 70 minutes in the external vacuum furnace

size indicates amorphous growth, which is accompanied by an almost vanishing saturation magnetization of $0.25 \mu_B$ per formula unit. Upon annealing the substrate up to 600 °C the microstructural evolution can be studied as a function of substrate temperature.

Up to 200 °C the amorphous growth is persistent. Thereafter, between 300 °C and 600 °C, polycrystalline growth is present and is consistent with the initial experiments concerning the substrate material, as has been described in paragraph 2.3, and with investigations on thermally evaporated thin films [7].

The grain growth with increasing substrate temperature can be explained using growth scheme [95], which is given in Fig. 4.4 a). The transition from amorphous to microcrystalline grain structures is characterized by zone 1 at low temperatures. Zones 2 and 3 correspond to polycrystalline grain growth at substrate temperatures from 300 °C up to 600 °C.

In conclusion, polycrystalline growth is visible at 300 °C. These findings can be correlated to the electrical and magnetic behavior, as has been previously discussed. The polycrystalline structure detected by x-ray patterns indicate good ordering at the elevated temperatures. Analyzing the peak intensities of a sample prepared at 450 °C, best matching with calculated reference data (compare Tab. A.3) is achieved. A lowest resistivity and a maximum saturation magnetization for this sample confirm the high degree of order. The grain size has been estimated to be 50-60 nm.

Samples prepared at room temperature and subsequently annealed show a similar microstructural evolution. A typical x-ray pattern is given in figure 4.4 b) indicating the nearly perfect polycrystalline microstructure.

In conclusion, it has been demonstrated that polycrystalline Co_2MnSi thin films can be

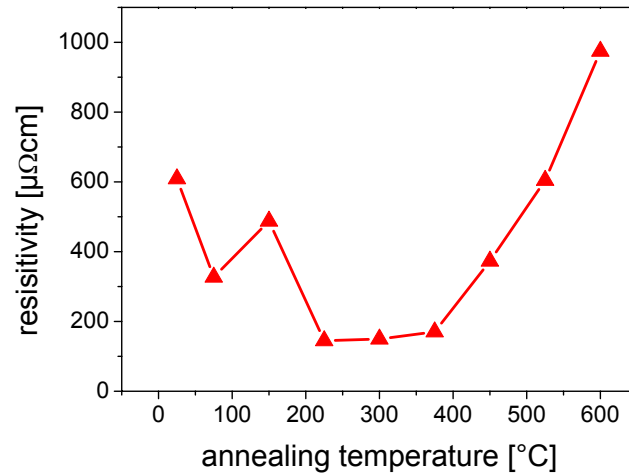


Figure 4.5: Resistivity vs. annealing temperature for (110) textured samples ($\text{SiO}_2(5\text{ nm})//\text{V}(42\text{ nm})/\text{Co}_2\text{MnSi}(100\text{ nm})$)

prepared by DC magnetron sputtering following two alternative preparation routes, which result in polycrystalline films of good quality. The electrical, magnetic and microstructural properties are strongly correlated.

4.2 Textured films

Alternatively to polycrystalline samples, it is possible to prepare textured films of Co_2MnSi Heusler alloy. This can be achieved by depositing the Co_2MnSi films onto a V seed layer followed by subsequent annealing. This annealing procedure was done in-situ in the same sputtering apparatus. As a result Co_2MnSi films can be prepared with pronounced (110) grain texture.

4.2.1 Electrical behavior

Regarding the electrical behavior of (110) textured samples, a minimum resistivity can be obtained, as is illustrated in Fig. 4.5. Starting at room temperature without a post annealing procedure, a resistivity of about $600\ \mu\Omega\text{ cm}$ is measured. This is decreased down to $170\ \mu\Omega\text{ cm}$, when annealing between 200 and 400 °C. This temperature range is characterized by minimum resistivity. By increasing the annealing temperature above 400 °C, the resistivity increases. The high temperature enables interdiffusion into the substrate, as has been proven by the destruction of the layered structure accessible by XRR experiments.

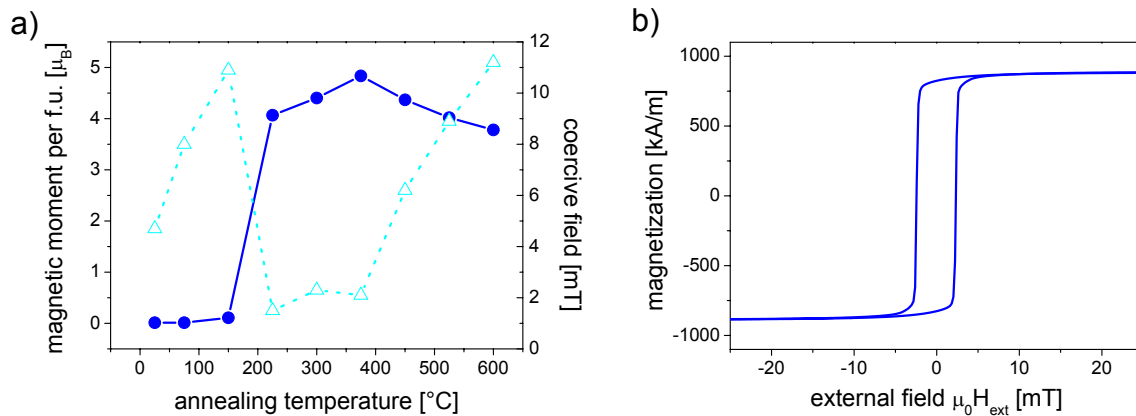


Figure 4.6: a) Saturation magnetization and coercive field vs. annealing temperature; b) hysteresis loop for (110) textured sample ($\text{SiO}_2(5 \text{ nm})//\text{V}(42 \text{ nm})/\text{Co}_2\text{MnSi}(100 \text{ nm})$) prepared by post annealing at 300 $^{\circ}\text{C}$ by the in-situ technique in system II

4.2.2 Magnetic evolution

As has already been measured for the polycrystalline samples, the textured samples show a strong correlation between the resistivity and saturation magnetization in dependence of the annealing temperature. The annealing temperature has been varied between room temperature and 600 $^{\circ}\text{C}$ and the resulting dependence is given in Fig. 4.6 a). Up to 150 $^{\circ}\text{C}$ the saturation magnetization or magnetic moment per formula unit stays unchanged around zero. Between 150 $^{\circ}\text{C}$ and 225 $^{\circ}\text{C}$ the magnetization increases above $4 \mu_B$ per f.u. Then up to 375 $^{\circ}\text{C}$ the saturation magnetization increases to about $4.9 \mu_B$ per f.u., before it decreases under $4 \mu_B$ per f.u. at an annealing temperature of 600 $^{\circ}\text{C}$. The present maximum of $4.9 \mu_B$ per f.u. is in good agreement with (110) textured films of another group [5]. The evolution of the coercive field with annealing temperature can similarly be characterized. Up to 225 $^{\circ}\text{C}$ the coercivities increase from 5 mT up to 11 mT, before they drop down to under 2 mT at 225 $^{\circ}\text{C}$. Up to 375 $^{\circ}\text{C}$ the coercive fields stay nearly unchanged at around 2 mT. Above 375 $^{\circ}\text{C}$ annealing temperature the coercivities drastically increase up to above 11 mT at 600 $^{\circ}\text{C}$. The described behavior of magnetization with annealing temperature is in agreement with annealing temperature dependence of resistivity investigated before. The annealing temperature range between 200 $^{\circ}\text{C}$ and 400 $^{\circ}\text{C}$ ¹ exhibits lowest resistivities on the one hand, and highest saturation magnetization and lowest coercivities on the other hand. Within this optimal annealing temperature range the hysteresis loops are nearly rectangular, as can be seen for an annealing temperature of 300 $^{\circ}\text{C}$ in Fig. 4.6 b).

When applying again the enhanced Stoner-Wohlfarth model by energy minimization to

¹A comparison of the annealing temperatures of the polycrystalline and (110) textured sample is difficult. The polycrystalline samples have been annealed ex-situ, where the textured ones have been deposited onto a 42 nm vanadium seed layer and annealed in-situ in sputter system II.

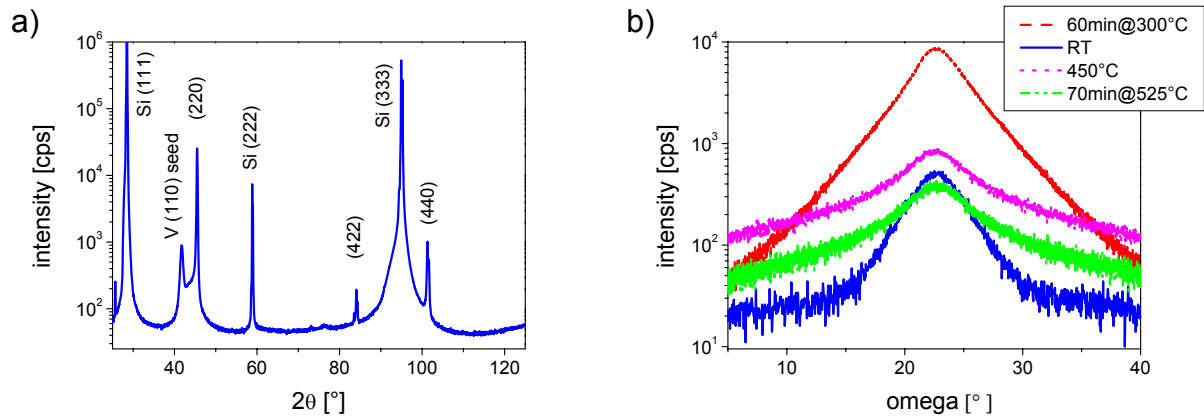


Figure 4.7: a) XRD pattern of (110) textured sample prepared by the post annealing procedure at 300 °C by the in-situ technique in system II; apart from the Co_2MnSi alloy peaks the Si and vanadium peaks are present; b) influence of V buffer: rocking curves of samples prepared by post annealing procedure (red (V-buffer: (110) texture) and green (on SiO_2 : polycrystalline)), without any annealing but V-buffer (blue) and on heated substrate (purple) showing the different degree of texture

this hysteresis shape, as is described in [94], an anisotropy constant of 2.89 kJ/m^3 can be derived. Within this model a randomly oriented grain distribution is assumed, which is justified by an isotropic magnetic behavior confirmed by MOKE also for the textured samples.

4.2.3 Analysis of microstructure

Till now it has been demonstrated that electrical resistivity and saturation magnetization are strongly related. For polycrystalline as well as for (110) textured samples, a high magnetization value and a low resistivity value coincide for suited substrate or annealing temperatures. This electrical and magnetic evolution has been confirmed by XRD experiments for the microstructure of the polycrystalline samples. The microstructure of the (110) textured samples show a similar annealing temperature behavior as of the post annealed polycrystalline ones.

At room temperature preparation the V seed layer establish a (110) texture, as has been demonstrated in paragraph 2.3. However, (110) textured growth with full magnetization is only present for annealing temperatures higher than 200 °C. In a typical x-ray pattern given in Fig. 4.7 a) (220) and (440) peaks are present with high intensities indicating the (110) texture. Additionally, the (422) is apparent but very low in intensity with respect to the (220) and (440).

Further evidence for (110) texture can be established by the technique of rocking curves. By tilting the sample around the optical axes in XRD experiments, the degree of texture

| | V buffer | FWHM [$^\circ$] | peak height [cps] |
|---------------------|-------------|----------------------|----------------------|
| post annealing | + | 4.8 | 8500 |
| room temperature | + | 4.7 | 500 |
| heated substrate | - | 6.8 | 820 |
| post annealing | - | 6.9 | 337 |

Table 4.1: Full width at half maximum (FWHM) and measured peak intensities in counts per second (cps) corresponding to Fig. 4.7 b)

can be qualitatively determined. High degree of texture is characterized by a small FWHM and a high intensity in rocking curves². The comparison of the polycrystalline and textured samples within this techniques directly reveals the more (110) texture in latter samples. The polycrystalline samples prepared either by the heated substrate or the post annealing method reveal a full width at half maximum of about 7° (see magenta and green curve in Fig. 4.7 b) and corresponding parameters in Tab. 4.1). By introducing the vanadium seed layer the FWHM is decreased to 5° at room temperature (blue). By application of the post annealing procedure the FWHM still is 5° (red), but the intensity is drastically raised confirming the transformation of the amorphous volume to a high ordered textured one (see also table 4.1).

Till now the investigations show that it is possible to prepare polycrystalline and textured Co_2MnSi samples with low resistivity and high saturation magnetization. However, no direct method for local disorder investigations has been employed. Only indirect measurements such as electrical resistivity and saturation magnetization have been performed to judge on the order-disorder relation.

4.3 Conclusion - ordering and intrinsic parameters

So far the ongoing discussion was dedicated to the electrical, magnetic and microstructural behavior on a more phenomenological approach. Furthermore, there was no direct access to an order parameter. Now it will be concentrated on the determination of local disorder and a corresponding order parameter enabling the connection to electrical and magnetic parameters.

²For comparison a silicon powder sample and a (111) single crystalline substrate have been characterized in the same way. The powder sample reveals a FWHM of 2.8° and an intensity of 7400 cps, where the single crystalline sample exhibits 0.9° and 2×10^6 cps as FWHM and intensity.

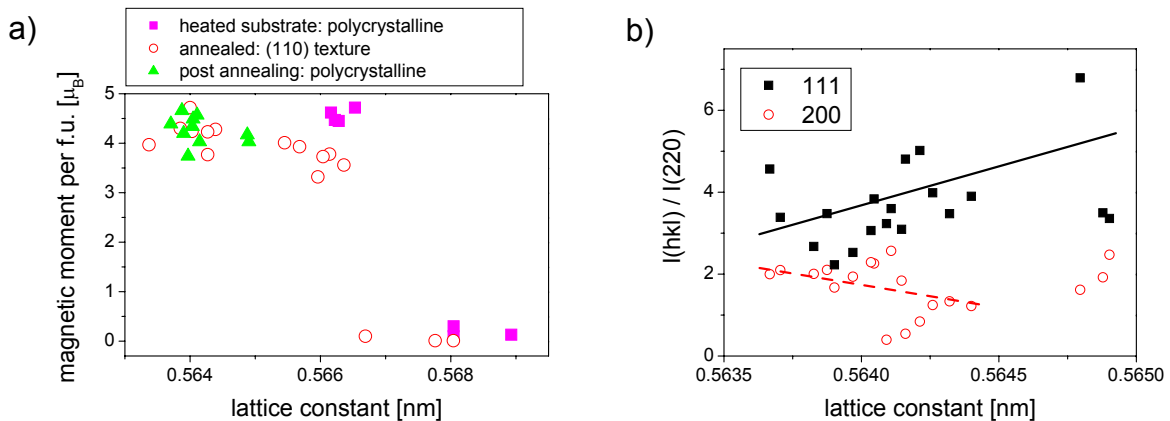


Figure 4.8: a) Comparison of polycrystalline and (110) textured samples by plotting saturation magnetization against lattice constant; b) ordering on microscale: films with minimum lattice constant characterize state of highest local ordering (relative intensities were determined by polycrystalline samples prepared by the post annealing procedure without vanadium seed layer)

Firstly, the lattice constants will be analyzed. This parameter is extracted from the x-ray diffractions measurements by determination of the exact 2θ -position of the (220) peak³ and by subsequently using the Bragg equation (1.2). Magnetic behavior and lattice constant are strongly correlated due to the sensitivity of the ferromagnetic interaction on the interatomic distance, as has been explained in paragraph 1.1.2. This can be seen when the saturation magnetization of various samples of different preparation procedures is plotted against the corresponding lattice constant Fig. 4.8 a). Larger lattice constants match with poor magnetization. When the lattice constant is smaller than the threshold of 0.5666 nm, the sample shows an increase in saturation magnetization.

The previous discussion has revealed that the ordered state with highest saturation magnetization corresponds to smaller lattice constants. Thus, the lattice constant is an additional parameter to qualitatively measure the degree of order. However, the origin on atomic scale for these slight deviations of lattice constant between 0.563 nm and 0.566 nm and corresponding saturation magnetization is not obvious. For this purpose the corresponding evolution of relative superlattice peak intensities in XRD experiments can serve. The evolution of these intensities is strongly correlated to the degree of disorder, as has been introduced in paragraph 1.2.3. Since the experimentally determined intensities of a perfectly ordered sample are not accessible, the type and degree of disorder cannot be correlated to the evolution in Fig. 1.6. A reference parameter, which qualitatively determines the order-disorder relation, is needed. The electrical resistivity, the saturation magnetization or the lattice constant can serve as such a parameter. Here the lattice

³This peak is taken due to two reasons. Firstly, it is present in all XRD measurements and, secondly, exhibits the highest intensity.

| thickness [nm] | preparation | roughness [nm] |
|----------------|-----------------------------------|----------------|
| 2.6 | RT | 0.20 |
| 100 | RT | 0.25-0.36 |
| 260 | RT | 0.23-0.34 |
| 100 | 40 min at 450 °C | 0.4 |
| 26 | $T_{\text{sub}} = 450 \text{ °C}$ | 0.46-0.57 |

Table 4.2: Rms-roughness of different Co_2MnSi thin films prepared on a 42 nm vanadium seed layer at room temperature, by post annealing procedure and onto heated substrate; determined over an area of $500 \times 500 \text{ nm}^2$

constant is taken, for which the ordered state is characterized by smallest values. Now regarding the evolution of relative peak intensities $I(hkl)/I(220)$ with lattice constant the type of disorder can be derived. As shown in Fig. 4.8 b), the (111) peak intensity increases and the (200) peak intensity decreases with increasing lattice constant. Or in terms of disorder: with increasing disorder the (111) intensity is increasing, where the (200) one is decreasing. Comparing this evolution of both peak intensities with the calculated evolution as a function of disorder parameter α in Fig. 1.6, the main disorder process becomes clear. The present combination of (111) and (200) evolution is only possible for Co-Mn or Co-Mn-Co disorder ⁴. This Co-Mn disorder was also found in literature [12] and the affinity for this type of disorder was attributed to the similar atomic radii of Co and Mn (1.25 Å and 1.12 Å) and their similar electronic properties [7].

In conclusion, the electrical and magnetic behavior could be connected to the microstructure. Optimal Co_2MnSi alloy thin films require temperatures between 200 °C and 450 °C dependent on exact preparation procedure and conditions. These optimal samples exhibit lowest resistivities, highest saturation magnetization and smallest lattice constants. For small deviations of these quantities the Mn-Co disorder has been identified to be responsible.

4.4 Growth of Co_2MnSi films

So far it has been demonstrated that it is possible to deposit Co_2MnSi thin films onto silicon substrate and V seed layer at elevated substrate and annealing temperatures and that these films exhibit well defined electrical, magnetic and microstructural properties. Now it is time to investigate the influence of the film thickness and the local ordering during annealing. The thickness dependence will be discussed in terms of surface morphology using Scanning Electron Microscopy (SEM) and Atomic Force Microscopy (AFM) and bulk magnetism. Firstly, the surface morphology will be studied. Especially

⁴Since the two Co sublattices are indistinguishable for the Mn atoms, it will be spoken of Co-Mn disorder in general.

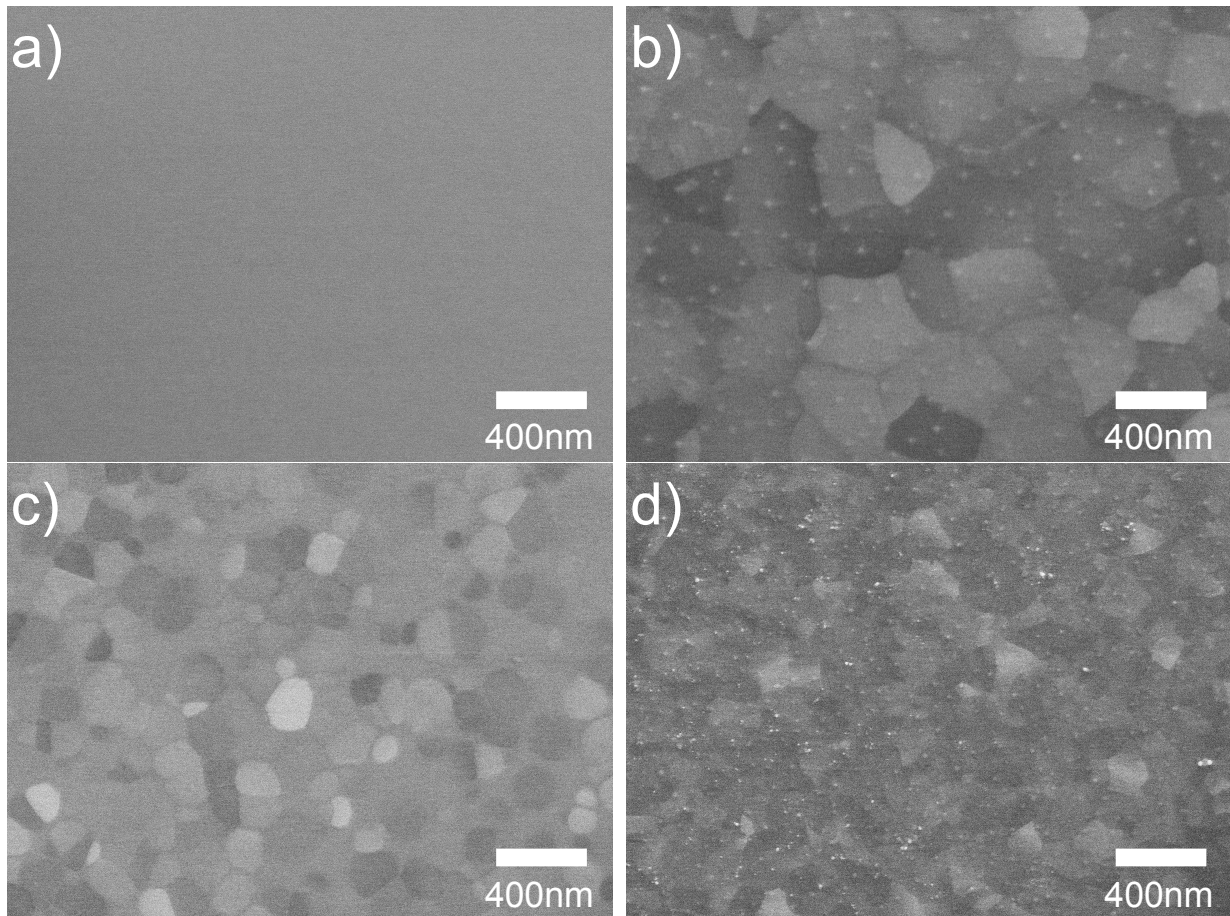


Figure 4.9: Morphology of Co_2MnSi thin films in dependence of layer thickness: 100 nm without post annealing a), 100 nm b), 61 nm c) and 15 nm d) with post annealing

for integrating Co_2MnSi thin films in magnetic tunnel junctions, the surface roughness has to be sufficiently small [10]. Only smooth surfaces enable the perfect deposition of the insulating aluminumoxide barrier.

Investigating the thickness dependence of bulk magnetism reveals information about the influence of the adjacent interfaces and make it possible to determine a minimum layer thickness.

As has been denoted in the previous paragraph, the Co-Mn disorder is responsible for slight deviations of saturation magnetization and lattice constant. However, this disorder type cannot account for the drastic change in saturation magnetization from 400 °C to 425 °C annealing temperature. The purpose of the final paragraph will be to clear up the origin for this drastic increase.

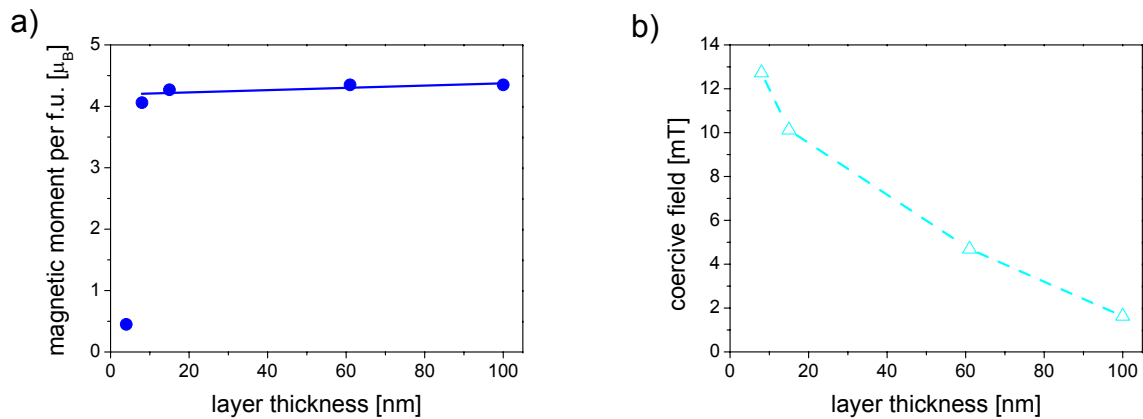


Figure 4.10: a) Magnetic moment per formula unit and b) coercivities in dependence of layer thickness for (110) textured samples prepared by the post annealing procedure with 42 nm V seed layer: down to 8nm layer thickness the magnetic moment is nearly constant

4.4.1 Surface morphology and roughness

To get a first idea of the growth mechanism in Co_2MnSi thin films, SEM images have been taken and are shown in Fig. 4.9 b)-d) of samples with film thickness varying from 15 nm to 100 nm deposited at room temperature onto a vanadium seed layer of identical thickness of 42 nm and subsequently annealed. For comparison, an image of a 100 nm sample prepared without the post annealing is also shown in Fig. 4.9 a). It is obvious that this sample provides no visible morphology indicating very small grains or an amorphous microstructure. This is in coincidence with the microstructure of polycrystalline and textured samples, already discussed in paragraphs 4.1.3 and 4.2.3. However, when the post annealing procedure is applied, the formation of very large grains of about 200-400 nm in lateral dimension do occur. Decreasing the film thickness over 61 nm down to 15 nm, the grain size decreases to 100-200 nm and 50-100 nm, respectively. This decrease in grain size with decreasing layer thickness is also observed for thin films in [95].

Although this drastic variation in grain size has been found, the corresponding surface roughness is surprisingly smooth. At room temperature prepared films are characterized by a surface roughness of rms-values of 0.2-0.4 nm only correspondingly to the structureless SEM image in Fig. 4.9 a). By the post annealing procedure the rms-roughness reaches a value of 0.4 nm, although large grains of 200-400 nm are present as indicated by the SEM image in Fig. 4.9 b). The deposition onto heated substrate reveals a higher rms-roughness of 0.4-0.6 nm. For comparison this data is summarized in Tab. 4.2.

4.4.2 Magnetism

As has been discussed before, the saturation magnetization is a very sensitive indicator of local ordering. Within that context the question arises whether the different grain sizes are influencing the magnetic behavior of the Co₂MnSi films. The corresponding plot, given in Fig. 4.10 a), reveals a nearly remaining constant magnetic moment down to a film thickness of 8 nm with a value close to that of the best optimized grown single Co₂MnSi layer. In contrast, a 4 nm thin film exhibits nearly no magnetic moment. Thus the transition from disorder to reasonably well ordered Co₂MnSi films is within the thickness range from 4 nm to 15 nm. However, the coercive field in Fig. 4.10 b) as the second magnetic parameter reveals a strong continuous thickness dependence. For thin films with an amorphous microstructure or small grains the coercivities decrease from 12.5 mT at 8 nm thin films to 2 mT at 100 nm film thickness. The evolution of the coercivity with increasing film thickness or resulting grain size can be compared with investigations on cobalt or iron powder samples, where the increase of the coercivity for decreasing particle size was attributed to approaching the single domain state of the particle [96, 97].

4.4.3 Local ordering

Till now it has been demonstrated that the slight deviations in saturation magnetization and lattice constant can be attributed to the presence of Co-Mn disorder. However, the origin for the drastic increase of saturation magnetization between an annealing temperature of 400 °C and 425 °C is still unclear for both the (110) textured and polycrystalline samples. In order to reveal the influence of local ordering effects, the evolution of the relative peak intensities of polycrystalline samples will be discussed as a function of annealing temperature. Such a discussion of peak intensities is only useful for perfect polycrystalline samples due to the presence of all superlattice peaks, as has been discussed in paragraph 1.2.2. The complete set of corresponding peak intensities is given in Fig. 4.11 a). For more transparency the intensities are divided into the classes of the fundamental and superlattice ones. The fundamental peaks (400), (422) and (440) are given in Fig. 4.11 b) ⁵. Over the total temperature range from 425 °C up to 550 °C the fundamental peak intensities are constant. The (400) peak intensity is more varying, since the signal to noise ratio is lower than for (422) and (440).

The superlattice peaks can be divided into two classes. The intensities of (111) and (311), given in Fig. 4.11 c), and (200) and (222), given in Fig. 4.11 d), make it possible to conclude on local ordering effects. They are sensitive to antisite disorder effects, as described in paragraph 1.2.2. The intensities of (111) and (311) increases with increasing annealing temperature, where (200) and (222) stay constant. However, no perfect ordered reference sample and the corresponding measured peak intensities are accessible. Without an ordering parameter as the electrical resistivity, the saturation magnetization or the lattice constant, no comment can be made on the type of disorder. Here the

⁵The (220) peak also belongs to the fundamental peaks, but is used as normalization factor.

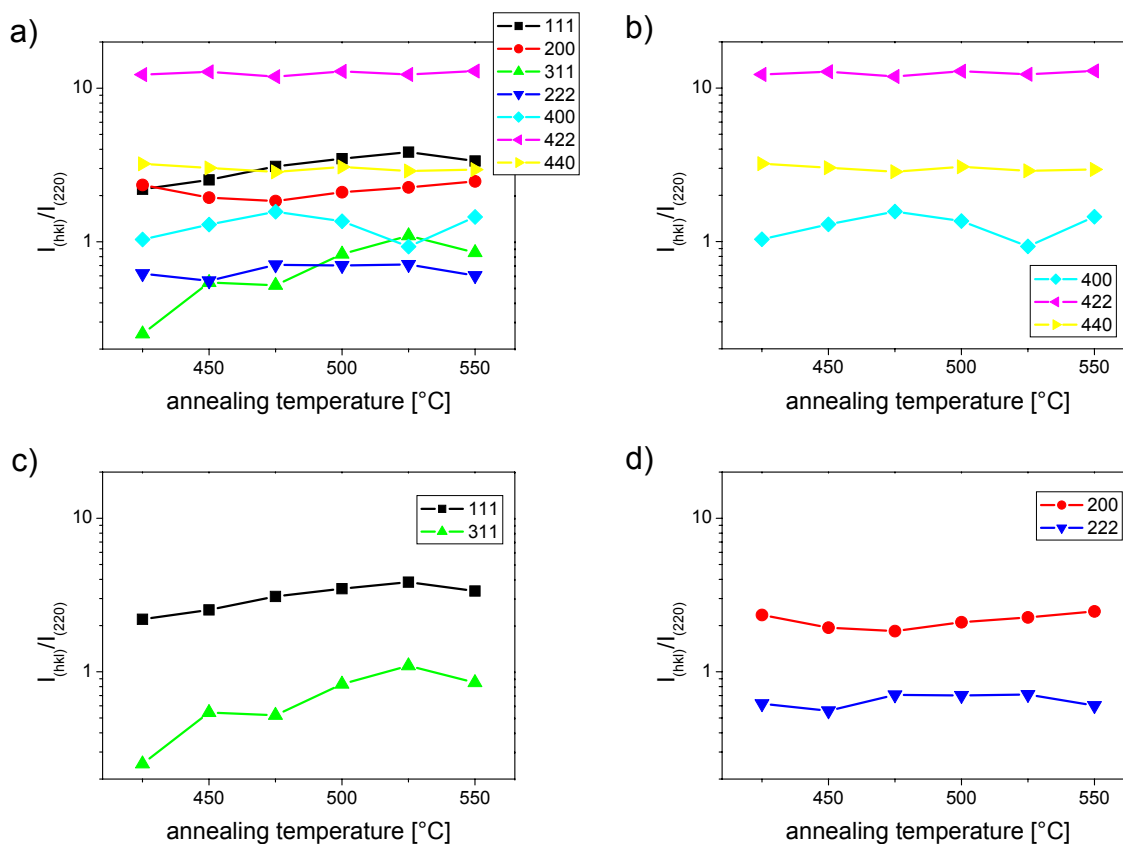


Figure 4.11: a) Intensities of all peaks in the Co_2MnSi x-ray patterns in dependence of annealing temperature; b) fundamental peaks (400), (422) and (440); c) superlattice peaks (111) and (311); d) (200) and (222) superlattice peaks

saturation magnetization will serve again for this purpose, where the more ordered state is characterized by higher magnetization, as has been described before. The resulting correlation is given in Fig. 4.12. With increasing saturation magnetization the (111) peak intensities increase and the (200) ones stay constant. In order to reveal the responsible disorder process, the comparison with the calculated evolution of peak intensities in Fig. 1.6 is necessary. With increasing order or decreasing disorder parameter α , the (111) intensity increases and (200) stays constant only for the Mn-Si disorder. Therefore, it is assumed that the Mn-Si disorder is responsible for the formation of the high saturation magnetization during annealing. In conclusion to the Co-Mn disorder, the following picture of disorder processes is assumed. The drastic increase of saturation magnetization during annealing is provided by Mn-Si disorder and the slight variations of lattice constant and corresponding magnetization is attributed to Co-Mn disorder. These two types of disorder have also mainly been reported in literature for Co_2MnSi thin films [7]. However, all the conclusions on local ordering effects have to be cautiously regarded, since

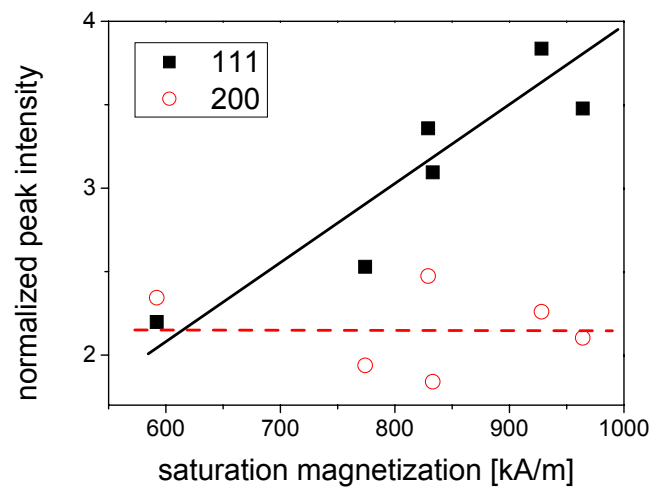


Figure 4.12: Intensities of the superlattice peaks (111) and (200) against the saturation magnetization as a measure of order

they are only valid for perfect polycrystalline or powder samples.

Chapter 5

Preparation II - magnetic tunnel junctions (MTJs)

The previous chapter was mainly dedicated to investigate the physical properties of Co_2MnSi single layered films. However, the application of Co_2MnSi aiming for higher spin polarization requires the integration of Co_2MnSi as electrodes in magnetic tunnel junctions. In contrast to the properties of the single films, the integration of Co_2MnSi thin films inhibits two problems to be mastered. One is to achieve a magnetic switching of Co_2MnSi film within an external field range different from that of the counterelectrode. The second is the interaction with the tunneling barrier, which immediately arises questions about its quality concerning segregation or interdiffusion of the Heusler containing elements to or into the tunneling barrier. As barrier AlO_x is employed due to good understanding of the growing and oxidation process.

Thus the experimental challenge is to adjust the post annealing of the Co_2MnSi film with oxidation of the AlO_x tunneling barrier.

5.1 Magnetic tailoring

The first problem to measure the spin polarization of Co_2MnSi containing MTJs is to ensure separated switching fields of the magnetic electrodes involved. As known from the detailed discussion of Co_2MnSi single layers in chapter 4, the coercive field of annealed Co_2MnSi single layers is in the range of 1 to 2 mT. The choice of a suitable second electrode is firstly directed at a known spin polarization, which will be necessary so as to determine that of Co_2MnSi using a MTJ. Regarding this limitation Py ($\text{Ni}_{80}\text{Fe}_{20}$) or $\text{Co}_{70}\text{Fe}_{30}$ are possible candidates, since their spin polarization was already measured [58]. The second constrain is a coercivity, which should be larger than that of Co_2MnSi to ensure a different magnetic switching range. Unfortunately, neither Py nor $\text{Co}_{70}\text{Fe}_{30}$ are providing a sufficiently large coercivity. Thus it has to be installed via magnetic interaction processes.

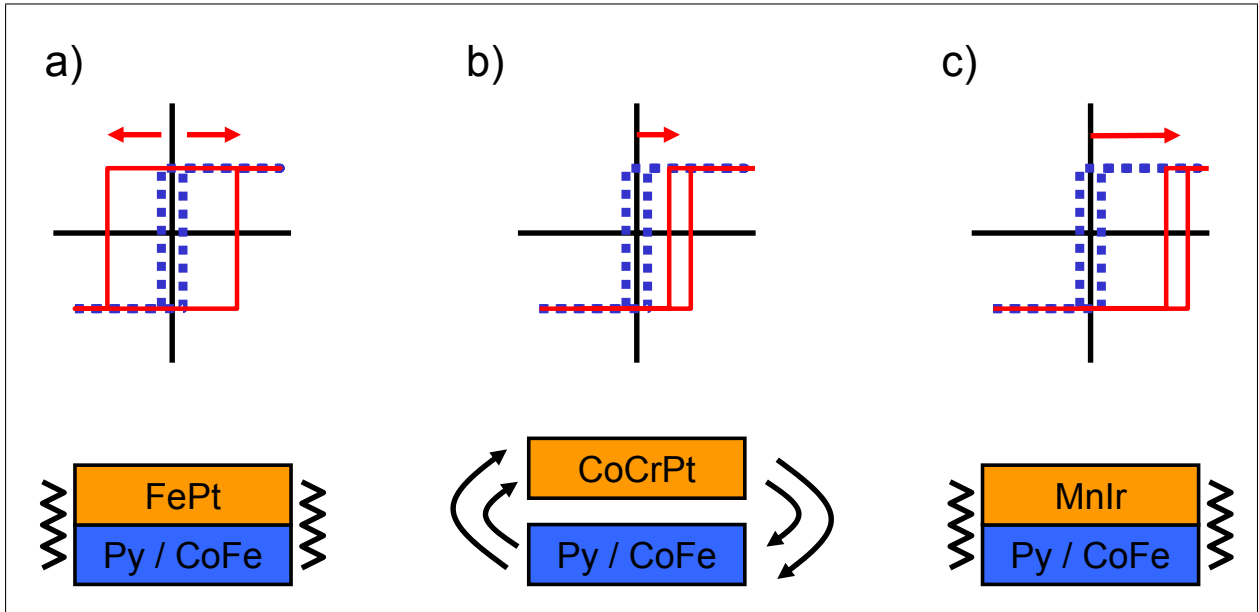


Figure 5.1: Possible magnetic coupling mechanisms to manipulate magnetic switching behavior: a) direct exchange coupling by the hard FePt ferromagnet, b) stray field mechanism and c) pinning by the antiferromagnet MnIr

In the following, three possible techniques to ensure separated magnetic switching behavior will be presented. To realize this, two principle ways are supposable. One way would be to increase the coercivity of one electrode, e.g. $\text{Co}_{70}\text{Fe}_{30}$ or Py, by ferromagnetic coupling to a hard ferromagnet. Alternatively to this hardening, the total hysteresis loop of one magnetic electrode can be shifted. This can be achieved in two ways: the influence by magnetic stray fields or the mechanism of exchange biasing.

For the purpose of magnetic hardening, the exchange interaction of two adjacent ferromagnetic layers is used as in graph a) of Fig. 5.1. The magnetic moments of the soft magnetic film ferromagnetically couple to the hard by exchange interaction over the interface. Single layers of FePt have been studied with respect to high coercivities in thin films with in-plane magnetization [98]. These investigations have shown that coercivities of 500 mT can be reached by annealing up to 550-750 °C. This high temperature window makes FePt not possible as hardening magnet for the upper electrode. The necessary annealing of the complete stack would enable interdiffusion processes and destroy the layered structure. Alternatively, a hardening of the lower electrode, the Co_2MnSi one, seems to be possible, since the FePt layer would firstly be sputtered as single layer. The high temperatures required for the appearance of the hard magnetic FePt phase could separately be applied without annealing the total MTJ stack. However, this way is not preferable due to two reasons. Firstly, the deposition of Co_2MnSi on top of FePt would fundamentally change the growth conditions and, hence, it cannot be ensured that the fine quality of Co_2MnSi films on top of silicon oxide and vanadium can be transferred. Secondly, annealing even

in vacuum of 2×10^{-7} mbar make adatoms settle at the FePt surface. Such impurities at the FePt-Co₂MnSi interface sensitively disturb the coupling process [99]¹.

A second way to ensure separated switching of the two electrodes is to shift the hysteresis loop of one of the two electrodes. One technique to provide such a shift is to use the stray field of a hard magnetic film as denoted in graph b) of Fig. 5.1. This effect was studied on CoCrPt with CoFe/Cu-multilayers [100]. The stray field of CoCrPt acts as bias field. The switching process of a magnetic layer is assisted by the bias field (lower coercivity), if external field is applied in same direction, and the coercive field is increased opposite direction. However, a considerable shift is achieved in structure sizes of a few micrometers [101]. This additional feature would drastically complicate the total preparation and characterization process.

The used alternative technique is to provide pinning by an antiferromagnet. If an antiferromagnet is field cooled in direct contact with a ferromagnet, an unidirectional anisotropy is established. The magnetization reversal is shifted by the exchange bias field as shown in graph c) of Fig. 5.1. How this mechanism works on atomic scale is controversially discussed in literature. A good review of possible theories is given in [102, 103, 104]. However, the exchange bias shift can phenomenologically be described by the local magnetic moments in both the antiferromagnetic and ferromagnetic layer. Within this picture the task of the field cooling process becomes obvious. At a temperature higher than the Neel temperature of the antiferromagnet but lower than the Curie temperature of the ferromagnet, the magnetic moments in the antiferromagnet are randomly oriented, where the ones in the ferromagnet are ferromagnetically coupled. When cooling down in an external field, the antiferromagnet orders in its antiferromagnetic superstructure. The direct contact to the aligned moments in the ferromagnet during field cooling establishes the unidirectional anisotropy. The aspect of the direct contact makes clear that any present impurities would sensitively disturb the exchange bias mechanism².

To establish the exchange bias mechanism, various oxides of the transition metals, e.g. CoNiO or NiO, or manganese containing alloys, e.g. have intensively been studied with respect to their exchange bias properties [105]. The antiferromagnet Mn₈₃Ir₁₇ (MnIr) produce large shifts of the hysteresis loop of adjacent ferromagnetic layer [106, 107]. The exact shift can be adjusted by the choice of the individual film thicknesses [58]. As ferromagnetic material Co₇₀Fe₃₀ is chosen and the field cooling process is provided by annealing to 275 °C for 60 minutes in a field of 100 mT. The used thicknesses are 5 and 10 nm for Co₇₀Fe₃₀ and MnIr, respectively.

¹Experiments by deposition of Co₂MnSi onto FePt ex-situ prepared films do not show ferromagnetic coupling or any other interaction.

²Measurements on MTJs, which were prepared up to Co₇₀Fe₃₀, annealed for the Co₂MnSi ordering and then topped by MnIr, do not show the exchange bias.

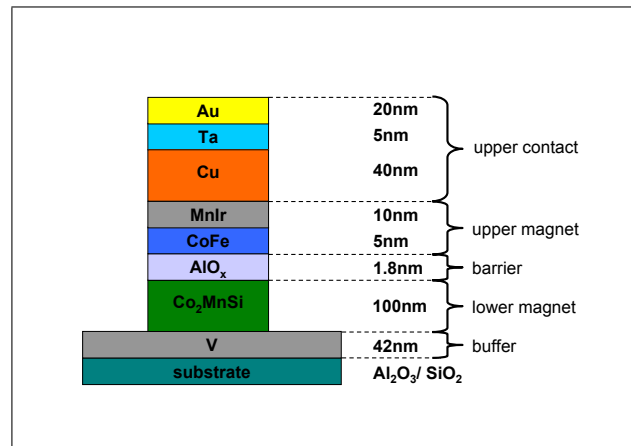


Figure 5.2: Stack character of the investigated magnetic tunnel junctions (MTJ)

5.2 The barrier

To provide a tunnel current between the two ferromagnetic electrodes, they have to be separated by vacuum or as in the present case, by an insulating barrier. Different materials such as MgO [10], SrTiO₃ [108] or Al₂O₃ [58, 10] are potential candidates. In the present work the most common used one, namely aluminum oxide or sapphire (Al₂O₃), is employed as the barrier material. As an insulator it exhibits a band gap of 10 eV [109]. Additionally, it is characterized by a large formation enthalpy of -380 kcal/mol [110]. Consequently, it is assumed that its formation is more preferable in comparison to other possible oxides, which can originate from the Heusler-elements upon annealing in the MTJs barrier region. Another aspect favoring Al₂O₃ is its known formation by subsequent oxidation of deposited aluminum. The oxidation of the aluminum can be achieved by employing different methods as native [111], thermally [112] or plasma [113] oxidation. Using native oxidation, an aluminum oxide passivation layer of 1-2 nm can be formed [84, 66]. To realize thicker insulating layers, thermally or plasma assisted oxidation has to be established. In the present work, in-situ plasma oxidation is applied and an ex-situ annealing procedure so as to heal barrier defects [114, 115]. This healing takes place in the field cooling process to activate the exchange bias [58]. Even by use of the described techniques it is questionable, if the optimum stoichiometry (Al₂O₃) is present due to the unknown kinetic situation during the oxidation process. Thus, it will be spoken of AlO_x in the future.

5.3 The stack - patterning

The basic structure of the MTJ used in this work is illustrated in Fig. 5.2. Its main features are the two magnetic electrodes, one of which magnetically exchange biased, separated by the insulating AlO_x layer. To force the current tunnel through the insulating barrier, a special design has to be realized. The so-called CPP geometry (**C**urrent **P**erpendicular

to Plane) requires a stack-like design. For this purpose stacks with cross-sections of (100×100 - $300 \times 300 \mu m^2$) have to be patterned out of the multilayered thin film, as it has been prepared by magnetron sputtering. Optical lithography technique in combination with argon ion etching enables one to achieve the stack shown in Fig. 5.2. To form the etching mask, optical positive resist is deposited onto the layer system by a spin-coater. This establishes a homogeneous film over the complete substrate and the rotation speed determines the resist thickness. Afterwards the resist has to harden by annealing at $95^\circ C$ for 30 minutes. Then the optical exposure follows. The exposed structures are developed and the resulting mask can be used for ion beam etching. Through the uncapped places the layered system is locally ablated. The Ar ion etching stops in the middle of 100 nm thick Co_2MnSi layer. After removing the rest of the resist, the sample is ready to be characterized.

5.4 The final process layout

The preparation of MTJs containing Co_2MnSi as lower electrode demands many special aspects as discussed in the previous paragraphs. To respect all these demands, the process, which will be described in the following, has been developed. It can be divided into seven steps as illustrated in Fig. 5.3. The start is made by DC magnetron sputtering of V(42 nm)/ Co_2MnSi (20-100 nm)/Al(1.4 nm) and subsequent plasma oxidation at 275 W for 100 sec to form the 1.8 nm thin AlO_x barrier a). This is the setup for (110) textured samples. If polycrystalline samples are investigated, the vanadium seed layer is absent. To ensure the $L2_1$ Heusler phase in Co_2MnSi , the system is annealed in-situ up to $\sim 450^\circ C$ for 40 minutes b). By this strategy it is accepted that the surface of the AlO_x is contaminated by a few monolayers of adatoms [116]. When the sample cools down to room temperature by radiation during hours without any active cooling system, the following layer sequence is started by an extra oxidation for 50 sec at a power of 275 W c). This step has two consequences. First, the surface is freed by the adatoms by reaction with the oxygen ions³ and the aluminum oxidation is completed to the optimal oxygen content of 200 sec in optimum reference samples [58]. Afterwards the process is back in standard process sequence d). The upper electrode is DC/RF magnetron sputtered and consists of 5 nm CoFe ($Co_{70}Fe_{30}$) and for the purpose of exchange biasing topped by 10 nm MnIr ($Mn_{83}Ir_{17}$). The deposition is closed by the upper contact (Cu(40 nm)/Ta(5 nm)/Au(30 nm)), in which each individually layer fulfills its job. The copper provides as mechanical buffer to prevent damage of the barrier during the electrical characterization, when tapping with a tip on top of the stack. The top gold layer protect the complete stack from oxidation and provides good electrical contact with gold tips and perfect surface for bonding by gold wire. The interfacial tantalum layer serves again for two jobs. Firstly, to give the gold layer permanent mechanical contact to the copper layer and, secondly, to prevent diffusion of the gold atoms

³The fine quality of the $AlO_x/Co_{70}Fe_{30}$ interface will be confirmed by IET spectroscopy in chapter 7.

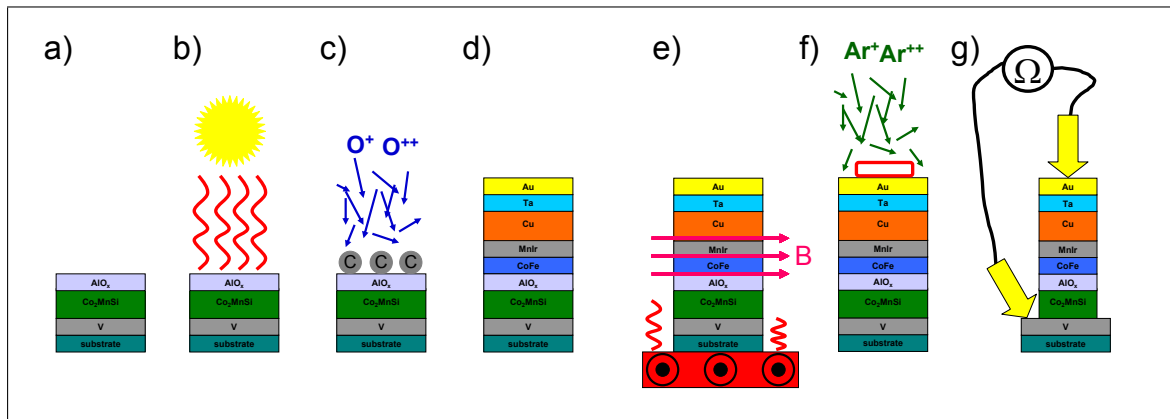


Figure 5.3: Scheme of the final process: a) DC magnetron sputtering up to Al 1.4 nm plus plasma oxidation at 275 W for 150 sec; b) post annealing (40 min at $\sim 450^\circ\text{C}$) without break of vacuum to achieve L_{21} phase; c) additional oxidation for free surface by adatoms at 275 W for 50 sec; d) DC/RF magnetron sputtering of upper electrode consisting of CoFe (5 nm) / MnIr (10 nm) and upper contact; e) field cooling 60 min at 275°C in magnetic field of 100 mT to activate exchange bias mechanism; f) deposition of etching mask by optical lithography and following argon ion etching; g) resulting layer stack ready for magnetoresistive characterization

into the copper during subsequent field cooling ⁴.

In the present state the stack is complete with respect to layer deposition. Now to activate the exchange bias, the total layer system has to be field cooled in the previous described way e). For a duration of 60 minutes, the stack system is annealed up to 275°C in a field of 100 mT. Additionally to the exchange bias activation, the annealing process enables healing of imperfections in the AlO_x barrier [114, 115].

Now all layers are deposited and functionalized. The layered system is in its final stage. However, to electrically characterize the MTJ, the patterning has to be done as described in the previous chapter f). After this patterning process the MTJ is ready to be characterized g).

⁴Alternatively, the reader may think of two other stages to separate the process with respect to the two distinguished annealing processes: prior the deposition of the aluminum or before the MnIr deposition. Both sequences have been tested. However, the first approach has as consequence a vanishing TMR amplitude, although perfect magnetic switching is apparent. The second one destroys the antiferromagnetic coupling between the $\text{Co}_{70}\text{Fe}_{30}$ and the MnIr. Hence, the applied sequence is best with compromise to the $\text{AlO}_x/\text{Co}_{70}\text{Fe}_{30}$ interface.

Chapter 6

Spin polarization in thin Co_2MnSi films

Measuring spin polarization, especially in thin films, is yet a challenging task. Various techniques have been presented in paragraph 3.4. The main efforts in the framework of this thesis are concentrated to the determination of spin polarization by magnetic tunnel junctions (MTJs). In the following paragraphs the experimental results will be discussed. Starting with magnetic, electrical and magnetoresistive results for samples with highest TMR-amplitude, before details of the Heusler-barrier-interface characteristics will be presented. Thereafter possibilities for optimization of the TMR amplitude are given. Subsequently the spin polarization will be correlated to magnetic and microstructural parameters of the Co_2MnSi Heusler alloy.

6.1 TMR effect amplitude and spin polarization realized

The discussion of the magnetic tunnel junctions consisting of Co_2MnSi as one electrode will start with the experimentally realized magnetoresistance. It depends on the separate switching of the Co_2MnSi and exchange biased $\text{Co}_{70}\text{Fe}_{30}$ electrodes. Fig. 6.1 a) displays the magnetic switching of a MTJ consisting of $\text{SiO}_2(100\text{ nm})//\text{V}(42\text{ nm})/\text{Co}_2\text{MnSi}(100\text{ nm})/\text{AlO}_x(1.8\text{ nm})/\text{Co}_{70}\text{Fe}_{30}(5\text{ nm})/\text{MnIr}(10\text{ nm})/\text{Cu}(40\text{ nm})/\text{Ta}(5\text{ nm})/\text{Au}(20\text{ nm})$. The total hysteresis loop is a superposition of the individual hysteresises of the soft magnetic Co_2MnSi and the exchange biased $\text{Co}_{70}\text{Fe}_{30}$ -layer. The switching of Co_2MnSi incorporated in the MTJ is very similar to that of single layered films and is characterized by a coercivity of 1.7 mT indicating that the hysteresis is symmetric about zero external field. In contrast, the hysteresis loop of the exchange biased $\text{Co}_{70}\text{Fe}_{30}$ is shifted by 42.5 mT and has a coercivity of 7.8 mT. Hence, it can be conducted that the magnetic switching fields of the magnetic electrodes are sufficiently apart so as to ensure large TMR effect amplitudes.

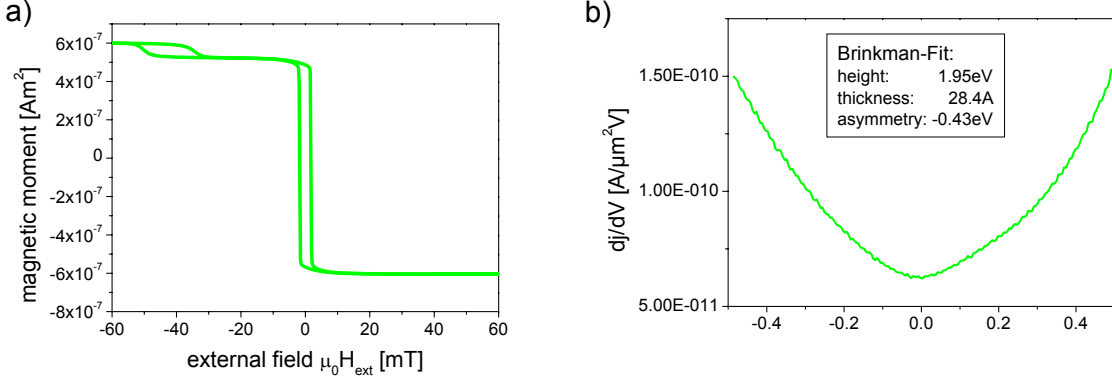


Figure 6.1: Typical magnetic and electrical behavior of prepared MTJs: a) clearly distinct coercivities provide the full TMR-amplitude and b) differential conductance G vs. bias voltage V revealing tunnel barrier characteristics

The second precondition to be fulfilled in a working magnetic tunnel junction is the quality of the AlO_x tunnel barrier. A first indication for a reasonable tunneling barrier is the presence of a parabolic dependence of the differential conductance G on the applied bias voltage V as seen in Fig. 6.1 b). The parabolic behavior can be fitted by use of the subsequently described Brinkman formalism resulting in a barrier height ϕ of 1.95 eV, a barrier thickness d of 28.4 Å and a barrier asymmetry $\Delta\phi$ of -0.43 eV. In comparison to optimized $\text{Co}_{70}\text{Fe}_{30}/\text{AlO}_x/\text{Co}_{50}\text{Fe}_{50}$ tunnel junctions ($\phi=3.0$ eV, d of 18.0 Å, $\Delta\phi=1.24$ eV), all three barrier parameters significantly differ and give rise to assume an imperfect barrier. However, a TMR ratio of 33 % at room temperature and of 86 % at 10 K can be achieved, which relates to a spin polarization of 61 %. This measured spin polarization is already exceeding that of all 3d metals and their alloys [10, 91]. Reducing the applied voltage from 10 mV to 1.0 mV, while measuring the magnetoresistance, the TMR amplitude can be increased to 95 % at 10 K resulting in a spin polarization of 66 %. The answers to the questions initiated by these results such as quality, temperature dependence of the TMR amplitude etc. are left for the following.

6.1.1 Quality of the interface I - electrical behavior

The electrical current flowing through an insulating barrier is very sensitive to the quality of this barrier [10] and can already be influenced by small deviations in atomic distribution [69, 65]. Few imperfections can vary the electrical and temperature dependent characteristics extremely [117, 118, 119, 71, 70].

Pinholes enabling an additional unpolarized channel to the tunnel current or spin scattering centers resulting in spin-flip during tunneling [71] will reduce the TMR amplitude. An enhancement by spin filtering effects [75, 120] or resonant tunneling [121, 122, 123, 124] is also possible. In order to determine these influences, a detailed study of the I - V - and/or

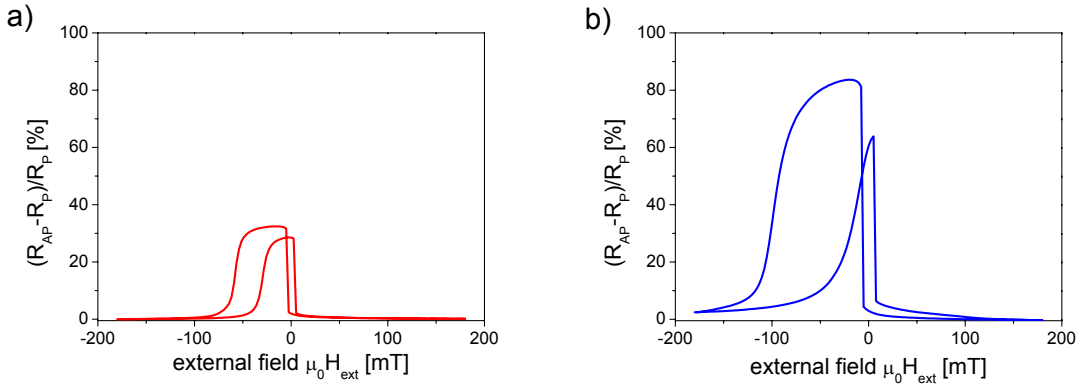


Figure 6.2: a) Best TMR measurement with TMR amplitude of about 33% at room temperature and b) 86% at 10 K resulting in spin polarization of 61% for Co_2MnSi ; after [94]

G - V -characteristics is needed.

I - V - and G - V -characteristics

The occurrence of a tunnel current is revealed by its characteristic I - V - or G - V -characteristic. The typical parabolic behavior of G - V -curves identifies the tunneling process. Therefore, the understanding of the exact G - V -curve can provide additional information of the barrier. To be able to quantify the quality of the barrier, a model proposed by Brinkman [64] is applied.

This model is based on two fundamental assumptions. The first is concerning the physical factors contributing to the tunnel current and the second the potential shape of the barrier. The shape proposed by Brinkman is displayed in Fig. 6.3. This simple model of the barrier neglecting the detailed shape is described by the three barrier parameters thickness d , height ϕ and asymmetry $\Delta\phi$. This model by Brinkman is an extension to the earlier model by Simmons [125] by addition of the barrier asymmetry to account for different materials of the electrodes. For perfect samples determined by sharp interfaces between the barrier and adjacent electrodes, the barrier asymmetry reveals the difference of the work functions of the two electrodes [65], the barrier thickness is a real measure of this quantity [58] and the height displays the mean potential barrier height. Variations of the barrier quality on atomic scale sensitively influence the barrier parameters in general, but especially the barrier asymmetry [69, 65].

The second assumption concerns the term of the tunnel current between to metallic electrodes separated by an insulating. It can be presented by the difference $I = I_{12} - I_{21}$ between tunnel current I_{12} defined by the current from electrode 1 to electrode 2 and by the one in opposite direction I_{21} . For the tunnel current I_{12} , the number of tunneling electrons is proportional to the available electrons in the emitting electrode 1 $\rho_1(E) \times f(E)$,

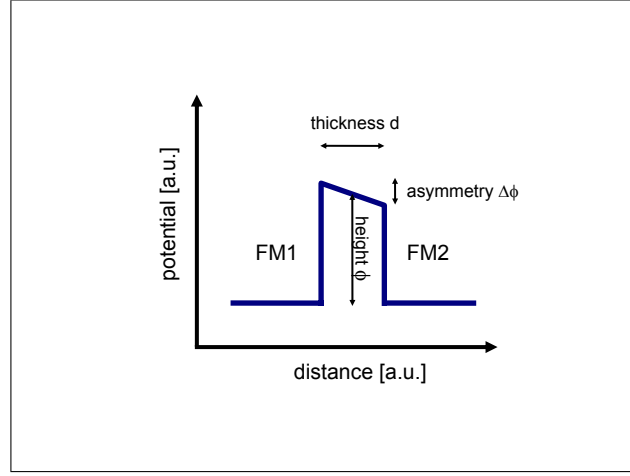


Figure 6.3: Potential of the insulating barrier proposed by Brinkman [64]

the free states in the absorbing electrode 2 $\rho_2(E) \times (1 - f(E))$ and the probability for transmission of an electron $|T|^2$, where ρ_i denotes the density of states at energy E and f the Fermi-Dirac function. If then a voltage V is applied ¹, the tunnel current I_{12} is described by:

$$I_{12} = \int \rho_1(E)\rho_2(E + eV)|T|^2 f(E) \left(1 - f(E + eV)\right) dE \quad (6.1)$$

The approach of Brinkman treats the $|T|^2$ -term within the WKB approximation and this makes the evaluation of the total tunnel current I possible. The resulting term of the G - V -characteristic reveals a parabolic behavior of the form: $G = A \cdot V^2 + B \cdot V + C$. Fitting the measured G - V -curve to this formula provides the three barrier parameters by the following equations:

$$\phi^2 = \frac{e^2 C}{32A} \ln^2 \left(\frac{h^3}{\sqrt{2}\pi e^3 m_{eff}} \sqrt{AC} \right) \quad (6.2)$$

$$d = -\frac{\hbar}{2\sqrt{2}\phi m_{eff}} \ln \left(\frac{h^3}{\sqrt{2}\pi e^3 m_{eff}} \sqrt{AC} \right) \quad (6.3)$$

$$\Delta\phi = -\frac{12\hbar B}{\sqrt{2}m_{eff}eC} \frac{\phi^{\frac{3}{2}}}{d} \quad (6.4)$$

m_{eff} is the effective electron mass and is set to $m_{eff} = 0.4 \cdot m_e$ [126]. Applying this formalism to the measured G - V -curves gives the opportunity to judge the quality of the barrier in a quantitative manner.

This model also includes a simple relation between barrier resistance and barrier parameters $R \propto d\sqrt{\phi}$. Thus, the barrier resistance is the first parameter accessible by

¹In the following discussions of the I - V - and G - V -characteristics the applied voltage V is defined with respect to the potential of the lower electrode

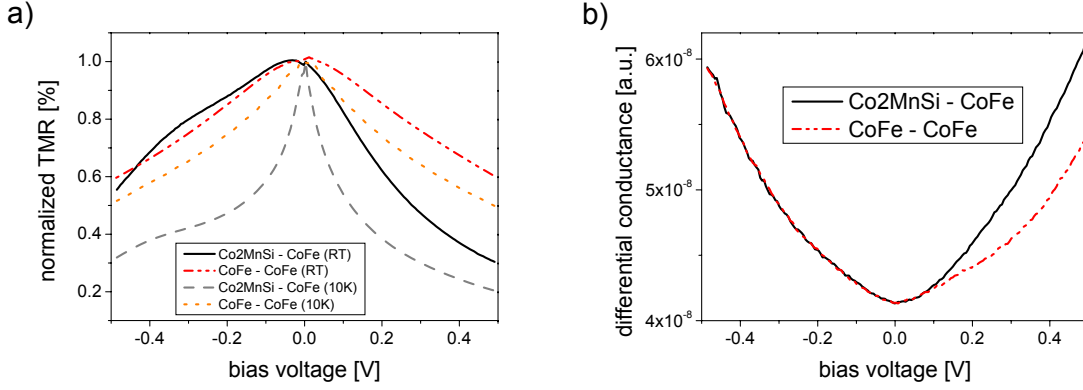


Figure 6.4: a) Difference between $\text{Co}_{70}\text{Fe}_{30}/\text{AlO}_x/\text{Co}_{50}\text{Fe}_{50}$ (CoFe-CoFe) and $\text{Co}_2\text{MnSi}/\text{AlO}_x/\text{Co}_{70}\text{Fe}_{30}$ (Co₂MnSi-CoFe) magnetic tunnel junctions in bias voltage dependence of TMR amplitude; b) G - V -characteristics

electrical measurements and provides first evaluation on the barrier constitution. Since the electrical characterization is performed on 100×100 - $300 \times 300 \mu\text{m}^2$ area sizes, the element size independent product of area and resistance is considered for more transparency. In case of the $\text{Co}_2\text{MnSi}/\text{AlO}_x/\text{Co}_{70}\text{Fe}_{30}$ tunnel junctions a typical area resistance RA is in the range 10 - $20 \text{ G}\Omega\mu\text{m}^2$, where the barrier thickness is about 28 \AA . This is larger by a factor of 1000 to $\text{Co}_{70}\text{Fe}_{30}/\text{AlO}_x/\text{Co}_{50}\text{Fe}_{50}$ optimally prepared samples with a typical RA of $20 \text{ M}\Omega\mu\text{m}^2$ for a 18 \AA barrier. Since the AlO_x barrier preparation has been identically made for both MTJs, the question concerning the origin of the thicker barrier in case of $\text{Co}_2\text{MnSi}/\text{AlO}_x/\text{Co}_{70}\text{Fe}_{30}$ arises, but its answer will be postponed until the underlying interfacial microstructure is known.

The TMR bias voltage dependence given in Fig. 6.4 a) reveals a asymmetric dependence for the $\text{Co}_2\text{MnSi}/\text{AlO}_x/\text{Co}_{70}\text{Fe}_{30}$ tunnel junction, which is very different from the behavior of the $\text{Co}_{70}\text{Fe}_{30}/\text{AlO}_x/\text{Co}_{50}\text{Fe}_{50}$ junction. Consequently, the tunneling process of the former depends on the direction of the applied bias voltage. The TMR amplitude is reduced, when the net current of electrons is directed from Co_2MnSi to $\text{Co}_{70}\text{Fe}_{30}$. Thus, an increase of the barrier thickness is causing a more pronounced asymmetry of TMR voltage dependence. Measurements performed at 10 K , where possible excitations such as magnons and phonons are frozen out, become more symmetric.

Comparing the corresponding G - V -curves for both cases in Fig. 6.4 b) reveals the major difference. The corresponding Brinkman fits provide asymmetries of -0.35 eV for $\text{Co}_2\text{MnSi}/\text{AlO}_x/\text{Co}_{70}\text{Fe}_{30}$ and 1.24 eV for $\text{Co}_{70}\text{Fe}_{30}/\text{AlO}_x/\text{Co}_{50}\text{Fe}_{50}$ tunnel junctions.

The first idea to clear up this change in barrier asymmetry is the change of the work function difference from $\text{Co}_{70}\text{Fe}_{30}$ to Co_2MnSi as lower electrode. The change in barrier asymmetry is determined to be $+1.6 \text{ eV}$. After the model of Brinkman the barrier asymmetry equals the difference of the work functions of the two electrodes $\Delta\Phi = \Phi_1 - \Phi_2$. Then the difference between the between $\Delta\Phi_{\text{Co}_2\text{MnSi}/\text{AlO}_x/\text{Co}_{70}\text{Fe}_{30}}$ and $\Delta\Phi_{\text{Co}_{70}\text{Fe}_{30}/\text{AlO}_x/\text{Co}_{50}\text{Fe}_{50}}$ is $\Phi_{\text{Co}_2\text{MnSi}} - \Phi_{\text{Co}_{70}\text{Fe}_{30}}$ when assuming $\Phi_{\text{Co}_{50}\text{Fe}_{50}} = \Phi_{\text{Co}_{70}\text{Fe}_{30}}$ and should present the change

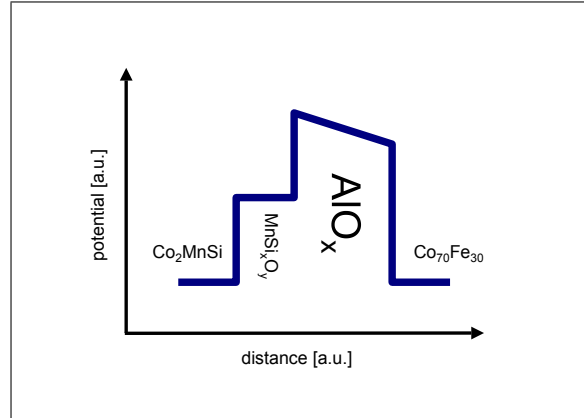


Figure 6.5: Extension of the simple barrier model by Brinkman to a step-like barrier shape

in barrier asymmetry. However, if the work functions of single elements Co, Mn and Si are regarded (Co: $\Phi = 5\text{ eV}$ [43], Mn: $\Phi = 3.8\text{ eV}$, Si: $\Phi = 4.2\text{ eV}$ [109]), it seems to be reasonable that the work function of Co_2MnSi is smaller that or in maximum equal to the one of $\text{Co}_{70}\text{Fe}_{30}$. Hence, the difference $\Phi_{\text{Co}_2\text{MnSi}} - \Phi_{\text{Co}_{70}\text{Fe}_{30}}$ is negative or near zero, which is in contrast to the drastic positive change of measured barrier asymmetry. This rejects the argument of work function change of the electrodes as reason for the change of barrier asymmetry from $\text{Co}_{70}\text{Fe}_{30}/\text{AlO}_x/\text{Co}_{50}\text{Fe}_{50}$ to $\text{Co}_2\text{MnSi}/\text{AlO}_x/\text{Co}_{70}\text{Fe}_{30}$ MTJs.

Additionally to the change in barrier asymmetry, the tunneling resistance or better the area resistance increases as denoted before. It is by a factor of 1000 higher for the $\text{Co}_2\text{MnSi}/\text{AlO}_x/\text{Co}_{70}\text{Fe}_{30}$ than for the $\text{Co}_{70}\text{Fe}_{30}/\text{AlO}_x/\text{Co}_{50}\text{Fe}_{50}$ MTJ. Therefore, an increase of the barrier thickness of 0.5 nm for the $\text{Co}_2\text{MnSi}/\text{AlO}_x/\text{Co}_{70}\text{Fe}_{30}$ MTJ can account for its higher area resistance due to the exponential dependence of the area resistance with the barrier thickness [64]. This increase of barrier thickness is qualitatively confirmed by the Brinkman-Fit of the G - V -curves, which reveal an increase from 18 Å to 28 Å.

Therefore, the interfaces of the two electrodes to the barrier have to be considered. Due to the asymmetric TMR voltage dependence of the $\text{Co}_2\text{MnSi}/\text{AlO}_x/\text{Co}_{70}\text{Fe}_{30}$ MTJ it seems to be reasonable that the atomic concentration of this additional part of the barrier is also asymmetric distributed. The comparison to the $\text{Co}_{70}\text{Fe}_{30}/\text{AlO}_x/\text{Co}_{50}\text{Fe}_{50}$ MTJ, which shows symmetric behavior, reveals that the critical interface has to be the one between Co_2MnSi and AlO_x . The upper $\text{AlO}_x/\text{Co}_{70}\text{Fe}_{30}$ interface is identically prepared for the two MTJs.

To summarize, from electrical point of view an additional barrier of 0.5 nm has to be present at the $\text{Co}_2\text{MnSi}/\text{AlO}_x$ interface. Such a step-like barrier sketched in Fig. 6.5 clears up the increase in barrier thickness and accordingly in area resistance, but also reveals the change of barrier asymmetry and height in the described way as was demonstrated by simulations by [69, 65]. How this additional part of the barrier is composed of on atomic scale is open here. Therefore, the labeling by MnSi_xO_y in Fig. 6.5 anticipates on the

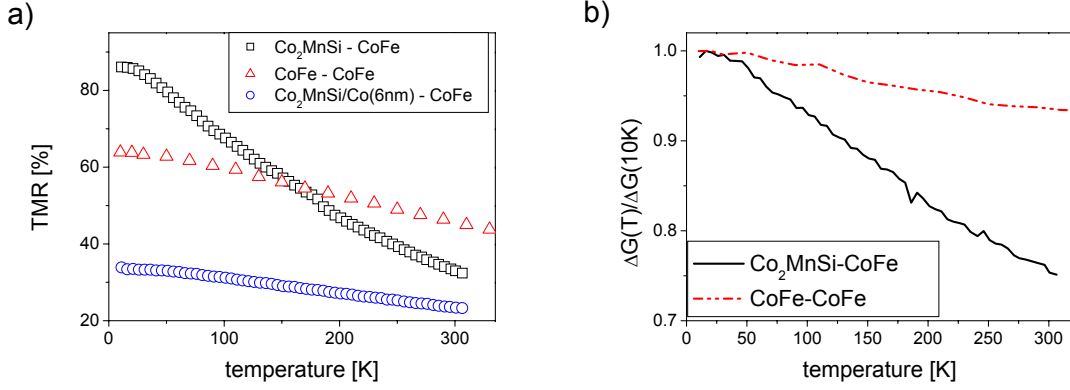


Figure 6.6: a) Temperature evolution of TMR amplitude and b) of ΔG : MTJ containing Co₂MnSi as one electrode showing very different behavior with respect to the Co₇₀Fe₃₀/AlO_x/Co₅₀Fe₅₀ MTJ

coming investigations.

Temperature dependence of TMR amplitude

Measuring the TMR effect amplitude from 10 K to room temperature yields its temperature dependence given in Fig. 6.6 a). The TMR amplitude about 86% at 10 K and only 33% at room temperature hence showing a much stronger reduction of the TMR with increasing temperature as was observed for Co₇₀Fe₃₀/AlO_x/Co₅₀Fe₅₀. A conclusive explanation of this TMR temperature dependence is very complicated due to a variety of different contributions to the total conductance such as direct tunneling, magnon and/or phonon assisted tunneling, spin scattering on paramagnetic ions or unpolarized conductance via defect states in the barrier. Here it is focussed on the latter possibility, which has been modeled by Shang *et al.* [70] describing the total conductance G through the barrier between the two magnetic electrodes with spin polarization P_1 and P_2 relatively oriented to each other by an angle θ :

$$G(\theta, T) = G_T(T) \left(1 + P_1(T)P_2(T) \cos \theta \right) + G_{SI}(T) \quad , \quad (6.5)$$

where G_T takes into account the direct elastic scattering and G_{SI} the unpolarized tunnel current. Equation (6.5) contains three temperature dependent contributions namely each spin polarization P_1 and P_2 , G_T and G_{SI} .

The temperature dependence of the elastic scattered tunnel current G_T is attributed to the broadening of the Fermi distribution with increasing temperature [70] and is given by [70]:

$$G_T = G_0 \frac{CT}{\sin CT} \quad , \quad (6.6)$$

| | T_c [K] | | a [K ^{-$\frac{3}{2}$]} | |
|-----------------------------------|-----------------|------|--|-------|
| Co | 1394 | [15] | $1 - 6 \times 10^{-6}$ | [70] |
| Co ₇₀ Fe ₃₀ | Fe:1043-Co:1394 | [15] | 7.6×10^{-6} | [58] |
| Co ₂ MnSi | 985 | [4] | bulk 2.8×10^{-6} | [127] |
| Py | 850 | [70] | $30 - 50 \times 10^{-6}$ | [70] |

Table 6.1: Magnetic characteristics describing magnetic temperature dependence: Curie temperature T_c and spin stiffness a ; the spin stiffness were calculated from MTJ measurements for all materials except the case of Co₂MnSi for which it was determined on a single crystal sample

where $C = 1.387 \times 10^{-4}d/\sqrt{\phi}$ with barrier thickness d and height ϕ to be extracted from corresponding G - V -characteristics and G_0 at $T=10$ K ².

In order to access the temperature dependence of spin polarization, within this model it is assumed that spin polarization and magnetization are correlated [72, 10] exhibiting both a temperature dependence proportional to the $T^{\frac{3}{2}}$ law, which is at least confirmed for magnetization of Co₂MnSi [4, 127]³:

$$P(T) = P_0 \left(1 - aT^{\frac{3}{2}} \right), \quad (6.7)$$

where a is the material-dependent spin stiffness. Typical values are listed in Tab. 6.1. The spin stiffness values except the one of Co₂MnSi have been determined by MTJ investigations. The Co₂MnSi spin stiffness originates from magnetometric measurements of bulk samples. This value can only be a rough estimate of the thin film spin stiffness of Co₂MnSi, since by MTJs the surface magnetism is probed [128]. However, by comparison of the related Curie temperatures the range for Co₂MnSi thin films can be estimated. Since the Curie temperature is between the ones of Py and Co₇₀Fe₃₀, the spin stiffness should be in the range of $7.6-50 \times 10^{-6} \text{ K}^{-\frac{3}{2}}$.

Lastly, the temperature dependence of the spin independent tunnel current G_{SI} has to be considered as well and can be attributed to several thermal activated processes. One proposed by Shang [70] is the hopping of electrons through the barrier via imperfections. The consequence of a spin independent tunnel current G_{SI} is a reduction of the measured TMR amplitude, which is given by:

$$TMR = \frac{2P_1(T)P_2(T)}{1 - P_1(T)P_2(T) + \frac{G_{SI}}{G_T}}. \quad (6.8)$$

²The barrier height and thickness are taken from G - V -characteristics measured at room temperature. Due to the high bias voltage up to 500 mV the main part of the parabolic G - V -curve is not influenced by the thermal energy of >25 meV at room temperature. Thus, the room temperature as well as the 10 K I - V -measurement reveals the same barrier parameters. However, for magnetic electrodes and at low temperatures the G - V -curve differs from the typical parabolic shape and this makes the fitting procedure to be more inaccurate.

³However, this correlation is not necessarily true, in principle, and, especially, not for the Heusler alloys [39].

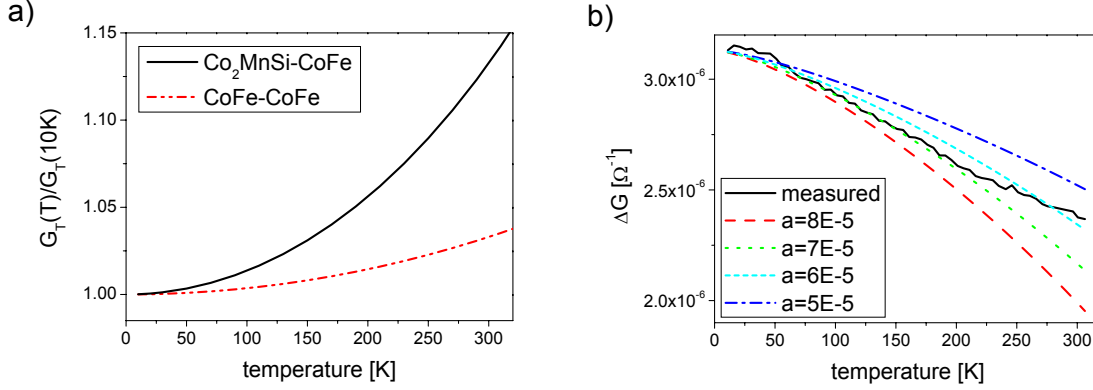


Figure 6.7: a) Temperature dependent tunnel current G_T for the different tunnel barriers; b) fitting of ΔG -temperature dependence including magnon excitation

The introduction of all temperature dependent contributions considered now enables to analyze the strong temperature dependence of the TMR amplitude quantitatively. To extract G_{SI} and G_T from experimental data two additional relations are useful. The difference of the experimental conductances of the parallel and antiparallel state must be independent of spin unpolarized tunnel current G_{SI} , since it is a constant contribution to both states, and thus:

$$\Delta G = G_{\uparrow\uparrow} - G_{\uparrow\downarrow} = G(\theta = 0^\circ, T) - G(\theta = 180^\circ, T) = 2G_T P_1(T) P_2(T), \quad (6.9)$$

where G_T is calculated by the use of equation (6.6). The constant C is determined as previously described and G_0 is taken at 10 K by use of equation (6.5) and assuming G_{SI} is zero. This assumption is legitimated by freezing out of thermal activated processes providing the unpolarized tunnel current. The unpolarized tunnel current G_{SI} can be extracted as follows from experimentally determined conductance:

$$G_{SI} = \frac{G_{\uparrow\downarrow} + G_{\uparrow\uparrow}}{2} - G_T \quad (6.10)$$

The sum over the parallel and antiparallel state cancels out the spin polarization part $P_1(T)P_2(T) \cos \theta$. The division by two and subsequent subtraction by G_T reveals the unpolarized tunnel current G_{SI} .

Investigating the temperature dependence of the spin dependent tunnel current G_T first, it becomes clear that the barrier parameters height ϕ and thickness d are dominating this part. Consequently, the different parameters determined for the $\text{Co}_2\text{MnSi}/\text{AlO}_x/\text{Co}_{70}\text{Fe}_{30}$ ($\phi=1.93$ eV and $d=2.85$ nm) in comparison to that for $\text{Co}_{70}\text{Fe}_{30}/\text{AlO}_x/\text{Co}_{50}\text{Fe}_{50}$ ($\phi=2.90$ eV and $d=1.80$ nm) lead to a much stronger temperature dependent current G_T for the MTJ containing Co_2MnSi . This is seen in Fig. 6.7 a). G_T of the MTJ containing Co_2MnSi shows an increase of about 15% with temperature, while that of the $\text{Co}_{70}\text{Fe}_{30}/\text{AlO}_x/\text{Co}_{50}\text{Fe}_{50}$ tunnel junction only decreases about 5%. Now where the temperature dependence of G_T have been determined, the temperature dependence of the spin polarizations can be

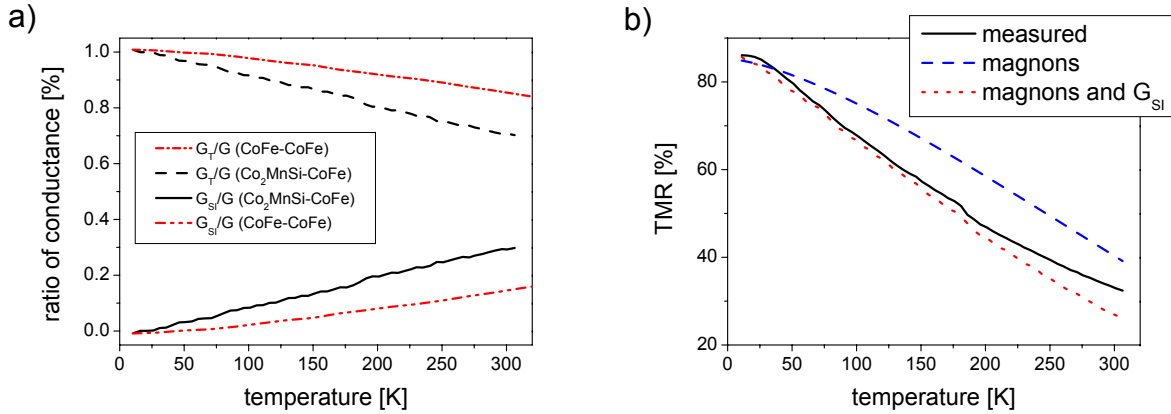


Figure 6.8: a) Ratios of participating tunnel currents demonstrate high part of spin independent tunnel current G_{SI} at room temperature; b) comparison with experimental data reveals necessity for spin independent tunnel current

extracted by use of equation (6.9). Assuming a spin stiffness of $7.6 \times 10^{-6} \text{ K}^{\frac{3}{2}}$ for $\text{Co}_{70}\text{Fe}_{30}$ the value for Co_2MnSi thin films can be fitted. For the range of $50\text{-}80 \times 10^{-6} \text{ K}^{\frac{3}{2}}$ the resulting ΔG vs. T curves are displayed in Fig. 6.7 b). Best agreement is achieved for $70 \times 10^{-6} \text{ K}^{\frac{3}{2}}$ that is higher than the previously discussed range of $7.6\text{-}50 \times 10^{-6} \text{ K}^{\frac{3}{2}}$. However, to estimate the possible range, it has been assumed that the Curie temperature of Co_2MnSi is between the ones of Py and $\text{Co}_{70}\text{Fe}_{30}$. The determined higher spin stiffness value points to a lower Curie temperature for Co_2MnSi thin films than for Py films.

In conclusion, the temperature dependence of ΔG can be attributed to two contributions. The first one is the temperature dependence of G_T , which is mainly affected by the barrier parameters thickness and height. The spin wave excitation (magnons) within the ferromagnetic electrodes, affected by the Curie temperature, is the second contribution. However, these considerations cannot clear up the strong temperature dependence of TMR effect amplitude for the $\text{Co}_2\text{MnSi}/\text{AlO}_x/\text{Co}_{70}\text{Fe}_{30}$ MTJ. If the already determined contributions are considered, the temperature dependence of TMR effect amplitude is that of the dashed blue line in Fig. 6.8 b). The temperature dependence is not that strong and the slope of the curve is opposite to the measured ones (black solid line). This discrepancy can be cleared up by taking into account the unpolarized tunnel current G_{SI} . By use of equation (6.10) the unpolarized part can be extracted from the experimental data. The relative ratios $\frac{G_{SI}}{G_{SI}+G_T}$ and $\frac{G_T}{G_{SI}+G_T}$ do not display the real contributions to the total tunnel current, but clearly reveals the difference in the temperature dependence between $\text{Co}_2\text{MnSi}/\text{AlO}_x/\text{Co}_{70}\text{Fe}_{30}$ and $\text{Co}_{70}\text{Fe}_{30}/\text{AlO}_x/\text{Co}_{50}\text{Fe}_{50}$ MTJs. The high ratio of spin unpolarized tunnel current G_{SI} in the $\text{Co}_2\text{MnSi}/\text{AlO}_x/\text{Co}_{70}\text{Fe}_{30}$ MTJ becomes the reason for the stronger temperature dependence with respect to the $\text{Co}_{70}\text{Fe}_{30}/\text{AlO}_x/\text{Co}_{50}\text{Fe}_{50}$ MTJ. Instead of 20 % in the $\text{Co}_{70}\text{Fe}_{30}/\text{AlO}_x/\text{Co}_{50}\text{Fe}_{50}$ MTJ the doubled ratio of 40 % is unpolarized tunnel current. This drastically increasing unpolarized tunnel current reduces

the contribution of the spin polarized term $G_T(T) \left(1 + P_1(T)P_2(T) \cos \theta\right)$ in equation (6.5) and decreases the TMR effect amplitude as is clear from equation (6.8). The effect on the temperature dependence of the TMR amplitude can be seen by the red dotted curve in Fig. 6.8 b). The slope changes and the temperature dependence is more drastic.

Now the strong temperature dependence of $\text{Co}_2\text{MnSi}/\text{AlO}_x/\text{Co}_{70}\text{Fe}_{30}$ MTJs has been deduced to the strongly increasing spin unpolarized tunnel current. However, the origin for this increasing unpolarized tunnel current cannot be determined by this model. But it seems to coincide with the high area resistance and the change in barrier asymmetry with respect to the $\text{Co}_{70}\text{Fe}_{30}/\text{AlO}_x/\text{Co}_{50}\text{Fe}_{50}$ reference MTJ. It is believed that the unpolarized tunnel current can be assigned to the step-like barrier in the $\text{Co}_2\text{MnSi}/\text{AlO}_x/\text{Co}_{70}\text{Fe}_{30}$ MTJ. To clear up on atomic scale, in the following paragraph the barrier quality is studied by AES and XAS/XMCD.

Finally, as consequence of the strong influence of the unpolarized tunnel current on the TMR temperature dependence, the investigation of the TMR effect amplitude demands for carefully controlling the temperature dependence of each single MTJ. Only a nearly same temperature dependence can ensure that the TMR effect amplitude and the corresponding spin polarization are comparable.

6.1.2 Quality of the interface II - atomic distribution

The previous interpretations based on magnetoresistance and tunneling characteristics suggest a step-like barrier. To elaborate this finding, microstructural characterization has been performed. Firstly, Auger Electron Spectroscopy (AES) combined with an ion etching techniques aiming for the stoichiometry of the Heusler/barrier interface. Secondly, X-ray Absorption Spectroscopy (XAS) and X-ray Magnetic Circular Dichroism (XMCD) to uncover the magnetic behavior at the $\text{Co}_2\text{MnSi}/\text{AlO}_x$ interface.

Interface stoichiometry

Auger Electron Spectroscopy provides a very surface sensitive and element-specific technique [65]. It enables to get insights into the stoichiometric composition at the interface between the Heusler and the barrier. In order to benefit from the surface sensitivity of AES, the samples to be investigated were prepared up to the oxidized AlO_x barrier only, and subsequently, post annealed at $\sim 450^\circ\text{C}$ for 40 minutes.

Since the determination of the absolute stoichiometry by AES is hard to reach, relative variations between differently prepared samples will be studied. To clear up the influence of plasma oxidation and thermal treatment, the following three samples have been prepared. Sample A is characterized by the complete oxidation and annealing process as denoted before. To separate the effect of annealing, sample B is only plasma oxidized. To further deduce on the effect of the plasma oxidation, sample C is prepared without oxidation. Then the layered stack is $\text{SiO}_2(100\text{ nm})//\text{V}42\text{ nm})/\text{Co}_2\text{MnSi}(100\text{ nm})/\text{Al}(1.4\text{ nm})$

| Composition | ΔG kcal/mole | Composition | ΔG kcal/mole |
|-------------------------|----------------------|---------------------------|----------------------|
| Al_2O_3 | -380 | Mn_2O_3 | -210 |
| CoO | -51 | Mn_3O_4 | -307 |
| Co_3O_4 | -185 | SiO_2 | -205 |
| MnO | -86 | MnSiO_3 | -297 |
| MnO_2 | -111 | Mn_2SiO_4 | -390 |

Table 6.2: Formation enthalpies for different composition of the present elements (after [110])

for sample C plus plasma oxidation at 275 W for 200 sec for sample B and plus annealing at $\sim 450^\circ\text{C}$ for 40 minutes for sample A.

Under consideration of the different information depth λ_x of the elements Co, Mn and Si [83] for sample A a stoichiometric composition of $\text{Co}_{34\pm 1}\text{Mn}_{41\pm 2}\text{Si}_{24\pm 1}$ has been determined. The composition of sample B reveals the effect of post annealing at $\sim 450^\circ\text{C}$ for 40 minutes. The determined stoichiometry of sample B is $\text{Co}_{36\pm 4}\text{Mn}_{43\pm 6}\text{Si}_{21\pm 2}$ in accordance with the annealed sample A. Therefore, the post annealing procedure does not significantly alter the atomic concentration. Hence, thermally induced segregation processes at the $\text{Co}_2\text{MnSi}/\text{AlO}_x$ interface are not very pronounced.

The atomic concentration at the $\text{Co}_2\text{MnSi}/\text{AlO}_x$ interface may also be influenced by the plasma oxidation process. For this purpose sample C provides information. The 1.4 nm thin Al layer protects the interface from oxygen, since the natural oxide layer is restricted to about 1 nm [84]. The reference concentration of sample C is determined to be $\text{Co}_{47}\text{Mn}_{36}\text{Si}_{17}$. This is different from the ideal bulk composition of Co_2MnSi . However, the quantification by AES is based on reference data of single element samples, e.g. Co, Mn and Si. This aspect makes the composition of sample C the ideal one for AES experiments. The comparison with data of the plasma oxidized samples A and B reveals a Mn and Si segregation to the $\text{Co}_2\text{MnSi}/\text{AlO}_x$ interface. The driving force during plasma oxidation may be the formation of binary alloys MnO_x and SiO_y or the ternary composition Mn_2SiO_4 as can be seen in Tab. 6.2. However, plasma oxidation is not a process in thermodynamic equilibrium and, hence, the present kinetic situation has to be taken into account. Consequently, the formation enthalpies of Tab. 6.2 can only serve as indications.

To roughly estimate the thickness of this MnSi_xO_y segregation layer, sample A and a sample with insertion of a 6 nm Co interlayer between Co_2MnSi and AlO_x are investigated with respect to depth profiling. The Co insertion prevents the formation of the MnSi_xO_y segregation layer, but ensures complete oxidation of the 1.4 nm Al layer by plasma oxidation to form 1.8 nm of AlO_x . The thickness of the insulating barrier is estimated from the sputtering time to remove the oxidized surface layers. This time is assumed to be proportional to the layer thickness. The sputtering time for sample A is $\frac{1}{3}$ larger than for the Co inserted sample. Therefore, the insulating barrier of sample A is about

$\frac{1}{3} \cdot 1.8 \text{ nm} = 0.6 \text{ nm}$ thicker. This increased barrier thickness of 0.6 nm is in good agreement with the additional barrier thickness estimated from electrical investigations of 0.5 nm. If the presence of the 0.5-0.6 nm MnSi_xO_y segregation layer can clear up the electrical discrepancy between the $\text{Co}_2\text{MnSi}/\text{AlO}_x/\text{Co}_{70}\text{Fe}_{30}$ and the $\text{Co}_{70}\text{Fe}_{30}/\text{AlO}_x/\text{Co}_{50}\text{Fe}_{50}$ MTJ, then the discrepancy of the temperature dependence may also be dissolved. Therefore, a complete $\text{Co}_2\text{MnSi}/\text{AlO}_x/\text{Co}_{70}\text{Fe}_{30}$ tunnel junction has been prepared as usual, but with a 6 nm Co intercalation layer between Co_2MnSi and AlO_x . From the single layer investigation it is known that the Mn/Si segregation layer is prevented. As result the temperature dependence also reduces to a low dependence as present in the $\text{Co}_{70}\text{Fe}_{30}/\text{AlO}_x/\text{Co}_{50}\text{Fe}_{50}$ MTJ as can be seen by blue curve in Fig. 6.6 a) and as additional confirmation the area resistance and barrier asymmetry are similar to the ones of the $\text{Co}_{70}\text{Fe}_{30}/\text{AlO}_x/\text{Co}_{50}\text{Fe}_{50}$ reference MTJ.

In conclusion, the formation of a 0.5-0.6 nm MnSi_xO_y segregation layer is responsible for the high area resistance, the change in barrier asymmetry and the strong temperature dependence with respect to the $\text{Co}_{70}\text{Fe}_{30}/\text{AlO}_x/\text{Co}_{50}\text{Fe}_{50}$ MTJ. These aspects make the picture of a step-like barrier shape as in Fig. 6.5 the most realistic one.

Surface magnetism

The spin polarization at the interface is the essential factor for achieving a high TMR amplitude because the tunneling process is sensitive to the first monolayers only [76, 77]. Due to the strong correlation of spin polarization and magnetism, the magnetic characterization of the $\text{Co}_2\text{MnSi}/\text{AlO}_x$ interface may supply additional information on factors limiting the spin polarization.

For this purpose the samples of type A, B and C, as described in the previous AES paragraph, will be studied, where the sample A is added by samples of same preparation procedure but with different Co_2MnSi layer thicknesses, e.g. 4, 8, 15 and 61 nm. As already mentioned in the previous paragraph, the natively oxidized Al cap layer in sample C prevents oxidation of the Co_2MnSi surface. The according XAS spectrum of Co is characterized by structureless $L_{2,3}$ absorption edges, as can be seen in Fig. 6.9 a). This is typical for Co with delocalized 3d electrons [83], e.g. metallic Co, but the resonance lines are significantly wider than for pure Co [129].

In contrast, the XAS spectrum of type A samples shows an additional shoulder at $\sim 4 \text{ eV}$ above the maxima of $L_{2,3}$ peaks. However, this absorption shape is neither compatible with pure metallic Co nor with the typical multiplett structure of CoO [129]. Hence, there is no indication of CoO at the $\text{Co}_2\text{MnSi}/\text{AlO}_x$ interface for samples of type A as well as of type B. This is in agreement with AES characterization of the $\text{Co}_2\text{MnSi}/\text{AlO}_x$ interface indicating Mn/Si segregation towards the interface but no Co diffusion.

All type A samples show the additional shoulder at $\sim 4 \text{ eV}$ above the maxima except the thinnest A sample of 4 nm thickness and the not annealed type B sample. These are exactly the samples which have not shown a magnetic moment in magnetometric measurements, as have been discussed in paragraph 4.4.2. Therefore, this 4 eV shoulder can be attributed

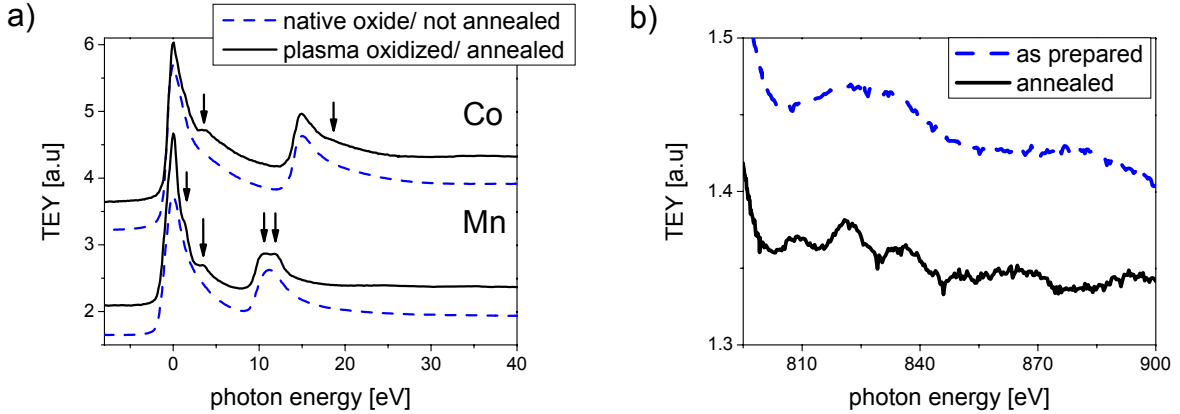


Figure 6.9: a) XAS measurements for type A and C samples in total electron yield (TEY) detection (the photon energy is defined with respect to the maximum of the L_3 absorption edge); b) EXFAS signal for samples A (4 nm, 61 nm and 100 nm Co_2MnSi thickness) and sample C at the Co $L_{2,3}$ edges

to a certain atomic and magnetic order of the Co_2MnSi at the interface to the AlO_x barrier.

For the Mn atoms the situation is quite different. The type C sample reveals a structureless $L_{2,3}$ absorption edge, as can be seen in Fig. 6.9 a), directing to metallic Mn [130]. In contrast, the plasma oxidized samples of type A and B exhibit a multiplett structure, as indicated by the tips in Fig. 6.9 a). This multiplett feature is independent of Co_2MnSi thickness and application of annealing and points to localized 3d electrons [83]. Altogether, this line shape can be attributed to oxidized Mn cation [83]. This is in good agreement with the AES studies establishing a MnSi_xO_y segregation layer. The MnO_x multiplett structure is usually sharper⁴. However, this can be understood by superposition of the multiplett structure of MnO_x and the underlying not oxidized Mn, since the previously determined layer thickness of 0.5-0.6 nm is much smaller than the information depth of $\sim 0.1 \mu\text{m}$ [74] in XAS experiments.

For Si the XAS spectrum reveals a typical SiO_2 absorption shape and additionally confirms the MnSi_xO_y segregation layer from AES experiments.

An additional feature between in bulk magnetic and non-magnetic samples can be observed in their extended x-ray absorption fine structure (EXFAS) in Fig. 6.9 b). For the annealed type A samples with thicknesses greater than 4 nm, a short period oscillation as a function of photon energy is revealed. In contrast, for the not annealed sample B and the too thin 4 nm sample of type A the oscillation period is much longer. This indicates that the atomic interface order is quite different for macroscopic non-magnetic and magnetic samples.

⁴The less sharp MnO_x multiplett for the samples discussed in this work is not a result of a limited energy resolution in XAS.

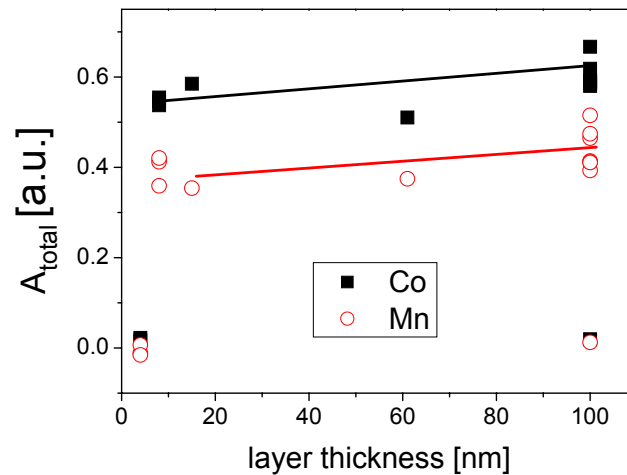


Figure 6.10: Relative XMCD signal A_{total} vs. Co_2MnSi layer thickness for samples of type A and as reference of type B

Till now the magnetic moments have only been characterized as a bulk parameter of the complete unit cell. Now the element-specific magnetic moment at the $\text{Co}_2\text{MnSi}/\text{AlO}_x$ interface can be evaluated. The calculation of the exact element-specific moment is based on some assumptions and is completely described in citesch04. Therefore, here the relative XMCD signal A_{total} , as defined in [83], is discussed. This is proportional to the magnetic moment.

As one first result the XMCD asymmetry defined by the difference of the two XAS signals exhibits the same sign for Co and Mn indicating parallelly aligned magnetic moments.

The evaluation of the relative XMCD signal reveals the influence of annealing on the surface magnetism. The samples of type A with thickness from 8 nm up to 100 nm show a non-vanishing magnetic moment of Co and Mn, while for the 4 nm sample and the not annealed sample of type B exhibit no detectable relative XMCD signal for both elements. This is in good agreement with the magnetometric characterization of layer thickness dependence in paragraph 4.4.2 and the discussion in terms of the 4 eV shoulder.

For the ratio of the relative XMCD signal of Co and Mn and therefore of the magnetic moments $\frac{m_{\text{Mn}}}{m_{\text{Co}}}$, a value of 1.5-2.2 has been estimated. From band structure calculations a magnetic moment ratio of ~ 2.9 is expected [14]. The reduced experimentally determined ratio is reasonable because of MnO_x formation and local disorder both be apparent in the segregation layer.

6.1.3 Co-termination at the interface

Suppressing the formation of the Mn/Si segregation layer at the $\text{Co}_2\text{MnSi}/\text{AlO}_x$ interface is the way to go so as to enhance the magnetic tunnel junction characteristics leading to

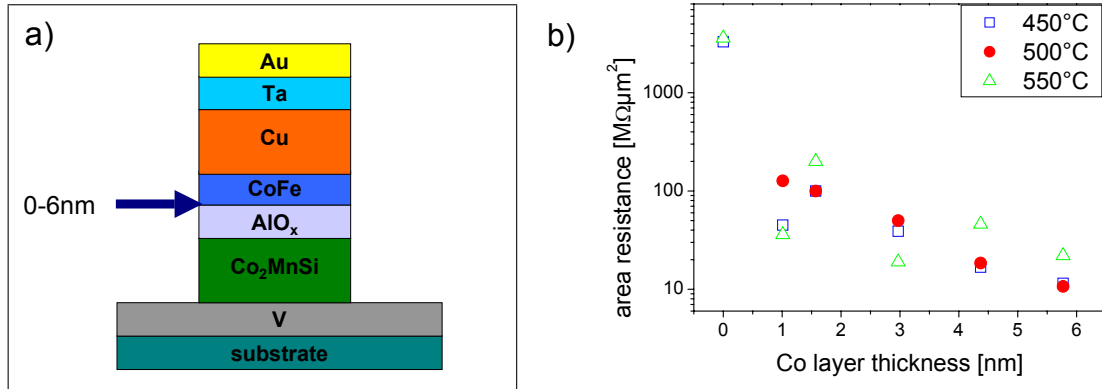


Figure 6.11: a) Assembly of Co-termination stack: between Co_2MnSi and AlO_x barrier a 0-6 nm thin cobalt interlayer is inserted; b) area resistance RA in dependence of Co intercalation layer thickness

higher TMR amplitudes. In order to maintain the overall stoichiometry of the Heusler alloy interface region on the one hand, the intercalation of a thin Co layer at the $\text{Co}_2\text{MnSi}/\text{AlO}_x$ interface is the only possibility to prevent from segregation Mn- and Si atoms at this interface. On the other hand theoretical band structure calculations conclude a loss of half metallic character induced by a cobalt terminated interface [42]. Consequently, the influence of a variable Co intercalation layer on the MTJ characteristics is both of fundamental as well as of application directed interest. Here the Co intercalation layer in the MTJ was varied up to 6 nm, see Fig. 6.11 a), and compared to a reference MTJ without it but identically made. These investigations have been done on a simplified layer stack. As can be seen Fig. 6.11 a), the antiferromagnet MnIr is absent. Thus, the pinning of the upper $\text{Co}_{70}\text{Fe}_{30}$ electrode is not present and the switching behavior becomes more disadvantageous. As consequence of the worse switching behavior the resulting TMR effect amplitude is reduced. However, this simpler stack setup can stop the layer deposition process after the $\text{Co}_{70}\text{Fe}_{30}$ layer to prepare an ex-situ annealing procedure. Concerning the ex-situ annealing procedure with respect to the in-situ annealing one after the AlO_x formation it provides the possibility to apply temperatures up to 550°C for several hours and an external field. This more variability may be useful to assist interdiffusion processes between the Co_2MnSi and the Co layer. The applied annealing procedure consists of annealing at 450, 500 or 550°C for 70 minutes.

The expected suppressing of the Mn and Si enriched interfacial layer by the intercalating thin Co layers can be proven measuring the corresponding area resistance RA , which is presented in Fig. 6.11 b), decreases starting from 10-20 $\text{G}\Omega\mu\text{m}^2$ for the reference sample without Co to a value of 10-20 $\text{M}\Omega\mu\text{m}^2$ with a 6 nm thick Co intercalation layer.

The corresponding evolution of the TMR effect amplitude is quite different. The reference MTJ without a Co intercalation layer exhibits a TMR amplitude between 15% and 15% slightly depending on the annealing temperature. For a 1 nm thick Co layer

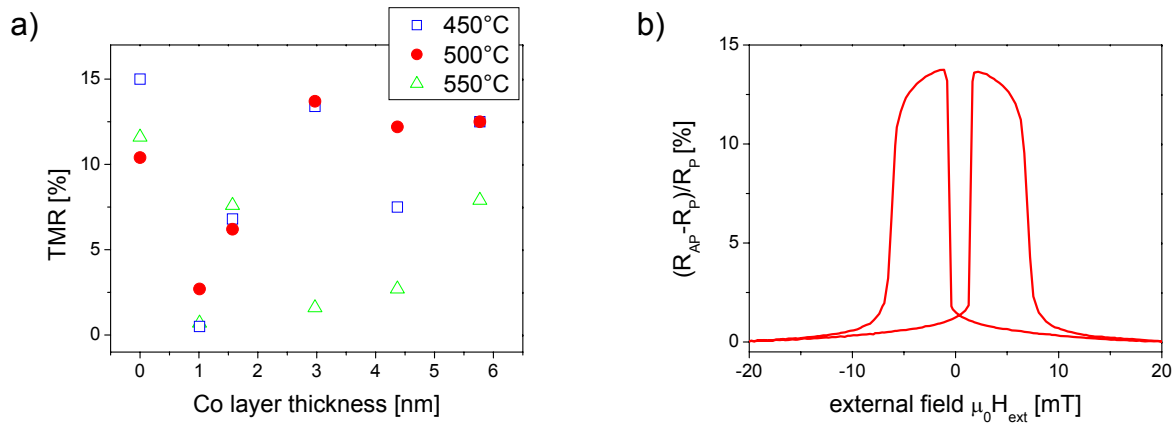


Figure 6.12: a) TMR amplitudes for variation of Co-interlayer thickness and b) corresponding magnetoresistance loop (here: 3 nm of Co interlayer)

the TMR drops down under 3% effect amplitude to again increase up to 12-13% for Co intercalation layers of 3-6 nm in thickness except for the 550°C annealed samples. To ensure that this behavior is not induced by a different switching behavior for the different Co layer thicknesses, the coercive fields have been cautiously monitored. The coercivities of $\text{Co}_2\text{MnSi}/\text{Co}_{x\text{nm}}$ electrode are in the range of 1-2 mT independently of Co layer thickness and for the $\text{Co}_{70}\text{Fe}_{30}$ one in the range of 5-6 mT as can be seen in a typical TMR loop in Fig. 6.12 b). Hence, this well defined switching behavior for all Co layer thicknesses allows to compare the pure TMR effect amplitudes.

The dependence of TMR effect amplitude from the Co intercalation layer thickness can be understood as follows. Without the Co layer the reference MTJ reveals a moderate TMR effect amplitude in comparison to the standard Co_2MnSi containing MTJ due to the worse switching behavior caused by the absent of the antiferromagnet MnIr. However, the area resistance fits very well with the standard MTJ value. If then a Co layer of 1-1.5 nm thickness is inserted, the TMR drops. From point of the phase diagram in Fig. 2.1 the Co concentration can vary in the range of 45-55% to conserve the $L2_1$ structure. The 1-1.5 nm thin Co layer provides only a ratio of about 2% of the total 100 nm Co_2MnSi volume. However, in the $\text{Co}_2\text{MnSi}/\text{AlO}_x$ interface region the Co concentration can locally be much higher to destroy the $L2_1$ structure. But even in case of very small deviations from optimal Co concentration (<5%), the spin polarization can break down due to antisite disorder effects. By the great amount of Co atoms at the $\text{Co}_2\text{MnSi}/\text{AlO}_x$ interface, the probability for antisite disorder effects with Mn and Si sites becomes higher. An extra peak in the gap of the spin down electrodes is the consequence of Co-Mn and Co-Si disorder [41]. Additionally, even in case of perfect stoichiometry and perfect local order, the Co terminated surface of the Co_2MnSi unit cell is predicted to be not half metallic [42].

The subsequent increase up to 12-13% of TMR effect amplitude for the 3-6 nm thick

intercalation layers can be deduced to the presence of a closed Co layer providing the spin polarization to the TMR effect. This Co layer is stable up 500°C , where for 550°C annealing the intermixing between Co_2MnSi and Co becomes significant to form again a Co enriched interface region with same consequences as described before.

In conclusion, the Co intercalation has successfully been introduced to prevent the Mn and Si segregation towards the $\text{Co}_2\text{MnSi}/\text{AlO}_x$ interface, as has already been indicated by the AES experiments. However, the extra Co atoms locally destroy the highly spin polarized character of Co_2MnSi or form a closed Co layer at temperatures $\leq 500^\circ\text{C}$ with Co-like spin polarization.

6.2 Spin polarization and local ordering

In literature [12, 63, 7] the influence of local ordering on the spin polarization is discussed. Only perfectly locally ordered Co_2MnSi films provide the theoretically predicted 100% spin polarization [3]. Therefore, the local order has to be monitored, when investigating the spin polarization. However, the local ordering can only be studied as a function of the volume, where the spin polarization determination probes the first few monolayer of Co_2MnSi . Therefore, before the bulk local ordering can be related to the spin polarization, the dependence of spin polarization from bulk characteristics has to be studied. Since the spin polarization and saturation magnetization are assumed to be strongly correlated, the magnetization may serve as bulk parameter and, therefore will be characterized, firstly.

To check the correlation between spin polarization and magnetism for Co_2MnSi , the spin polarization determined at 10 K is related to the corresponding saturation magnetization at room temperature. As can be seen in Fig. 6.13, spin polarization and saturation magnetization are indeed strongly correlated⁵. At low saturation magnetization values of $\sim 800 \text{ kA/m}$ a spin polarization of under 30% is present, while the maximum magnetization coincides with the maximum spin polarization of 61%. This behavior confirms the assumed strong correlation between spin polarization as a surface sensitive parameter and saturation magnetization as a volume sensitive one for Co_2MnSi . A drop of saturation magnetization by only 10% has as consequence a strong reduction of spin polarization by $\frac{1}{4}$. Therefore, the local ordering investigation concerning the bulk volume can be related to the surface sensitive spin polarization at the $\text{Co}_2\text{MnSi}/\text{AlO}_x$ interface.

But before the discussion comes to the detailed analysis of the local ordering, the more macroscopic microstructure and its influence on the spin polarization will be regarded.

As has been mentioned in chapter 4, the grain size of Co_2MnSi layers depends on their thickness. Thinner films of about 15 nm thickness have shown grain sizes in the range of 50-100 nm, where for the 100 nm thick Co_2MnSi film larger grains of 200-400 nm have

⁵As can be seen in this graph as well as in the following ones, the conclusions on the local disorder processes can only be extracted from very few samples. Thus, to be completely convinced by these correlations, the number of investigated samples has to be increased in the future.

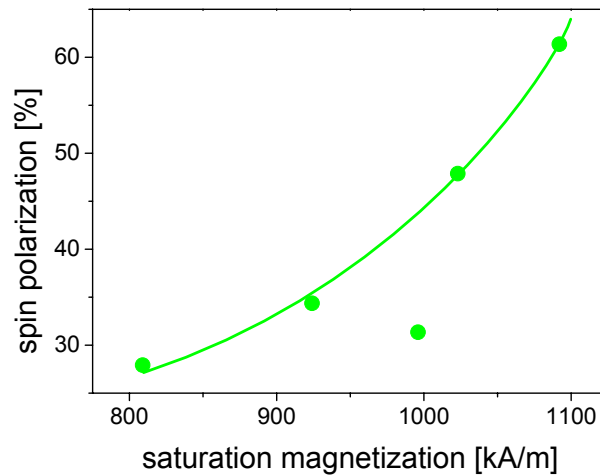


Figure 6.13: Spin polarization determined at 10 K and at 10 mV bias voltage vs. saturation magnetization: maximum spin polarization coincides with maximum saturation magnetization; the data is taken from MTJs containing polycrystalline Co_2MnSi films except the point at 61 % spin polarization, which belongs to a (110) textured Co_2MnSi electrode

been identified. Consequently, the question arises if this variation in grain size also has an influence on the spin polarization. The magnetoresistive measurements of the corresponding magnetic tunnel junctions reveal a clear dependence of spin polarization from film thickness. The TMR amplitude decreases from 33% measured at room temperature for the 100 nm thick sample to 13% for the film of 20 nm thickness, as can be extracted from Fig. 6.14. This drop of TMR effect amplitude and correspondingly of the spin polarization can be attributed to two effects. Firstly, the thickness dependence of the bulk magnetization as well as the surface magnetism reveal a decrease of $\sim 10\%$ of magnetic moment, when decreasing the film thickness from 100 nm to 8 nm. Then this drop of 10% has as consequence a drastic reduction of spin polarization by $\frac{1}{4}$, as has been shown on Fig. 6.13. Secondly, the decreasing grain size emphasizes the influence of grain boundaries in the Co_2MnSi films. Grain boundaries can provide centers for non-stoichiometric segregations [65] and this may reduce the measured spin polarization by extra unpolarized tunnel currents.

In summary, the film thickness strongly influences the spin polarization of Co_2MnSi thin films by affecting the grain size and the magnetism. However, even in case of constant film thicknesses the spin polarization varies as has been seen in Fig. 6.13 for 100 nm films. To clear up this variation the detailed atomic structure will be studied.

Firstly, the lattice constant accessible by the peak angle position give information on local ordering, as has been confirmed on magnetism of the single Co_2MnSi films in paragraph 4.3. Consequently, the evolution of TMR amplitude with lattice constant is investigated. The experimental data reveal a strong correlation, as can be seen Fig. 6.16

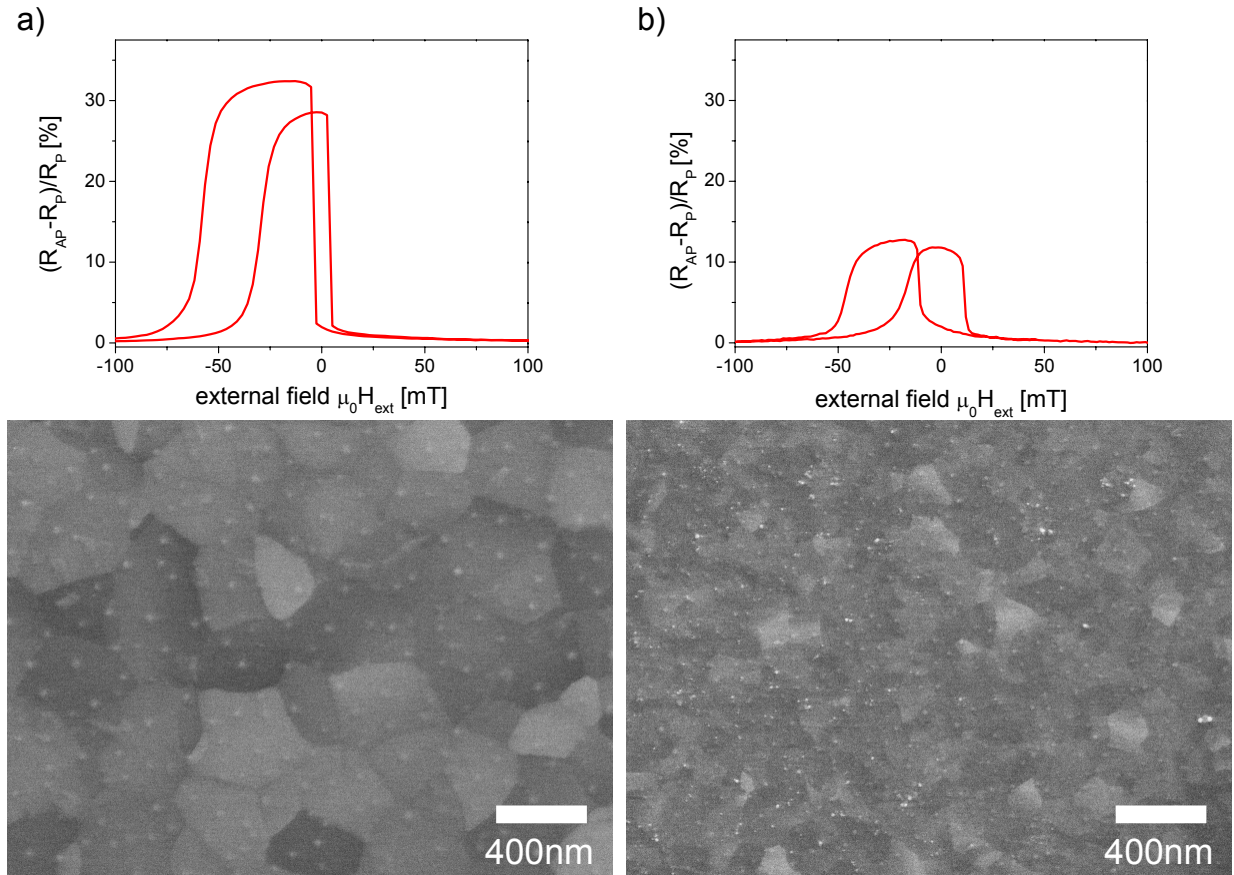


Figure 6.14: Magnetoresistance for magnetic tunnel junction containing a) a 100 nm and b) a 25 nm thin Co_2MnSi electrode; bottom pictures show the corresponding surface morphology of textured $\text{V}(42\text{ nm})/\text{Co}_2\text{MnSi}(100\text{ nm})/\text{AlO}_x(1.8\text{ nm})$ stacks revealing the different grain sizes

a). The more well ordered samples with small lattice constant exhibit the highest TMR effect amplitude in accordance with the conclusions on the electrical resistance and the saturation magnetization in paragraphs 4.1.1 and 4.1.2 and in agreement with theoretical investigations, which predict a reduction of the energy gap with increasing lattice constant [29]. The comparability of the room temperature TMR effect amplitude is ensured by the fact that all investigated samples exhibit the same characteristic temperature dependence ⁶.

Now to be able to get insight into the exact local ordering processes, the relative peak intensities have to be analyzed. Due to best signal-to-noise ratio, the intensities of the peaks (200) and (111) are studied. The disorder process responsible for the reduction of

⁶This same temperature dependence was confirmed directly by TMR vs. T measurements for the elevated samples.

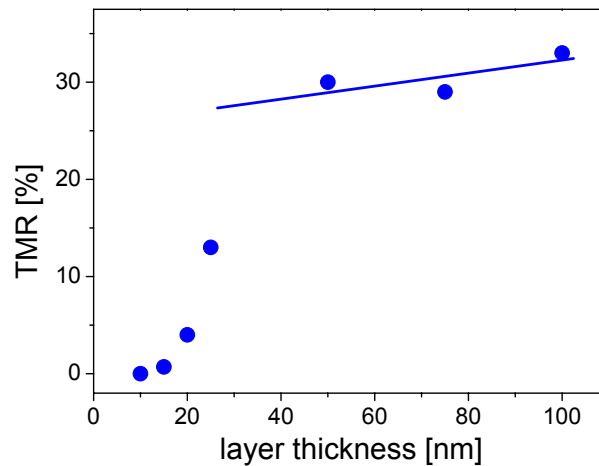


Figure 6.15: TMR effect amplitude in dependence of (110) textured Co_2MnSi layer thickness showing a rapid decrease at about 30 nm

the spin polarization is best seen when plotting the individual peak intensities against the effect TMR amplitude, as done Fig. 6.16 b). Up to high TMR amplitude values the relative peak intensity of the (200) peak increases, where the ones of the (111) decreases. Under assumption that samples with higher spin polarization are better ordered, the evolution of the peak intensities with TMR amplitude in comparison to the calculated evolution with order parameter in Fig. 1.6 lets conclude only one disorder type. The Co-Mn disorder process is responsible for the reduced spin polarization. Only the two types Co-Mn and Co-Mn-Co reveal a decreasing (111) intensity and an increasing (200) intensity with increasing degree of order. This is the same disorder process responsible for the reduction in saturation magnetization discussed in chapter 4. And also the favor for this disorder type can be deduced to the nearly same atomic radii [7] and its similar electronic configuration of the elements cobalt and manganese [7, 12].

To quantify the degree of Co-Mn disorder, the relative peak intensities have to be studied with respect to a reference. The calculated data in Tab. A.3 serves as this reference. If the measured peak intensities are normalized to the corresponding calculated ones, the degree of disorder can directly be extracted from Fig. 1.6 in paragraph 1.2.3. For the (111) peak the ratio of measured to calculated peak intensity was determined to be 1.3, where for the (200) the factors is 0.5. For both, a disorder parameter of $\alpha_{\text{Co-Mn}} \sim 0.6-0.7$ is determined. This high degree of disorder seems to be unrealistic due to the measured high spin polarization. In contrast, by experiments in other groups a spin polarization of 50-60% corresponds to disorder of 18% [63]. This makes clear the necessity for a perfect ordered Co_2MnSi reference sample to experimentally determine the relative peak intensities by the used XRD machine. Only such a procedure includes all instrumental deviations from calculated intensities.

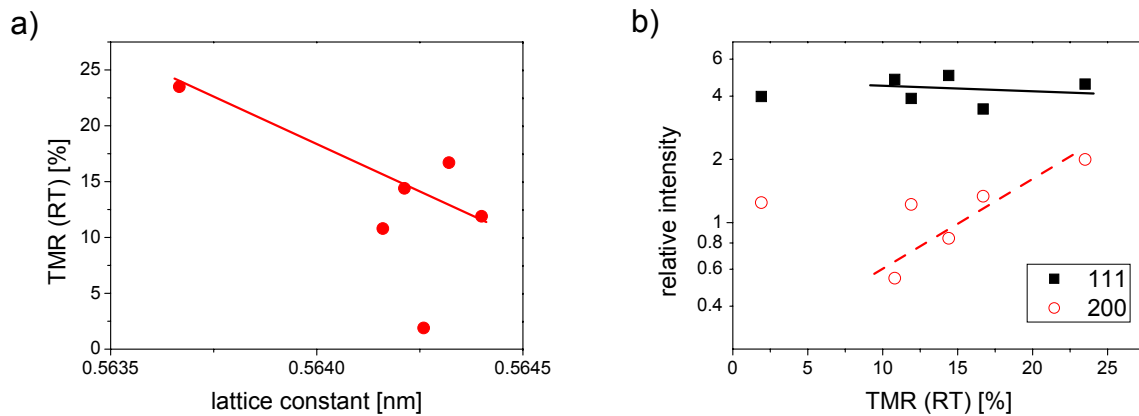


Figure 6.16: a) TMR amplitude at room temperature vs. lattice constant of Co_2MnSi demonstrates that high spin polarization corresponds to smallest unit cells; b) influence of local ordering on spin polarization: decreasing (111) intensity and increasing (200) intensity with increasing TMR effect amplitude; both graphs have been extracted from data taken on polycrystalline Co_2MnSi 100 nm films integrated in MTJs

To summarize, it could be demonstrated that not only the film thickness influence the grain size within the Co_2MnSi thin films, but also the TMR effect amplitude. This has been deduced to the decreasing grain size and /or to a higher sensitivity of spin polarization with respect to local ordering than for the nearly unchanged magnetism. This sensible correlation between spin polarization and magnetism has been experimentally demonstrated. The analysis of the relative peak intensities reveals the Co-Mn and Co-Mn-Co disorder as main type for the reduction in spin polarization. This type of disorder and its sensitive influence on the spin polarization is in good agreement with other experimental investigations [63, 12].

Chapter 7

IETS - Inelastic electron tunneling spectroscopy

Inelastic electron tunneling spectroscopy (IETS) is a physical technique, which provides information about solid state excitation and impurities within the AlO_x barrier and at the interfaces. In principle, these additional information is included in the already taken I - V - or G - V -characteristics. However, extra experimental efforts are necessary to extract this data. Therefore, the first paragraph will describe the experimental setup, before afterwards the experimental results will be discussed.

The tunneling electron can interact with solid state excitations as phonon, plasmons or magnons and with impurities situated within the barrier or at its interfaces [66]. If such an assisted tunneling is inelastic, the tunnel current will vary slightly. The detection of such a variation is revealed by $\frac{d^2I}{dV^2}$ - V curves.

7.1 Experimental aspects

IET spectra ($=\frac{d^2I}{dV^2}$) reveal small deviation from the characteristic current-voltage behavior of tunnel junctions. To detect these small deviations, the IET spectra have been taken by Lock-In technique with an ac voltage modulation amplitude of 5 mV in accordance to investigations of other groups [131, 132, 133, 134, 135]. The bias voltage is varied from -400 mV to +400 mV, where it is defined with respect to the potential of the lower electrode. Thus, at positive bias voltage the electrons tunnel from the lower into the upper electrode. In order to reduce thermal smearing of order $4k_B T$ [136], the $\frac{d^2I}{dV^2}$ - V characteristics are taken at 20 K. This determines the thermal restriction to the resolution to be ~ 7 meV.

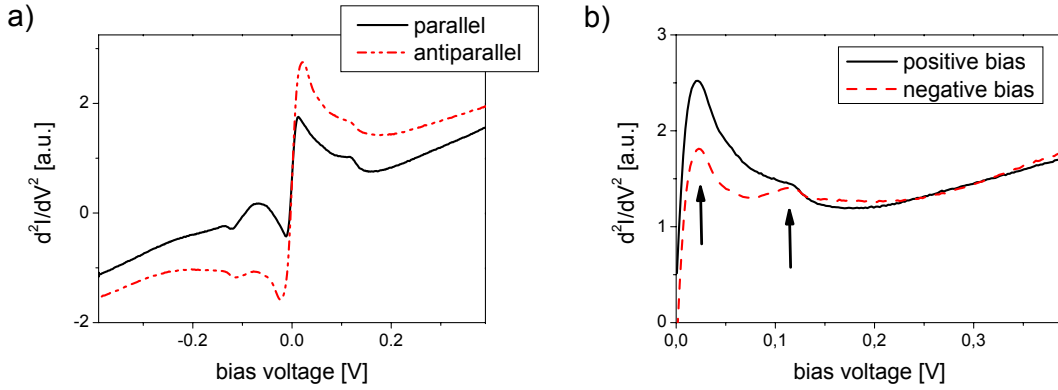


Figure 7.1: a) IET spectrum for parallel and antiparallel magnetic configuration; b) dependence from bias voltage polarity; both for the reference $\text{Co}_{70}\text{Fe}_{30}/\text{AlO}_x/\text{Py}$ magnetic tunnel junction

7.2 Results

The electrical and temperature dependent investigation as well as the AES and XAS analysis propose that the main reason for the large temperature and bias voltage dependence is the presence of the MnSi_xO_y segregation layer at the $\text{Co}_2\text{MnSi}/\text{AlO}_x$ interface formed during the plasma oxidation process. More information about the influence of this MnSi_xO_y segregation layer on the tunneling process can be achieved by IETS.

Therefore, in the following, the discussion is concentrated on two systems. Firstly, the magnetic tunnel junction consisting of $\text{Co}_2\text{MnSi}/\text{AlO}_x/\text{Co}_{70}\text{Fe}_{30}$ as active layers and secondly, as reference a sample of $\text{Co}_{70}\text{Fe}_{30}/\text{AlO}_x/\text{Py}$ have been characterized by IETS. The reference MTJ exhibits smaller temperature and bias voltage dependencies, which additionally to its very high TMR amplitude at room temperature make them a *perfect oxidized reference*¹.

Starting with this reference sample one is able to study the fundamental features of IET spectra of magnetic tunnel junctions with AlO_x as barrier.

The 2nd derivate of current-voltage characteristic of the $\text{Co}_{70}\text{Fe}_{30}/\text{AlO}_x/\text{Py}$ reference MTJ is presented Fig. 7.1 a), where the antiparallel and parallel alignment is defined with respect to the relative orientations of the magnetic electrodes.

Three features are remarkable. Firstly, the IET spectrum exhibits a larger signal for the antiparallel configuration. Secondly, in both magnetic configurations and in both directions of bias voltage at about 115 meV a peak is present. This peak has been found in several other investigation using AlO_x as barrier material [73, 135, 133] and is attributed to an AlO stretching mode [66]. And thirdly, two peaks are present at -10 mV and +10 mV, which can be interpreted as energy with maximum probability for magnon excitations [137]. The corresponding peak is higher for positive bias voltage, as can be

¹By AES depth profile measurements no intermixing of the magnetic electrodes with the AlO_x barrier is detectable.

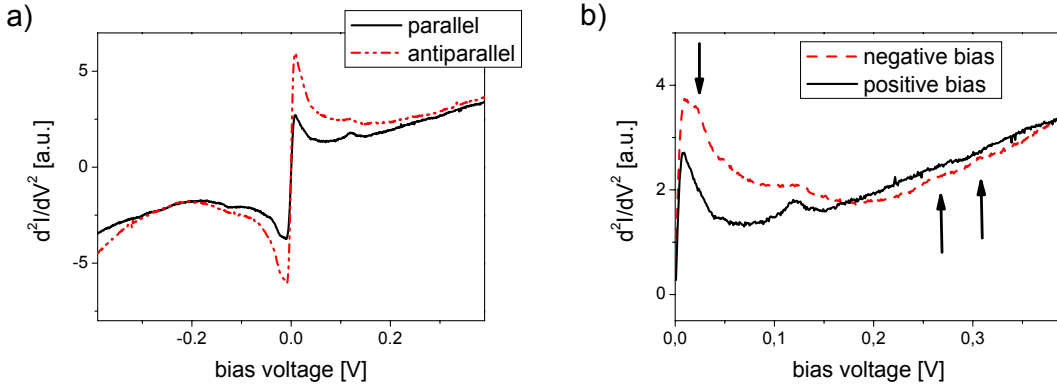


Figure 7.2: a) $\frac{d^2I}{dV^2}$ vs. applied bias voltage V for parallel and antiparallel magnetic configuration; b) dependence from bias voltage polarity in parallel magnetic alignment; both for the $\text{Co}_2\text{MnSi}/\text{AlO}_x/\text{Co}_{70}\text{Fe}_{30}$ magnetic tunnel junction

seen in Fig. 7.1 b). This is the case when the electrons tunnel from the high Curie temperature $\text{Co}_{70}\text{Fe}_{30}$ into the low Curie temperature Py.

If now the MTJ with Co_2MnSi as lower electrode is regarded, these features can also be found. At about 115 mV again the AlO phonon excitation is present for both magnetic configurations and for both bias voltage polarities, as is shown in Fig. 7.2 a). At -9 mV and 8 mV the same magnon excited peaks are present now with higher intensity at negative bias voltage, which represents the case of tunneling from the high Curie temperature $\text{Co}_{70}\text{Fe}_{30}$ into the low Curie temperature Co_2MnSi . Thus, the previously remarked feature can also be found in the $\text{Co}_2\text{MnSi}/\text{AlO}_x/\text{Co}_{70}\text{Fe}_{30}$ MTJ.

Additionally, at -22 mV a shoulder is present, as is obvious in Fig. 7.2 b). It is only observed, when the electrons tunnel from $\text{Co}_{70}\text{Fe}_{30}$ into Co_2MnSi . Such an asymmetry is generally apparent, if the corresponding inelastic scattering process occurs only at one barrier interface and if the tunneling probability depends on the fact whether the inelastic scattering occurs after or before the barrier transmission [66]. Since the only difference between the $\text{Co}_2\text{MnSi}/\text{AlO}_x/\text{Co}_{70}\text{Fe}_{30}$ and the reference $\text{Co}_{70}\text{Fe}_{30}/\text{AlO}_x/\text{Py}$ MTJ is the constitution of the $\text{Co}_2\text{MnSi}/\text{AlO}_x$ interface with the MnSi_xO_y segregation layer, this inelastic scattering process is suggested to take place at this interface. Especially the localized Mn ions are recommended to play a dominant role.

Going to higher energies, two further peaks are present at -260 meV and -310 meV. Due to their excitation energy, these peaks can be attributed to phonon or molecule excitations [138]. The latter one can be due to presence of carbon hydrogen molecules established by the annealing after the AlO_x preparation in the vacuum. However, these molecules should be situated at the $\text{AlO}_x/\text{Co}_{70}\text{Fe}_{30}$ interface. But the two peaks are not present in the positive bias polarity. Hence, it seems to be more realistic that again the MnSi_xO_y segregation layer provides phonon excitations. Nevertheless, due to their high excitation energies, they play no dominant role at room temperature but are still *frozen* out.

Conclusion and outlook

”Is Co_2MnSi a promising candidate to replace the transition metals in sensor applications?” This was the question that arose at the very beginning of this work. ”And what is the realizable spin polarization in real thin films of Co_2MnSi ?” is the question that follows consequently after. Following these two main questions, the fundamental physical as well as applicational aspects have been investigated and discussed.

For the first time a very high TMR amplitude of over 95% could be realized in a magnetic tunnel junction consisting of one conventional electrode of $\text{Co}_{70}\text{Fe}_{30}$ and a Co_2MnSi Heusler alloys one. To reach this high TMR effect amplitude, the deposition and properties of single Co_2MnSi Heusler alloy films have been extensively studied. Polycrystalline and (110) textured thin films can be realized by magnetron sputtering with well defined microstructural ($a = 0.563\text{-}0.566\text{ nm}$), magnetic ($4.7\ \mu_B$) and electrical properties ($\rho(300\text{ K}) = 110\text{-}170\ \mu\Omega\text{ cm}$) independent of growth mode. These films exhibit nearly rectangular hysteresis loops with low coercivities of 1-2 mT and very low surface roughness of 0.2-0.6 nm. Both aspects are important for integration in magnetic tunnel junctions (MTJ).

The Co_2MnSi film layer thickness seems to play neither a dominant role for the magnetism in bulk nor at the $\text{Co}_2\text{MnSi}/\text{AlO}_x$ interface, as has been checked down to a layer thickness of 6 nm. Only for thinner films the magnetism is vanishing.

Polycrystalline samples can be prepared by deposition on heated substrate, where the choice of substrate is of no fundamental aspect. The substrate temperature has to be in the range of 300-600 °C. Alternatively, polycrystallinity can be achieved by deposition onto SiO_2 (100 nm) at room temperature and post annealing for 70 minutes at 450-550 °C. In contrast, the (110) textured films need a 42 nm thick vanadium layer as seed, which itself is (110) textured. The room temperature deposition is again followed by post annealing at temperatures between 200 °C and 600 °C.

The realization of the polycrystalline samples enabled one to analyze local disorder effects known to be apparent in Heusler alloys by the mean of x-ray diffraction. This technique revealed two disorder types in Co_2MnSi thin films. The Mn-Si disorder is assumed to be responsible for the drastic change of saturation magnetization during annealing, where the Co-Mn disorder affects the saturation magnetization lattice constant

in a slight way.

Having studied the single Co_2MnSi films very intensively, the integration of Co_2MnSi in magnetic tunnel junctions is in turn. For this purpose a procedure has been established that follows the efforts of both, the single layer preparation and the MTJ integration. The important features of this procedure are the two separated annealing processes to enhance the local ordering in Co_2MnSi and to activate the exchange bias anisotropy in the $\text{Co}_{70}\text{Fe}_{30}/\text{Mn}_{83}\text{Ir}_{17}$ electrode. The Co_2MnSi annealing has to be inserted only after the prepared AlO_x barrier. At all other stages no TMR amplitude is measurable due to the presence of impurities at the elevated interfaces to destroy the highly spin polarized surface or the exchange bias.

Applying this procedure successfully, one has been enabled to determine the spin polarization of Co_2MnSi thin films. Measuring at 10 K and at low bias voltage of 1 mV, a spin polarization of 66 % has been achieved, which is quite higher than all other measurements for Heusler alloys reported in literature.

However, at room temperature and at higher bias voltages, the spin polarization drastically drops in contrast to reference MTJs consisting of 3d transition metal electrodes. This makes the application at room temperature unattractive. To reveal the origin for this behavior, the Co_2MnSi containing MTJs have been intensively studied by indirect and direct techniques. The electrical characterization has revealed an additional 0.6 nm barrier with a step-like shape, which has been confirmed by AES and XAS. These two direct techniques have detected a 0.5 nm MnSi_xO_y segregation layer at the $\text{Co}_2\text{MnSi}/\text{AlO}_x$ interface in agreement with the electrical characterization. By IETS scattering on magnetic Mn ions has been assumed to take place at the $\text{Co}_2\text{MnSi}/\text{AlO}_x$ interface. For the strong temperature dependence of TMR effect amplitude, large ratios of unpolarized tunnel current have been identified to be responsible, which can maybe attributed to magnon or defect scattering at the MnSi_xO_y segregation layer.

In order to prevent the formation of the MnSi_xO_y segregation layer, Co intercalation films of variable thickness have been inserted at the $\text{Co}_2\text{MnSi}/\text{AlO}_x$ interface. And indeed, no segregation could be found by AES or XAS for thick enough Co layers. Correspondingly, the bias voltage as well as the temperature dependence degrades to a degree of reference MTJs. However, these investigations have revealed only a low spin polarization. The TMR effect amplitude drastically drops due to Co antisite disorder and regains a Co-like value for 3-6 nm Co layers at annealing up to 500 °C.

All this together makes it possible to conclude for further investigations that much efforts have to be put in the AlO_x oxidation process. The variation of the oxidation parameters as aluminum layer thickness, microwave power, kinetic energy of the ions or oxidation time give a lot of possibilities as well as alternative oxidation techniques such as pulse plasma, native or thermal oxidation have to be taken into account. First experiments with pulse plasma oxidation reveal again the formation of the MnSi_xO_y segregation layer.

Despite the presence of this segregation layer, information about the influence of local disorder within Co_2MnSi could be studied. As in the single layer investigations, the high ordered state with high spin polarization corresponds to minimum lattice constants and maximum saturation magnetization. A reduction of spin polarization could be also attributed to Co-Mn antisite disorder.

This microstructure effect on atomic scale is added by an effect of the Co_2MnSi layer thickness. Although the magnetism stays nearly unchanged down to 6 nm, the spin polarization already drops at 30 nm. This thickness induced decrease of spin polarization has been attributed to the accompanied decrease of the grain size from 100-200 nm at 100 nm down to 50-100 nm at 15 nm. This makes clear that the spin polarization is more sensitive to microstructural defects, although the bulk and surface magnetism stays unchanged.

In conclusion, 100 years after the discovery of the Heusler alloys by Friedrich Heusler, their possibility to applications in spintronic devices has been demonstrated and, thus, may reopen new importance to the Heusler alloys in field of spintronics.

Appendix A

X-ray diffraction patterns

The intensity of the diffracted beam of an x-ray diffraction experiment is composed of several contributions, as denoted in paragraph 1.2.2. One crucial part is the structure factor, which is very sensitive to local disorder processes. Assuming the absence of local disorder and a perfect polycrystalline sample, the peak intensities can be calculated or determined experimentally on powder samples. For various compositions, this data is collected in [11]. Hence, for comparison the peak intensities are denoted with respect to the same experimental assembly including the wavelength of a copper x-ray tube ($\lambda_{av}=1.54184 \text{ \AA}$) and together with Miller indices (hkl) and distance of the diffracting planes for clarity. The underlying unit cell is accounted by the structure type (Hermann-Mauguin (order number)) and by the corresponding lattice constant.

| Vanadium | | | |
|----------------------------------|----------------------|--------------------|-----------|
| Im3m(229); $a=3.027 \text{ \AA}$ | | | |
| hkl | $d_{hkl} [\text{Å}]$ | $2\theta [^\circ]$ | intensity |
| 110 | 2.1411 | 42.208 | 100 |
| 200 | 1.5141 | 61.216 | 17 |
| 211 | 1.2363 | 77.155 | 33 |
| 220 | 1.0704 | 92.145 | 10 |
| 310 | 0.9575 | 107.24 | 18 |
| 222 | 0.8739 | 123.80 | 7 |
| 321 | 0.8091 | 144.65 | 29 |

Table A.1: X-ray diffraction pattern of vanadium after [11]

| Silicon | | | |
|-----------------------------------|------------------------|--------------------|-----------|
| Fd3m(227); $a=5.4306 \text{ \AA}$ | | | |
| hkl | $d_{hkl} [\text{\AA}]$ | $2\theta [^\circ]$ | intensity |
| 111 | 3.1355 | 28.466 | 100 |
| 220 | 1.9201 | 47.344 | 90 |
| 311 | 1.6735 | 56.171 | 57 |
| 400 | 1.3577 | 69.196 | 14 |
| 331 | 1.2459 | 76.452 | 28 |
| 422 | 1.1086 | 88.118 | 34 |
| 511 | 1.0452 | 95.052 | 18 |
| 440 | 0.9601 | 106.84 | 10 |
| 531 | 0.9180 | 114.23 | 24 |
| 620 | 0.8587 | 127.73 | 29 |
| 533 | 0.8282 | 137.13 | 11 |

Table A.2: X-ray diffraction pattern of silicon after [11]

| Co₂MnSi | | | |
|----------------------------------|------------------------|--------------------|-----------|
| Fm3m(225); $a=5.670 \text{ \AA}$ | | | |
| hkl | $d_{hkl} [\text{\AA}]$ | $2\theta [^\circ]$ | intensity |
| 111 | 3.2740 | 27.238 | 3 |
| 200 | 2.8340 | 31.570 | 4 |
| 220 | 2.0040 | 45.249 | 100 |
| 311 | 1.7100 | 53.594 | 1 |
| 222 | 1.6360 | 56.227 | 1 |
| 400 | 1.4170 | 65.920 | 14 |
| 420 | 1.2680 | 74.887 | 2 |
| 422 | 1.1570 | 83.566 | 35 |
| 440 | 1.0020 | 100.59 | 10 |
| 620 | 0.8965 | 118.61 | 22 |
| 444 | 0.8184 | 140.77 | 2 |

Table A.3: X-ray diffraction pattern of Co₂MnSi after [11]

Publications and talks

Publications

- D. Sudfeld, K. Wojczykowski, W. Hachmann, S. Heitmann, K. Rott, T. Hempel, S. Kaemmerer, P. Jutzi, A. Huetten, and G. Reiss, *Magnetic cobalt nanocrystals organized in patches and chains*, IEEE Trans. Mag., **38**, 2601 (2002)
- S. Kämmerer, S. Heitmann, D. Meyners, D. Sudfeld, A. Thomas, A. Hütten, and G. Reiss, *Room-temperature preparation and magnetic behavior of Co_2MnSi thin films*, J. Appl. Phys. **93**, 7945 (2003)
- M. Rabe, U. May, H. Siegle, A. Hütten, S. Kämmerer, M. Justus, and G. Reiss, *Magnetotransport properties of hard magnetic pinned multilayers*, J. Appl. Phys. **95**, 1211 (2004)
- G. Reiss, H. Brückl, A. Hütten, H. Koop, D. Meyners, A. Thomas, S. Kämmerer, J. Schmalhorst, and M. Brzeska, *New materials and applications for magnetic tunnel junctions*, Phys. Stat. Sol. **201**, 1628 (2004)
- S. Kämmerer, A. Thomas, A. Hütten, and G. Reiss, *Co_2MnSi Heusler alloy as magnetic electrodes in magnetic tunnel junctions*, Appl. Phys. Lett. **85**, 79 (2004)
- J. Schmalhorst, S. Kämmerer, M. Sacher, G. Reiss, A. Hütten, and A. Scholl, *Interface structure and magnetism of magnetic tunnel junctions with Co_2MnSi electrode*, Phys. Rev. B **70**, 024426 (2004)
- J. Schmalhorst, S. Kämmerer, G. Reiss, and A. Hütten, *Inelastic electron tunneling spectroscopy and bias voltage dependence of magnetic tunnel junctions with polycrystalline Co_2MnSi electrode*, submitted to APL
- A. Hütten, S. Kämmerer, J. Schmalhorst, A. Thomas, and G. Reiss, *The current potential of Co_2MnSi Heusler alloy electrodes in magnetic tunnel junctions*, accepted for Phys. Stat. Solidi
- A. Hütten, S. Kämmerer, J. Schmalhorst, and G. Reiss, *Heusler alloyed electrodes integrated in magnetic tunnel junctions*, chapter 9 in "Halfmetallic Alloys: Funda-

mentals and Applications” (Springer series ”Lecture Notes on Physics”), editors: I. Galanakis und H. Dederichs, Springer Verlag (2004), in press

Talks and posters

- Talk: 2001 DPG-Frühjahrstagung Hamburg, *Schaltverhalten von antiferromagnetisch und ferromagnetisch gekoppelten Dreischichtsystemen*
- Talk: 2002 MMM 2002 Tampa, *Room temperature preparation and magnetic behavior of Co_2MnSi thin films*
- Talk: 2003 DPG-Frühjahrstagung Dresden, *Evolution of microstructural, magnetic, and electrical properties of the Co_2MnSi Heusler alloy*
- Poster: 2003 ICMFS Madrid, *First spin polarization measurements of the Heusler alloy Co_2MnSi in magnetic tunnel junctions*
- Talk: 2003 ICMFS Madrid, *Magnetic Interactions in Multilayers for Magnetoelectronic Applications*
- Poster: 2004 DPG-Frühjahrstagung Regensburg, *Spinpolarisation in dünnen Co_2MnSi Filmen*

Bibliography

- [1] F. Heusler, Verh. Dtsch. Phys. Ges. **5**, 219 (1903).
- [2] R. de Groot, F. Mueller, P. van Engen, and K. Buschow, Phys. Rev. Lett. **50**, 2024 (1983).
- [3] S. Ishida, T. Masaki, S. Fujii, and S. Asano, Physica B **245**, 1 (1998).
- [4] P. Webster, J. Phys. Chem. Solids **32**, 1221 (1971).
- [5] U. Geiersbach, A. Bergmann, and K. Westerholt, J. Magn. Magn. Mat. **240**, 546 (2002).
- [6] U. Geiersbach, A. Bergmann, and K. Westerholt, Thin Sol. Films **425**, 225 (2003).
- [7] M. Raphael, B. Ravel, M. Willard, S. Cheng, B. Das, R. Stroud, K. Bussmann, J. Claassen, and V. Harris, Appl. Phys. Lett. **79**, 4396 (2001).
- [8] M. Julliere, Phys. Lett. **54A**, 225 (1975).
- [9] P. Brown, K. Neumann, P. Webster, and K. Ziebeck, J. Phys.: Condens. Matter **12**, 1827 (2000).
- [10] J. Moodera and G. Mathon, J. Magn. Magn. Mat. **200**, 248 (1999).
- [11] Reference database, International Centre for Diffraction Data, 1999.
- [12] B. Ravel, M. Raphael, and V. Harris, Phys. Rev. B **65**, 184431 (2002).
- [13] D. Orgassa, H. Fujiwara, T. Schulthess, and W. Butler, Phys. Rev. B **60**, 13237 (1999).
- [14] I. Galanakis, P. Dederichs, and N. Papanikolaou, Phys. Rev. B **66**, 174429 (2002).
- [15] F. Cardarelli, *Materials Handbook* (Springer-Verlag, London, 2000).
- [16] J. Schmalhorst, *Magnetismus: Grundlagen und Anwendungen (part 1)*, 2004, Course in Semester 2003/2004 at the University of Bielefeld.

- [17] G. Güntherodt and U. Rüdiger, *30. Ferienkurs des Instituts für Festkörperforschung 1999: Magnetische Schichtsysteme* (Forschungszentrum Jülich, Jülich, 1999), chap. A9: Magnetische Festkörper: ein Überblick, p. A9.1.
- [18] P. Webster, *Contemp. Phys.* **10**, 559 (1969).
- [19] S. Parkin, N. More, and K. R. and M. G., *Phys. Rev. Lett.* **64**, 2304 (1990).
- [20] P. Grünberg, R. Schreiber, Y. Pang, M. Brodsky, and H. Sowers, *Phys. Rev. Lett.* **57**, 2442 (1986).
- [21] C. Kittel, *Einführung in die Festkörperphysik* (R. Oldenbourg Verlag, Munich, 1999).
- [22] C. Zener and R. Heikes, *Rev. Mod. Phys.* **25**, 191 (1953).
- [23] A. Morrish, *The physical principles of magnetism* (IEEE Press, New York, 2001).
- [24] W. Nolting, *Quantentheorie des Magnetismus* (Teubner, Stuttgart, 1986).
- [25] J. Kübler, A. Williams, and C. Sommers, *Phys. Rev. B* **28**, 1745 (1983).
- [26] V. Yu Irkhin and M. Katsnel'son, *Phys. Usp.* **37**, 659 (1994).
- [27] P. Webster, *J. Appl. Phys.* **52**, 2040 (1981).
- [28] C. Zener, *Phys. Rev.* **81**, 440 (1953).
- [29] S. Picozzi, A. Continenza, and A. Freeman, *Phys. Rev. B* **66**, 094421 (2002).
- [30] J. Caballero, Y. Park, A. C. J. Childress, F. Petroff, and R. Morel, *J. Appl. Phys.* **81**, 2740 (1996).
- [31] J. Caballero, W. Geerts, J. Childress, F. Petroff, P. Galtier, J. Thiele, and D. Weller, *Appl. Phys. Lett.* **71**, 2382 (1997).
- [32] J. Caballero, Y. Park, and A. C. J. Childress, *J. Elec. Mat.* **26**, 1274 (1997).
- [33] J. Caballero, W. Geerts, F. Petroff, J. Thiele, and D. W. and J.R. Childress, *J. Magn. Magn. Mat.* **177-181**, 1229 (1998).
- [34] J. Caballero, Y. Park, J. Childress, J. Bass, W. Chiang, A. Reilly, W. Pratt, and F. Petroff, *J. Vac. Sci. Technol. A* **16**, 1801 (1998).
- [35] J. Caballero, A. Reilly, Y. Hao, J. Bass, W. Pratt, F. Petroff, and J. Childress, *J. Magn. Magn. Mat.* **198-199**, 55 (1999).
- [36] C. Tanaka, J. Nowak, and J. Moodera, *J. Appl. Phys.* **86**, 6239 (1999).
- [37] C. Fang and G. de Wijs and R.A. de Groot, *J. Appl. Phys.* **91**, 8340 (2002).

- [38] I. Galanakis, J. Phys.: Condens. Mat. **14**, 6329 (2002).
- [39] J. Coey and C. Chien, MRS Bulletin **October**, 720 (2003).
- [40] C. Palmstrom, MRS Bulletin **October**, 725 (2003).
- [41] S. Picozzi, A. Continenza, and A. Freeman, Phys. Rev. B **69**, 094423 (2004).
- [42] S. Ishida, S. Fujii, H. Nagayoshi, and S. Asano, Physica B **254**, 157 (1998).
- [43] S. Parker, *Solid-state physics source book* (McGraw-Hill Book Company, New York, 1988).
- [44] D. de Fontane, Solid State Phys. **34**, 73 (1979).
- [45] S. Heitmann, *Cobalt/copper multilayers: Interplay of microstructure and GMR amplitude and recrystallization as the key towards temperature stability*, PhD thesis, University of Bielefeld, Department of Physics, 2004.
- [46] B. Cullity and S. Stock, *Elements of X-ray diffraction* (Prentice Hall, London, 2001).
- [47] B. Warren, *X-ray diffraction* (Dover Publications, New York, 1990).
- [48] C. Weißmantel and C. Hamann, *Grundlagen der Festkörperphysik* (Johann Ambrosius Barth Verlag, Heidelberg, 1995).
- [49] J. Vossen and W. Kern, editors, *Thin film processes* (Academic Press, New York, 1978).
- [50] A. Elshabini-Riad and F. Barlow III, *Thin film technology handbook* (McGraw-Hill, New York, 1997).
- [51] W. Schweika, *30. Ferienkurs des Instituts für Festkörperforschung 1999: Magnetische Schichtsysteme* (Forschungszentrum Jülich, Jülich, 1999), chap. A5: Schichtpräparation mit Sputterverfahren, p. A5.1.
- [52] H. Hauser, R. Chabicovsky, and K. Riedling, Thin magnetic films, in *Nanomaterials and magnetic thin films*, edited by H. Nalwa, , Handbook of thin film materials Vol. 5, chap. 8, p. 375, Academic Press, San Diego, 2002.
- [53] Y. Kuz'ma and E. Gladyshevskii, Russ. J. Inorganic Chem. **9**, 373 (1964).
- [54] F. Leutloff, Diplomarbeit, University of Bielefeld, Department of Physics, 2004.
- [55] PureTech Inc., 2003, personal notification by B. Mayer.
- [56] H. Grohman, Development of sputtering target microstructure by inert gas hot pressing, website of PureTech Inc. - www.puretechinc.com/tech_papers/tech_papers.htm.

- [57] Heraeus Noblelight, *Kurzwellige Infrarot-Strahler*, 2001.
- [58] A. Thomas, *Preparation and characterisation of magnetic single and double barrier junctions*, PhD thesis, University of Bielefeld, Department of Physics, 2004.
- [59] S. Kämmerer, A. Thomas, H. Brückl, G. Reiss, and A. Hütten, *First spin polarization measurements of the Heusler alloy Co_2MnSi in magnetic tunnel junctions*, 2003, Poster - ICMFS Madrid 2003.
- [60] S. Kämmerer, S. Heitmann, D. Meyners, D. Sudfeld, A. Thomas, A. Hütten, and G. Reiss, *J. Appl. Phys.* **93**, 7945 (2003).
- [61] P. Bechthold, *30. Ferienkurs des Instituts für Festkörperforschung 1999: Magnetische Schichtsysteme* (Forschungszentrum Jülich, Jülich, 1999), chap. C8: Magnetooptische Effekte: Phänomenologische Beschreibung und Anwendungen, p. C8.1.
- [62] J. Schmalhorst, *Magnetismus: Grundlagen und Anwendungen (part 2)*, 2003, Course in Semester 2002/2003 at the University of Bielefeld.
- [63] S. Cheng, B. Nadgorny, E. Carpenter, B. Das, G. Trotter, M. Raphael, and V. Harris, *IEEE Trans. Mag.* **37**, 2176 (2001).
- [64] W. Brinkman, R. Dynes, and J. Rowell, *J. Appl. Phys.* **41**, 1915 (1970).
- [65] J. Schmalhorst, *Magnetische, thermische und dielektrische Stabilität von magnetischen Tunnelelementen*, PhD thesis, University of Bielefeld, Department of Physics, 2001.
- [66] E. Wolf, *Principles of electron tunneling spectroscopy* (Oxford University Press, New York, 1989).
- [67] J. Schelten, *30. Ferienkurs des Instituts für Festkörperforschung 1999: Magnetische Schichtsysteme* (Forschungszentrum Jülich, Jülich, 1999), chap. D7: Tunnelmagnetowiderstand, p. D7.1.
- [68] N. Pinto, R. Murri, and M. Nowak, Magnetotransport effects in semiconductors, in *Nanomaterials and magnetic thin films*, edited by H. Nalwa, , Handbook of thin film materials Vol. 5, chap. 9, p. 439, Academic Press, San Diego, 2002.
- [69] H. Brückl, J. Schmalhorst, G. Reiss, G. Gieres, and J. Wecker, *Appl. Phys. Lett.* **78**, 1113 (2001).
- [70] C. Shang, J. Nowak, R. Jansen, and J. Moodera, *Phys. Rev. B* **58**, R2917 (1998).
- [71] R. Jansen and J. Moodera, *Phys. Rev. B* **61**, 9047 (2000).
- [72] A. MacDonald, T. Jungwirth, and M. Kasner, *Phys. Rev. Lett.* **81**, 705 (1998).

- [73] J. Moodera, J. Nowak, and R. Veerdonk, *Phys. Rev. Lett.* **80**, 2941 (1998).
- [74] S. Eisebitt, *30. Ferienkurs des Instituts für Festkörperforschung 1999: Magnetische Schichtsysteme* (Forschungszentrum Jülich, Jülich, 1999), chap. C6: Zirkulardichroismus and der Rumpfaborption, p. C6.1.
- [75] P. LeClair, *Fundamental aspects of spin polarized tunneling*, PhD thesis, Eindhoven University of Technology, 2002.
- [76] P. Tedrow and R. Meservey, *J. Appl. Phys.* **16**, 71 (1975).
- [77] J. de Teresa, A. Barthelemy, A. Fert, J. Contour, F. Montaigne, and P. Seneor, *Science* **286**, 507 (1999).
- [78] P. Scherrer, *Goettinger Nachr.* **2**, 98 (1918).
- [79] H. Klug, *X-ray diffraction procedures* (John Wiley and Sons, New York, 1974).
- [80] H. Bunge, *Quantitative texture analysis* (Deutsche Gesellschaft für Metallkunde, Oberursel, 1986).
- [81] H. Bunge, *Experimental techniques of texture analysis* (Deutsche Gesellschaft für Metallkunde, Oberursel, 1986).
- [82] H. Bunge, *Advances and applications of quantitative texture analysis* (Deutsche Gesellschaft für Metallkunde, Oberursel, 1986).
- [83] J. Schmalhorst, S. Kämmerer, M. Sacher, G. Reiss, A. Hütten, and A. Scholl, *Phys. Rev. B* **70**, 024426 (2004).
- [84] R. Meservey and P. Tedrow, *Phys. Rep.* **238**, 173 (1994).
- [85] C. Carbone, *30. Ferienkurs des Instituts für Festkörperforschung 1999: Magnetische Schichtsysteme* (Forschungszentrum Jülich, Jülich, 1999), chap. B2: Photoemission from Magnetic Films, p. B2.1.
- [86] L. Baumgarten, *30. Ferienkurs des Instituts für Festkörperforschung 1999: Magnetische Schichtsysteme* (Forschungszentrum Jülich, Jülich, 1999), chap. A8: Winkelauflöste Photoemission zur Bandstrukturbestimmung in Festkörpern, p. A8.1.
- [87] J. Coey, J. Versluijs, and M. Venkatesan, *J. Phys. D: Appl. Phys.* **35**, 2457 (2002).
- [88] D. Ristoiu, J. Nozieres, C. Borca, T. Komesu, H. Jeong, and P. Dowben, *Europhys. Lett.* **49**, 624 (2000).
- [89] S. Kevan, editor, *Angle resolved photoemission : theory and current applications* (Elsevier, Amsterdam, 1992).

- [90] N. Garcia, M. Munoz, and Y. Zhao, *Phys. Rev. Lett.* **82**, 2923 (1999).
- [91] R. Soulen Jr. *et al.*, *Science* **282**, 85 (1998).
- [92] S. Upadhyay, A. Palanisami, R. Louie, and R. Buhrman, *Phys. Rev. Lett.* **81**, 3247 (1998).
- [93] P. Rossiter, *The electrical resistivity of metals and alloys* (Cambridge University Press, Cambridge, 1987).
- [94] S. Kämmerer, A. Thomas, A. Hütten, and G. Reiss, *Appl. Phys. Lett.* **85**, 79 (2004).
- [95] Y. Pauleau, Residual stress in physically vapor-deposited thin films, in *Deposition and processing of thin films*, edited by H. Nalwa, , Handbook of thin film materials Vol. 1, chap. 9, p. 455, Academic Press, San Diego, 2002.
- [96] W. Meiklejohn, *Rev. Mod. Phys.* **25**, 302 (1953).
- [97] B. Cullity, *Introduction to magnetic materials* (Addison-Wesley Publishing Company, London, 1972).
- [98] I. Rohde, Diplomarbeit, University of Bielefeld, Department of Physics, 2003.
- [99] A. Hütten, *Magnetic Interactions in Multilayers for Magnetoelectronic Applications*, 2003, Talk - ICMFS Madrid 2003.
- [100] M. Rabe, U. May, H. Siegle, A. Hütten, S. Kämmerer, M. Justus, and G. Reiss, *J. Appl. Phys.* **95**, 1211 (2004).
- [101] M. Rabe, *Magnetismus von hartmagnetischen Biasschichten für Anwendungen in magnetoresistiven Elementen*, PhD thesis, Robert Bosch GmbH, 2003.
- [102] J. Nogues and I. Schuller, *J. Magn. Magn. Mat.* **192**, 203 (1999).
- [103] A. Berkowitz and K. Takano, *J. Magn. Magn. Mat.* **200**, 552 (1999).
- [104] D. Dahlberg, *A microscopic understanding of exchange anisotropy in Fe/MnF₂ bilayers*, 2003, Conference talk - ICMFS Madrid 2003.
- [105] A. Devasahayam and M. Kryder, *IEEE Trans. Mag.* **35**, 649 (1999).
- [106] Y. Saito, M. Amano, K. Nakajima, S. Takahashi, and M. Sagoi, *J. Magn. Magn. Mat.* **223**, 293 (2001).
- [107] K. Yagami, M. Tsunoda, and M. Takahashi, *J. Appl. Phys.* **89**, 6609 (2001).
- [108] K. Takahashi, A. Sawa, Y. Ishii, H. Akoh, M. Kawasaki, and Y. Tokura, *Phys. Rev. B* **67**, 094413 (2002).

- [109] Goodfellow GmbH Bad Nauheim, website - www.goodfellow.com, physical properties of various materials.
- [110] J. Dean, editor, *Lane's handbook of chemistry* (McGraw-Hill Book Company, New York, 1973).
- [111] Z. Zhang, P. Freitas, A. Ramos, N. Barradas, and J. Soares, *Appl. Phys. Lett.* **91**, 8786 (2002).
- [112] S. Parkin *et al.*, *J. Appl. Phys.* **85**, 5828 (1999).
- [113] X. Han, M. Oogane, H. Kubota, Y. Ando, and T. Miyazaki, *Appl. Phys. Lett.* **77**, 283 (2000).
- [114] R. Sousa, J. Sun, V. Soares, P. Freitas, A. Kling, M. da Silva, and J. Soares, *Appl. Phys. Lett.* **73**, 3288 (1998).
- [115] S. Tehrani, J. Slaughter, E. Chen, M. Darlam, J. Shi, and M. de Herrera, *IEEE Trans. Magn.* **35**, 2814 (1999).
- [116] M. Henzler and W. Göpel, *Oberflächenphysik des Festkörpers* (Teubner Studienbücher, Stuttgart, 1994).
- [117] S. Nonoyama, H. Itoh, A. Oguri, J. Inoue, and P. Bruno, *J. Magn. Magn. Mat.* **198-199**, 158 (1999).
- [118] N. Tezuka, M. Oogane, and T. Miyazaki, *J. Magn. Magn. Mat.* **198-199**, 149 (1999).
- [119] R. Jansen and J. Moodera, *Appl. Phys. Lett.* **75**, 400 (1999).
- [120] A. Saffarzadeh, *J. Magn. Magn. Mat.* **269**, 327 (2004).
- [121] A. Vedyayev, D. Bagrets, A. Bagrets, and B. Dieny, *Phys. Rev. B* **63**, 064429 (2001).
- [122] E. Tsymbal and D. Pettifor, *J. Magn. Magn. Mat.* **198-199**, 146 (1999).
- [123] A. Vedyayev, D. Bagrets, A. Bagrets, N. Ryzhanova, N. Strelkov, B. Dieny, and C. Lacroix, *J. Magn. Magn. Mat.* **242-245**, 453 (2002).
- [124] C. de Groot, Y. Ouyang, S. Ko, E. Kendall, Q. Shu, and J. Moodera, *J. Phys.: Condens. Mat.* **14**, 5153 (2002).
- [125] J. Simmons, *J. Appl. Phys.* **34**, 1793 (1963).
- [126] A. Bratkovky, *Phys. Rev. B* **56**, 2344 (1997).
- [127] L. Ritchie, G. Xiao, Y. Ji, T. Chen, C. Chien, M. Zhang, J. Chen, Z. Liu, G. Wu, and X. Zhang, *Phys. Rev. B* **68**, 104430 (2003).

- [128] J. Mathon and S. Ahmad, *Phys. Rev. B* **37**, 660 (1988).
- [129] T. Regan, H. Ohldag, C. Stamm, F. Nolting, J. Lüning, J. Stöhr, and R. White, *Phys. Rev. B* **64**, 214422 (2001).
- [130] Y. Yonamoto, T. Yokoyama, K. Amemiya, D. Matsumura, and T. Ohta, *Phys. Rev. B* **63**, 214406 (2001).
- [131] J. Murai, Y. Ando, and T. Miyazaki, *Nippon Oyo Jiki Gakkaishi* **23**, 64 (1999).
- [132] J. Murai, Y. Ando, T. Daibou, K. Yaoita, H. Han, and T. Miyazaki, *J. Magn. Magn. Mat.* **226-230**, 922 (2001).
- [133] Y. Ando, J. Murai, and T. Miyazaki, *J. Magn. Magn. Mat.* **198-199**, 161 (1999).
- [134] Y. Ando, J. Murai, H. Kubota, and T. Miyazaki, *J. Appl. Phys.* **87**, 5209 (2000).
- [135] R. Veerdonk, J. Moodera, and W. de Jonge, *J. Magn. Magn. Mat.* **198-199**, 152 (1999).
- [136] W. Nolting, *Statistische Physik* (Vieweg, Braunschweig, 1998).
- [137] X. Han, A. Yu, M. Oogane, J. Murai, T. Daibou, and T. Miyazaki, *Phys. Rev. B* **63**, 224404 (2001).
- [138] T. Wolfram, editor, *Inelastic electron tunneling spectroscopy* (Springer-Verlag, Berlin, 1978).

Acknowledgment - Danksagung

Zunächst einmal geht mein besondere Dank an ALLE, die mir bei der Erstellung dieser Arbeit zur Seite gestanden und geholfen haben.

Insbesondere möchte ich mich für die gute Betreuung und finanzielle Unterstützung bei Priv. Doz. Dr. Andreas Hütten, Prof. Dr. Günter Reiss, Priv. Doz. Dr. Hubert Brückl, Dr. Jan Schmalhorst und Dr. Willi Schepper bedanken.

Andreas danke ich für die immer motivierende Betreuung und die reichlichen Ideen, die wesentlich zum Erfolg dieser Arbeit beigetragen haben. Zudem war es immer wieder nett, über die Tücken des Fußballs zu plaudern.

Sonja Heitmann danke ich für die sehr gründliche und hervorragende Einarbeitung in die Kunst der Röntgenbeugung und -reflektometrie. Dabei möchte ich natürlich nicht die angenehme Atmosphäre in unserem Büro vergessen, zu der auch Maik Justus maßgeblich beigetragen hat.

Maik möchte ich sodann auch für die vielen kleinen Tips und Hilfestellungen bei fast allen experimentellen Anlagen bedanken.

Andy Thomas danke ich für die ausführliche Einarbeitung in den TMR-*stuff* und für das kritische Korrekturlesen der ersten Version dieser Arbeit.

Beim Dank für die TMR-Details darf und möchte ich natürlich nicht Hubert Brückl und Jan Schmalhorst vergessen, die mir für kleine Fragen immer spontan zur Verfügung standen. Jan gilt es zusätzlich noch für die stöchiometrische und magnetische Charakterisierung der Grenzflächen und die IETS-Messungen zu danken.

Dank auch für die Möglichkeit die XAS- und XMCD-Messungen an der Beamline 7.3.1.1 an der Advanced Light Source in Berkeley (USA) durchführen zu lassen.

Bei Marc Sacher möchte ich mich für die vorzügliche Bereitstellung der großen Sputteranlage bedanken, sowie für vereinzelte AFM-Messungen, wobei der Großteil der Rauigkeitsbestimmungen von Dirk Meyners durchgeführt wurden, für die ich mich hiermit bedanken möchte.

Karsten Rott danke ich für zahlreiche kleine Tips zu diversen Anlagen und Strukturierungsproblemen.

Dank geht an Daniela Sudfeld und Inga Ennen für diverse AGM-Messungen.

Jan Bornemeier danke ich für das zuverlässige Bonden meiner magnetischen Tunnelemente.

Dank an Frimin Leutloff für den Ersatz von Maik als Zimmerkollege und die vielen kleinen unterstützenden Hilfen bei diversen Messungen und Probenherstellungen.

Mark und Steffi danke ich für die spontane Unterstützung bei der Korrektur der englischen Sprache.

Für die "weiche" Unterstützung möchte ich mich bei meinen Eltern, Freunden und natürlich bei meiner Freundin Mirja herzlich bedanken.